AD-A253 923

②

PENNSTATE

Inhibiting Corrosion in Gr/Al and Gr/Mg Metal Matrix Composites Using Nonequilibrium Alloying Techniques

DTIC
ELECTE
AUG 11 1992
S A D

Annual Report
April 1, 1991 - March 31, 1992

Submitted to:
Office of Naval Research
800 North Quincy Street
Arlington, VA 22217-5000

Original contains color plates: All DTIC reproductions will be in black and white

Submitted by:

B.A. Shaw and T.R. Schrecengost
Penn State University, University Park, PA 16802

W.C. Moshler and R.G. Wendt
Martin Marletta Space Systems, Denver CO 80201

June 1992

92 8 7 150

92-22544

REPORT DOCUMENTATION PAGE

Public reporting burden for this collection of information is estimated to average 1 hour per response, including the time for reviewing instructions, searching existing data sources, gathering and maintaining the data needed, and completing and reviewing the collection of information. Send comments regarding this burden estimate or any other aspect of this collection of information, including suggestions for reducing this burden, to Washington Headquarters Services, Directorate for Information Operations and Reports, 1215 Jefferson Davis Highway, Suite 1204, Arlington, VA 22202-4302, and to the Office of Management and Budget, Paperwork Reduction Project (0704-0188), Washington, DC 20503.

1. AGENCY USE ONLY (Leave blank)	2. REPORT DATE	3. REPORT TYPE AND DATES COVERED
	June 1992	Annual 4/1/91 - 3/31/92

4. TITLE AND SUBTITLE	5. FUNDING NUMBERS
Inhibiting Corrosion in Gr/Al and Gr/Mg Metal Matrix Composites Using Nonequilibrium Alloying	N00014-91-J-1196

6. AUTHOR(S)

B.A. Shaw, T.R. Schrecengost, W.C. Moshier, and

R.G. Wendt

7. PERFORMING ORGANIZATION NAME(S) AND ADDRESS(ES)	8. PERFORMING ORGANIZATION REPORT NUMBER
The Pennsylvania State University Department of Engineering Science and Mechanics 227, Hammond Bldg; University park, PA 16802	

9. SPONSORING/MONITORING AGENCY NAME(S) AND ADDRESS(ES)	10. SPONSORING/MONITORING AGENCY REPORT NUMBER

11. SUPPLEMENTARY NOTES

12a. DISTRIBUTION/AVAILABILITY STATEMENT	12b. DISTRIBUTION CODE
Distribution --Unlimited	

13. ABSTRACT (Maximum 200 words)

Metal matrix composites (MMCs) have been heavily studied over the past thirty years. During that period, many proposals have been made to develop a matrix alloy that was compatible with the reinforcing phase. However, for one reason or another, the technology has continued to focus on conventional alloys and fabrication practices. Although tremendous advances have been made on composite materials, the basic technology remains similar to systems studied twenty years ago. This work represents the first program where new alloys are being developed for graphite reinforced composites which are tailored to a novel processing technology for manufacturing corrosion resistant graphite reinforced composites.

14. SUBJECT TERMS		15. NUMBER OF PAGES
		100
		16. PRICE CODE

17. SECURITY CLASSIFICATION OF REPORT	18. SECURITY CLASSIFICATION OF THIS PAGE	19. SECURITY CLASSIFICATION OF ABSTRACT	20. LIMITATION OF ABSTRACT
Unclassified	Unclassified	Unclassified	

NSN 7540-01-280-5500

Inhibiting Corrosion in Gr/Al and Gr/Mg Metal Matrix Composites Using Nonequilibrium Alloying Techniques

DTIC QUALITY INSPECTED 5

Annual Report
April 1, 1991 - March 31, 1992

Accesion For		
NTIS CRA&I		✓
DTIC TAB		[
U: announced		[ ]
Justification		
By		
Distribution /		
Availability Codes		
Dist	Avail and / or Special	
A-1		

Submitted by:

B.A. Shaw and T.R. Schrecengost
Penn State University, University Park, PA 16802

W.C. Moshier and R.G. Wendt
Martin Marietta Space Systems, Denver CO 80201

June 1992

EXECUTIVE SUMMARY

Metal matrix composites (MMCs) have been heavily studied over the past thirty years. During that period, many proposals have been made to develop a matrix alloy that was compatible with the reinforcing phase. However, for one reason or another, the technology has continued to focus on conventional alloys and fabrication practices. Although tremendous advances have been made on composite materials, the basic technology remains similar to systems studied twenty years ago. This work represents the first program where new alloys are being developed for graphite reinforced composites which are tailored to a novel processing technology for manufacturing corrosion resistant graphite reinforced composites.

High modulus graphite fiber reinforced metal matrix composites offer a wide variety of attractive properties including: high specific modulus and strength (E/ρ and UTS/ρ), tailorable or zero coefficient of thermal expansion (CTE), and high thermal conductivity. With these properties, structures can be designed and fabricated from MMCs that are dimensionally stable when subjected to both thermal and mechanical perturbations.

However, several problems have been associated with graphite/magnesium (Gr/Mg) and graphite/aluminum (Gr/Al) MMCs that can be grouped into four major categories:

- poor corrosion resistance,
- significant reactivity between the fiber and matrix during processing that can lead to embrittlement,
- excessive thermal and strain hysteresis due to low matrix strength, and
- limited processing capabilities restricted to simple shapes and fiber architectures.

In this program, nonequilibrium alloying by sputter vapor deposition is being investigated and offers the potential to eliminate all of these shortcomings. Although the emphasis of this investigation is on improving the corrosion resistance, this technique may also greatly enhance fabrication capability, eliminate fiber/matrix reaction, and reduce thermal hysteresis.

During this first year, binary alloys consisting of Mg-Cr, Mg-Mo, Mg-Ta, Mg-W, Al-Cr, Al-Mo, Al-Ta, and Al-W as well as ternary alloys composed Mg-Ta-W, Mg-Al-W, and Al-Mg-W were successfully fabricated. While all exhibited improved corrosion resistance over pure Al and Mg, detailed testing indicates Al-W, Al-Mo, Al-Mg-W, and possibly Al-Mg-Mo show the best potential for fabrication. Each of these alloys exhibited marked increases in pitting potential and reduce galvanic interaction both before and after heat treating at nominal composite processing temperatures. In each case, solid solutions well beyond equilibrium solubility limits were deposited and the alloy was stable during heat treatment at 400°C. These alloys will be carried into the next phase of this program where the parameters required to deposit these alloys onto P75 fibers will be established and preliminary hot isostatic pressing (HIPing) experiments will be conducted to established the composite consolidation cycle.

Table of Contents

Table of Contents

List of Figures

List of Figures

List of Figures

List of Tables

1.0   INTRODUCTION

High modulus Gr fiber reinforced MMCs offer a wide variety of attractive properties including high specific modulus and strength (E/ρ and UTS/ρ), tailorable or zero coefficient of thermal expansion (CTE), and high thermal conductivity. Precision structures fabricated from MMCs can maintain dimensional stability when subjected to both thermal and mechanical loads. An example of a widely used satellite structure, in which the performance could be greatly improved using MMCs, is the beam compactor or beam expander secondary mirror (or sub-reflector) support structure (Figure 1-1).
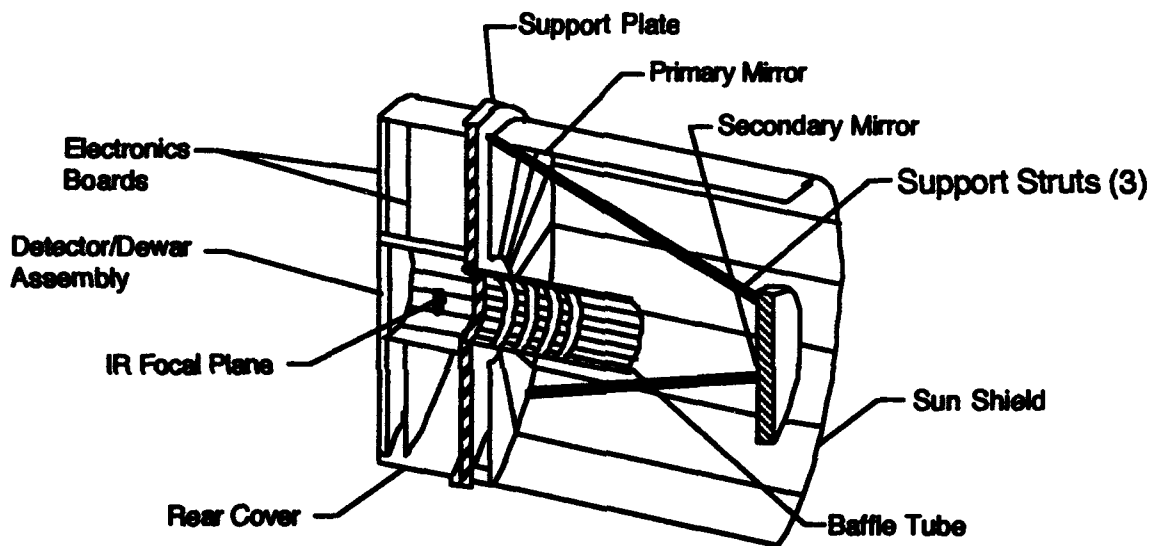
Figure 1-1. Schematic of a Staring Telescope

Unfortunately, MMCs--especially Gr fiber reinforced composites--have been found to be extremely susceptible to corrosion with severe corrosion in chloride-containing environments occurring in as little time as several weeks for Gr/Al composites [Ref. 1-3] or in just a few days for Gr/Mg composites [Ref. 4,5].

The mechanisms behind this rapid attack depend on the matrix metal, fiber, and the processing condition used to fabricate the composite. The literature reveals that pitting [Ref. 1,3,6,7], galvanic corrosion [Ref. 2,6,8,9], residual chlorides [Ref. 10], and second phase particles [Ref. 1,7,11] all contribute to the degradation of Gr/Al composites. Pitting and galvanic corrosion are intrinsic

1

corrosion problems, whereas residual chlorides and second phase particles are corrosion problems introduced through processing. There is general agreement that corrosion of Gr/Al MMCs initiates in a pitting mode [Ref. 1-3,7]. Residual chlorides (left behind during the coating fibers with the wettability promoting TiB_2) and second phase particles, such as Al_4C_3, play key roles in propagating degradation of the composite. Once the graphite fibers are exposed, the cathodic reaction on the Gr fibers accelerates corrosion of the matrix metal, ultimately leading to structural failure of the composite.

To improve the corrosion resistance of Gr MMCs, several techniques such as overcoatings, cathodic protection, and use of cathodic inhibitors have been investigated in the past. However, each of these techniques effect composite properties and only delay pitting and subsequent galvanic interaction between the metal matrix and the Gr [Ref. 1,3,6]. While some coatings have been successful in delaying the corrosion process, they do not alter the inherent corrosion resistance of the Al to pitting, and thus, they are only a temporary solution.

The overall objective of this research is to determine if nonequilibrium alloying can be used to improve the corrosion resistance of graphite reinforced MMCs. Of specific interest are improving the inherent corrosion resistance of the matrix metal and improving galvanic compatibility between the matrix and the graphite reinforcement. This program encompasses both fundamental and applied studies which will be used to produce a prototype filament wound secondary mirror support structure, like the one pictured in Figure 1-1, during the final stage of the program.

In this report, results of the first year's effort are presented and discussed. The specific objectives of the first year's research were to: 1) develop the parameters to co-sputter Mg and Al alloyed with either Cr, Mo, Ta or W, 2) characterize the corrosion behavior of these alloys by anodic polarization and galvanic corrosion experiments conducted in chloride solutions, and 3) use x-ray diffraction to characterize the alloys and investigate the solubility of Mo,W, Ta and Cr in Mg and Al. Non-equilibrium concentrations were achieved by sputtering from co-focused sources onto a rotating substrate. Over 30 alloy systems were sputtered and the corrosion properties measured. Almost all of

2

these alloys exhibited more noble pitting (E_p) and corrosion (E_{Corr}) potentials than the respective pure metals. X-ray diffraction studies of the alloys both before and after heat treatment indicated high concentration (>15 to 25 at. %) Al-Mo, Al-W, Mg-Mo, Mg-Ta, and Mg-Cr maintained the solute in solid solution.

Based on our evaluation of the 30 alloy systems, seven alloys were selected for additional studies. Of these, Al-W, Al-Mo, and Al-Mg-W appear to be the best candidates for use in a graphite reinforced MMC from both a corrosion and thermal stability standpoint.

2.0 TECHNICAL BACKGROUND

2.1 Corrosion Behavior of Gr/Metal Composites

Gr/Al has been found to be susceptible to severe corrosion in chloride environments by a number of researchers [Ref. 1-3,6-11]. In the absence of surface flaws, degradation of the composite is initiated by pitting that proceeds at a rate typical of monolithic Al alloys. Once the outer surface of the composite has been penetrated, corrosion is propagated by the cathodic reaction on the exposed graphite fibers. The large difference in corrosion potential between the matrix metal and Gr fibers drives the rapid dissolution of the matrix. It has been reported that the corrosion rate of Al can be increased eighty-fold when equal areas of Gr and Al are coupled [Ref. 10]. Internal residual chlorides, introduced during fabrication of the composite, have been found to greatly accelerate localized corrosion of the matrix. These residual chlorides at the fiber-matrix interface are by products of the coating put on the fibers to improve wettability. Also, reaction of the Gr with Al can lead to the formation of carbides at the interface which contribute to degradation.

During the past decade a variety of methods for improving the corrosion resistance of Gr/Al MMCs have been investigated with little success. These methods include: cathodic protection [Ref. 10], electrical insulation between the Gr fiber and metal matrix [Ref. 10], use of cathodic inhibitors [Ref. 10,11], and barrier coatings [Ref. 1,3,6]. Cathodic protection, which promotes the formation of hydroxyl ion, can be dangerous and is not recommended because Al is susceptible to corrosion in alkaline environments. Electrical insulation of the Gr fibers from the matrix by a continuous coating is possible, but impractical since flaws in the coating can never be totally eliminated. In addition, coatings that promote wetting always partially react with the matrix to establish a good bond, further increasing the potential for intimate fiber/matrix contact. Cathodic inhibitors, such as $ZnCl_2$ or mixtures of Na_2CrO_4 and $ZnCl_2$, show promise for decreasing galvanic corrosion [Ref. 10] through the precipitation of $Zn(OH)_2$ on cathodic sites which effectively reduces the cathodic area. However, this is difficult to put into practical use in a composite. Protective coatings such as electroplated [Ref. 1] or electroless Ni [Ref. 3,6], anodization [Ref. 3,6], chemical vapor deposition of either Ni [Ref. 3,6] or chromium carbide [Ref. 1], and organic

4

coatings [Ref. 1] have all been used to inhibit localized corrosion and seal surface flaws in the composite. Although these coatings can extend the life of the composite, its inherent corrosion resistance is still poor--leaving the composite susceptible to severe degradation when the coating is damaged. Furthermore, these coatings increase material density and may alter thermal dimensional stability of the composite. For aerospace applications, flaking of the coating onto sensitive surfaces such as detectors or reflectors, will also be a problem.

Gr/Al Metal Matrix Composite

Al immersed in an aerated aqueous chloride solution buffered to a near neutral pH, dissolves locally according to the following anodic reaction:

$$Al \rightarrow Al^{+3} + 3e^-$$

with oxygen reduction at cathodic sites proceeding by the following reaction:

$$O_2 + 2H_2O + 4e^- \rightarrow 4OH^-.$$
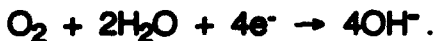
Corrosion of Al under these conditions is in the form of pits, with the majority of the surface remaining passive as shown by the dashed line in Figure 2-1. Once the electrochemically noble Gr is exposed, corrosion of the Al matrix is accelerated due to galvanic corrosion. This point is illustrated in Figure 2-1(solid line), which shows that the dissolution of Al is dramatically increased as a result of oxygen reduction taking place on the exposed Gr fibers. The rate of dissolution increases as the amount of exposed Gr fiber increases, and extensive dissolution can occur in a very short period of time.

The addition of several atomic percent of W, Ta, Cr, or Mo has been shown to substantially increase the pitting potential of sputter deposited Al as illustrated in Figure 2-2. The solute concentration need not be high to have a

5
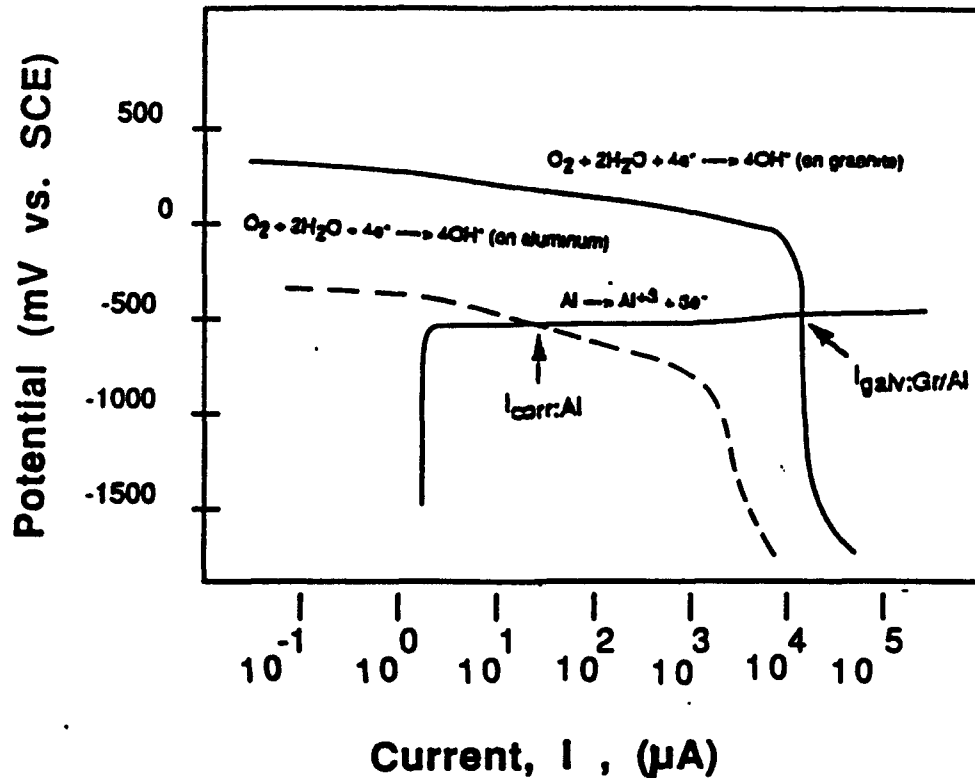
Figure 2-1. *Once exposed, the graphite in a Gr/Al composite greatly accelerates the corrosion of Al. The normal corrosion rate of Al in an aerated chloride solution, Icorr, is increased when Al is galvanically coupled to graphite, Igalv Gr/Al. In this example the corrosion rate is increased over the three orders of magnitude.*

significant impact. At a W concentration of 1.5 at. %, the average E_p is -111 mV_{SCE} (for a 0.1M KCl solution) as shown in Figure 2-3. This alloy would not undergo pitting either when exposed to an air saturated 0.1 M chloride solution or as a result of galvanic coupling to any metal or conductor with an E_{corr} less than the E_p for the alloy (~200 mV_{SCE}).

By superimposing the cathodic polarization data for Gr on the anodic polarization data for the Al-1.5 at. % W alloy, the effects of the galvanic coupling on the corrosion behavior of the Al matrix can be estimated. Figure 2-4 shows cathodic polarization data for P100 Gr fibers in aerated 3.15 wt. % NaCl (derived from reference 10), superimposed on the anodic polarization curve for the Al-1.5 at. % W alloy. This figure reveals that even at a Gr:Al area

6
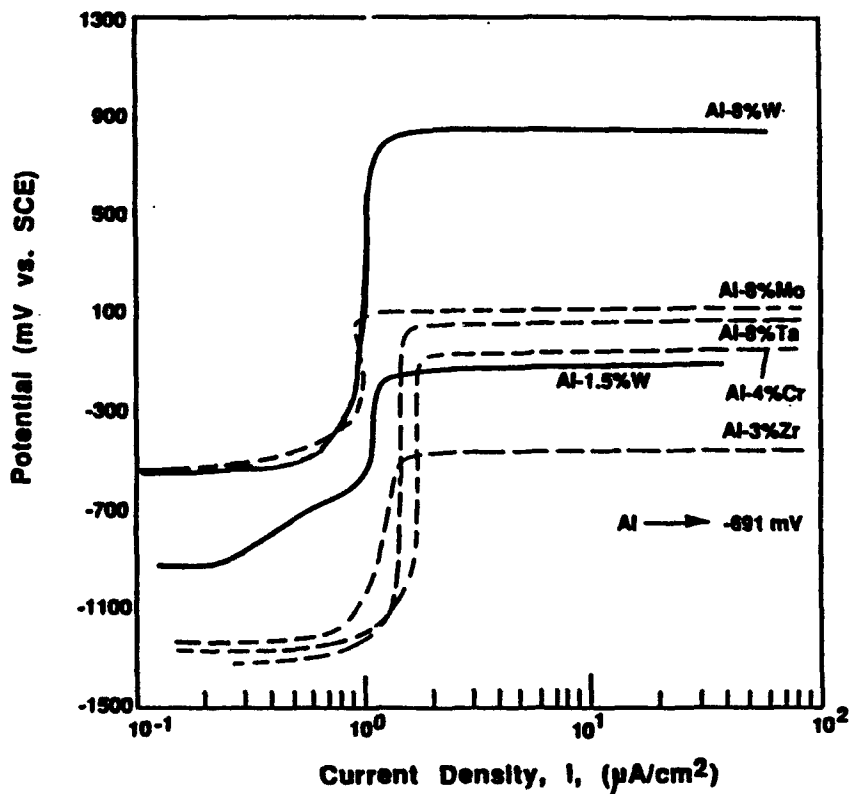
Figure 2-2. Anodic polarization behavior of a variety of non-equilibrium Al alloys in aerated 0.1 M KCl compared to the spontaneous pitting potential for Al (-691 mV vs. SCE).
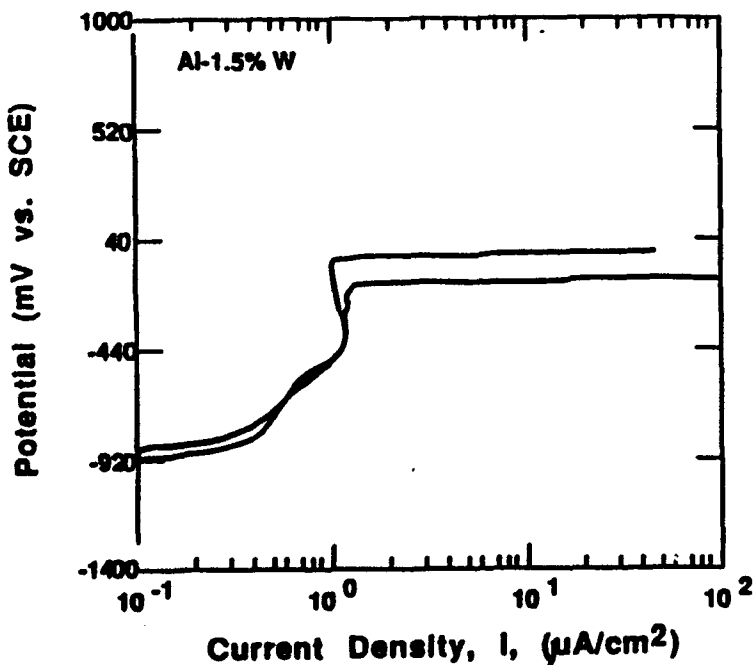
Figure 2-3. Polarization behavior for duplicate sputter-deposited Al-1.5 at. % W in an aerated 0.1 M NaCl solution.

7
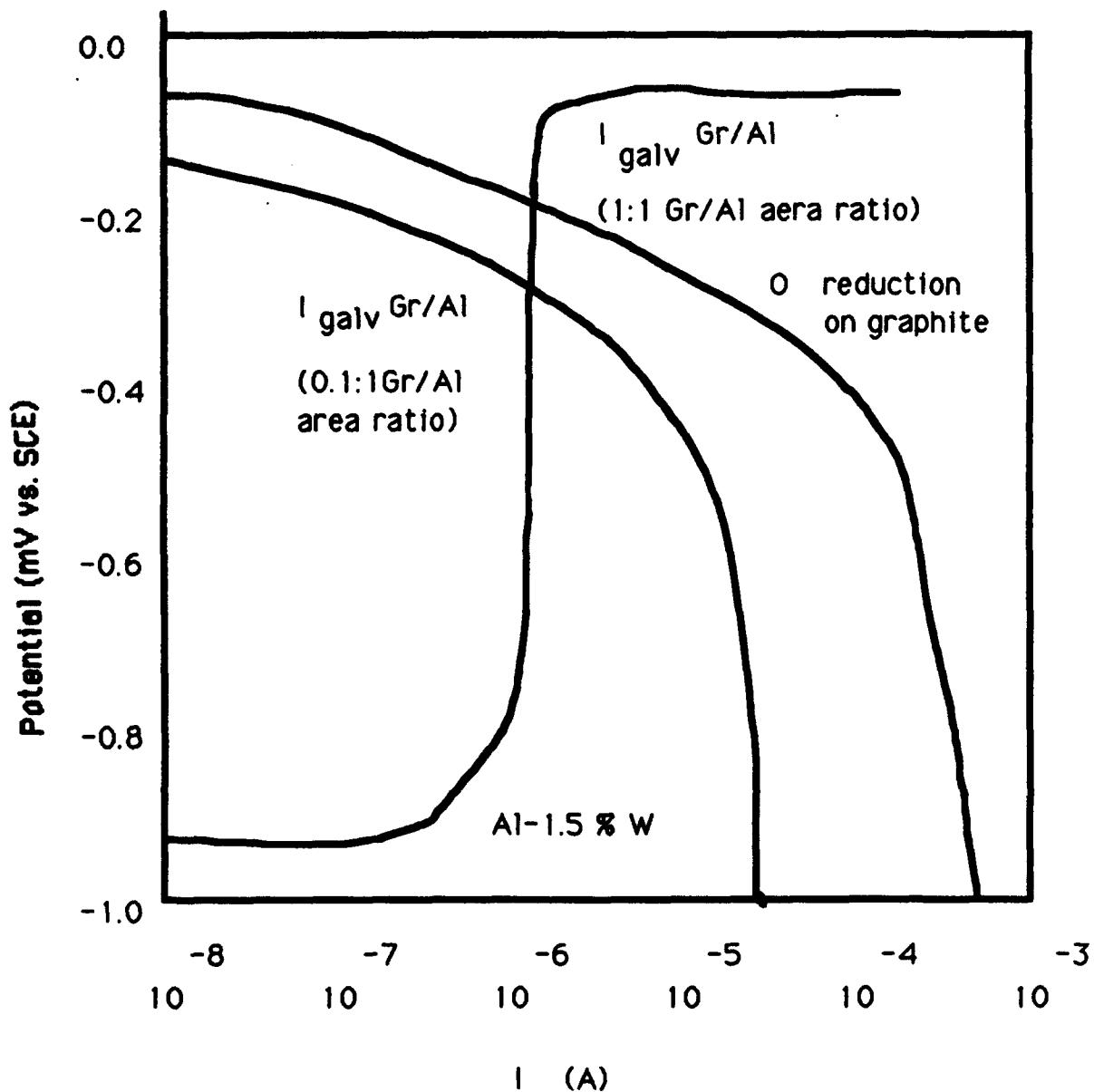
Figure 2-4. Mixed potential analysis of Gr/Al1.5 at. % W galvanic couple (cathodic data derived from Ref. 10).

ratio of 1-to-1, corrosion of the non-equilibrium Al-1.5 at. % W alloy was not accelerated as a result of galvanic coupling.

Gr/Mg Metal Matrix Composite

Magnesium in Gr/Mg composites experiences far more dramatic degradation than that observed for Gr/Al. Unlike Al, which can form a passive

film that limits attack, the surface film that forms on Mg is not very protective. For example, high purity Mg in a benign solution of sodium borate/boric acid (pH 9.3) exhibits a passive current density of 1-2 mA/cm^2 [Ref. 17]; whereas, a typical current density for Al in a near neutral pH solution is on the order of several μA/cm^2. Impurities in Mg, particularly Ni, Fe, and Cu, further increase the corrosion rate.

For Mg alloys, the rate controlling reaction is the evolution of hydrogen as opposed to reduction of oxygen as in Al alloys. Mg dissolves by the following reaction:

$$Mg \rightarrow Mg^{+2} + 2e^-$$

and in near neutral aqueous solutions, water is reduced to form hydrogen gas and hydroxyl ions:

$$2H_2O + 2e^- \rightarrow H_2 + 2OH^-$$.
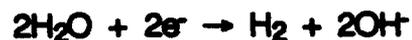
Efforts to reduce the corrosion of Mg and its alloys have focused on eliminating trace element impurities. These impurities increase corrosion by establishing microgalvanic cells within the Mg alloy since they are electropositive to Mg by several hundred millivolts. In the case of Fe, as little as 160 ppm in the Mg alloy can greatly accelerate corrosion rates [Ref. 18]. However, not all elements are deleterious to the corrosion behavior of Mg. For example, Al, which is used extensively as an alloying addition to Mg, has been shown to improve corrosion resistance. Studies of nonequilibrium alloying of Mg with 10 to 23 wt. % Al have shown that the corrosion rate can be decreased by two orders of magnitude [Ref. 22]. This decrease in corrosion rate was attributed to the formation of an aluminum rich passive film. Small concentrations of Zn and Mn have also been found to increase the corrosion resistance of Mg by minimizing the deleterious effect of Fe. The addition of 1 wt. % Zn or Mn effectively decreases the corrosion rate of Fe-contaminated Mg by almost three orders of magnitude (Figure 2-5). The end result of these efforts is an alloy that is still susceptible to corrosion, because the basic composition of the passive film is not sufficiently altered.
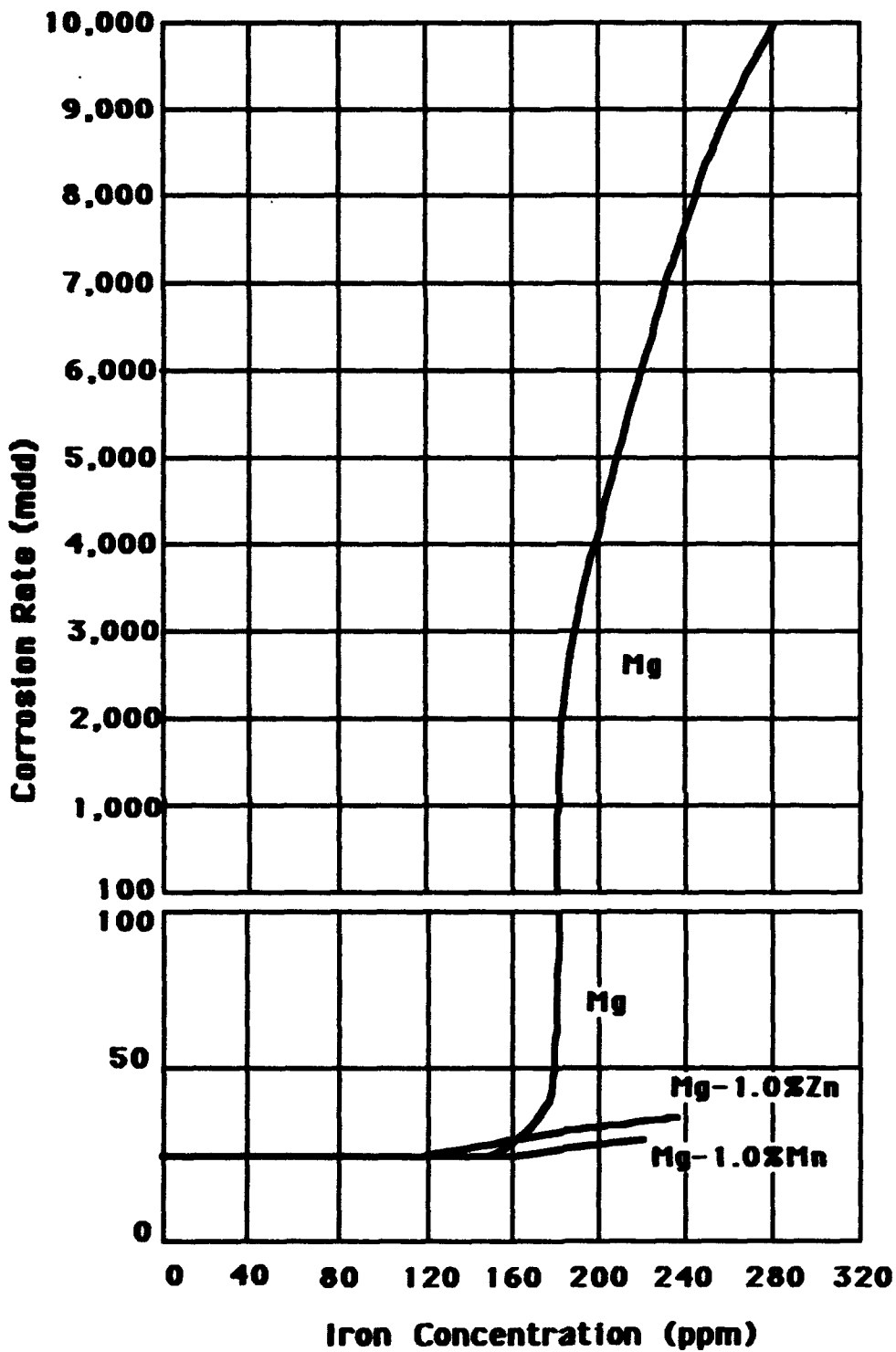
Figure 2-5. The corrosion of Mg in 3 wt. % NaCl, alternate immersion, 16 weeks, showing tolerance limit for Fe and the beneficial effect of alloying with Zn and Mn [Ref. 18].

In the case of Al, our effort focuses on improving the passivity of the alloy to eliminate, or at least minimize, galvanic attack. Magnesium on the other hand is extremely reactive, and its passive film is easily dissolved. Hence, for this metal it is necessary to add elements that not only improve passivity but also limit reactivity. To do this alloying elements must serve two roles: (1) passivate the alloy, and (2) drive the corrosion potential in the noble direction. To improve the inherent corrosion resistance of Mg, it will be essential to enhance its passivity.

One method to increase passivity is to alloy the Mg with Cr, Mo, Ta, or W in nonequilibrium concentrations. A key to this approach is to keep the solute in solid solution. Precipitation of a second phase would not only tie up the passivity enhancing species in precipitates, diminishing passivity--it would also increase corrosion through the establishment of microgalvanic cells.

Addition of certain transition metals to Al shifts the E_{corr} of the alloy several hundred millivolts in the positive direction. Table 2-1 shows this effect for Al-Mo alloys [Ref. 13] in deareated 0.1M KCl. In each case, the Mo in the alloy remains in solid solution with the Al. The increase in E_{corr} is believed to result from an increase in the exchange current density for the reduction reaction (in this case - hydrogen evolution), as illustrated in Figure 2-6. The Mo addition effectively catalyzes the hydrogen evolution reaction on the surface of the alloy and in the process shifts the open circuit potential more noble. We have noticed similar shifts in the E_{corr} of Al alloyed with Ta and W in both aerated and deareated in 0.1M KCl solutions. Figure 2-7 shows approximate exchange current densities for the hydrogen evolution reaction on a number of metals as a function of their location in the periodic table [Ref. 20]. Al and Mg both have low

Table 2-1. Effect of Mo in Al on E_{corr}.

[Mo] at.%	Eoc mV vs SCE
0.0	- 1405
2.8	- 1002
5.4	- 953
7.1	- 877
10.4	- 883
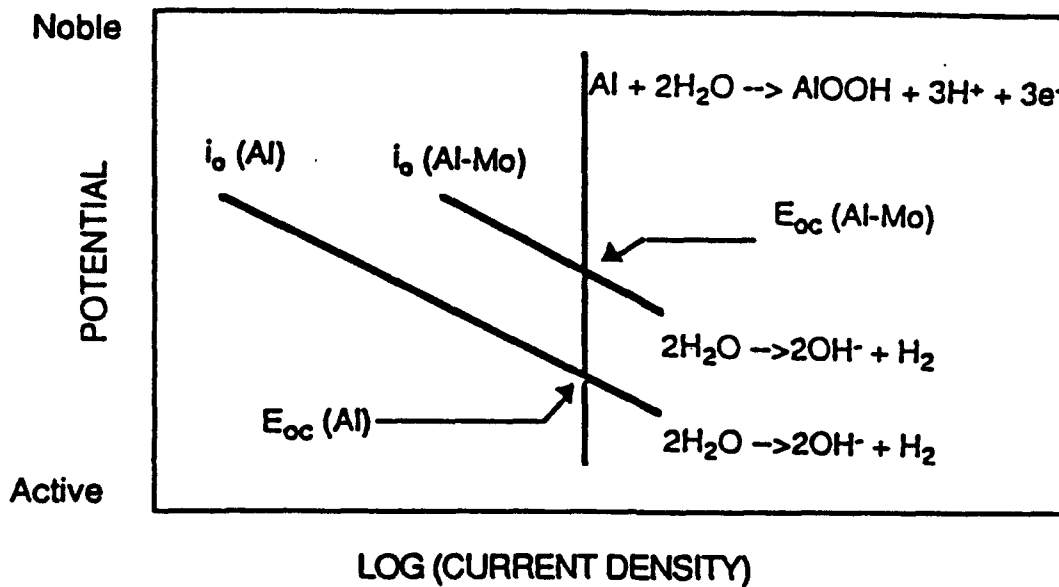
Figure 2-6. The effect of the exchange current density on E_{corr} [Ref. 12].

Figure 2-7. Hydrogen exchange current density related to the periodic classification of elements [Ref. 20].

exchange current densities, whereas the exchange current densities of Mo, Ta, and W are three orders of magnitude higher. If the E_{corr} of Mg could be shifted through solid solution alloying with elements such as Mo, Ta, or W, then the galvanic compatibility of Mg with Gr could be significantly enhanced.

2.2 PHASE EQUILIBRIUM

In general, the solubility of Group Vb and VIb transition metals in either Al or Mg is extremely limited. In fact, none of these transition metals have been found to have even small solid solubility limits in Mg. Aluminum, on the other hand will retain small amounts of the Group Vb and VIb transition metals in solid solution.   Each of the Al-Group Vb and VIb alloy systems exhibits a peritectic reaction on the Al rich side. Solid solubility limits average less than 0.5% for the Group Vb and VIb metals in Al. A few details of each of the binary systems investigated in this program and their corresponding phase diagrams are presented in the following paragraphs. Although investigators are cited in each section, all data was found in ASM Binary Phase Phase Diagrams, Second Edition. [Ref. 21]

Mg-Cr
Although a phase diagram does not exist for the Mg-Cr system, Montignie has suggested the formation of $CrMg$, Cr_2Mg_3, $CrMg_3$, and $CrMg_4$. However, these postulated phases have not been experimentally verified and have been questioned because at any given temperature, Cr cannot be in equilibrium with several intermetallic phases.

Mg-Mo
Investigations by Sauerwald and Climax Molybdenum Company reported that Mo does not alloy with Mg. Therefore, the phase diagram is simply elemental Mg and elemental Mo for all concentrations.

Mg-Ta
Although a phase diagram does not exist, Gulyae has suggested the Mg-Ta system will have a peritectic reaction at 652°C with an estimated 0.1 to 0.2 at. % of Ta in Mg. However, no data currently exists for this binary system.

13

Mg-W

Similar to the previous 3 systems, no phase diagram exists for the Mg-W binary alloy system. Studies by Kremer and Sauerwald and Busk concluded that Mg does not alloy with W.

Al-Cr

The Al-Cr phase diagram, shown in Figure 2-8, is based on experimentation and thermodynamic calculations. On the Al rich side there is a peritectic reaction at 661.45°C with Al alloyed with 0.35 at. % Cr. As the Cr concentration increases, a two phase field of Al and the Al_7Cr intermetallic is found. As the concentration of Cr is further increased, a series of intermetallic compounds with increasing Cr:Al ratio can form. For Cr concentrations of 1 to 10 at. % the phase diagram indicates heat treating may result in decomposition of the solid solution to Al and Al_7Cr.

Al-Mo

Examining the Al-Mo phase diagram in Figure 2-9, the solid solubility of Mo in Al is very low. At 0.077 at. % Mo there is a peritectic reaction of liquid and $Al_{12}Mo$ to Al. For Mo concentrations between 0.07 and 7.9 at. %, the equilibrium phases are Al and $Al_{12}Mo$; and from 7.9 to 16.8 at. % the equilibrium phases are Al_5Mo and $Al_{12}Mo$. Early work with rapidly quenched alloys extended the concentration of Mo in Al up to 2.7 at. %.

Al-Ta

The Al-Ta phase diagram is shown in Figure 2-10. Solid solubility of Ta in Al is limited to less than 0.04 at. %. Above this concentration, up to 24 at. % Ta, there is a two phase region of Al and $TaAl_3$.

Al-W

Similar to all the Al-Group Vb and VIb alloys, the Al-W phase diagram shows a peritectic reaction on the Al-rich side (Figure 2-11). Solubility of W in Al is virtually zero. At room temperature, the equilibrium phase consists of Al and γ-$Al_{12}W$ for compositions between 0 and 8 at. % W. From 8 to 17 at % W, the equilibrium phases are $Al_{12}W$ and Al_5W.

14
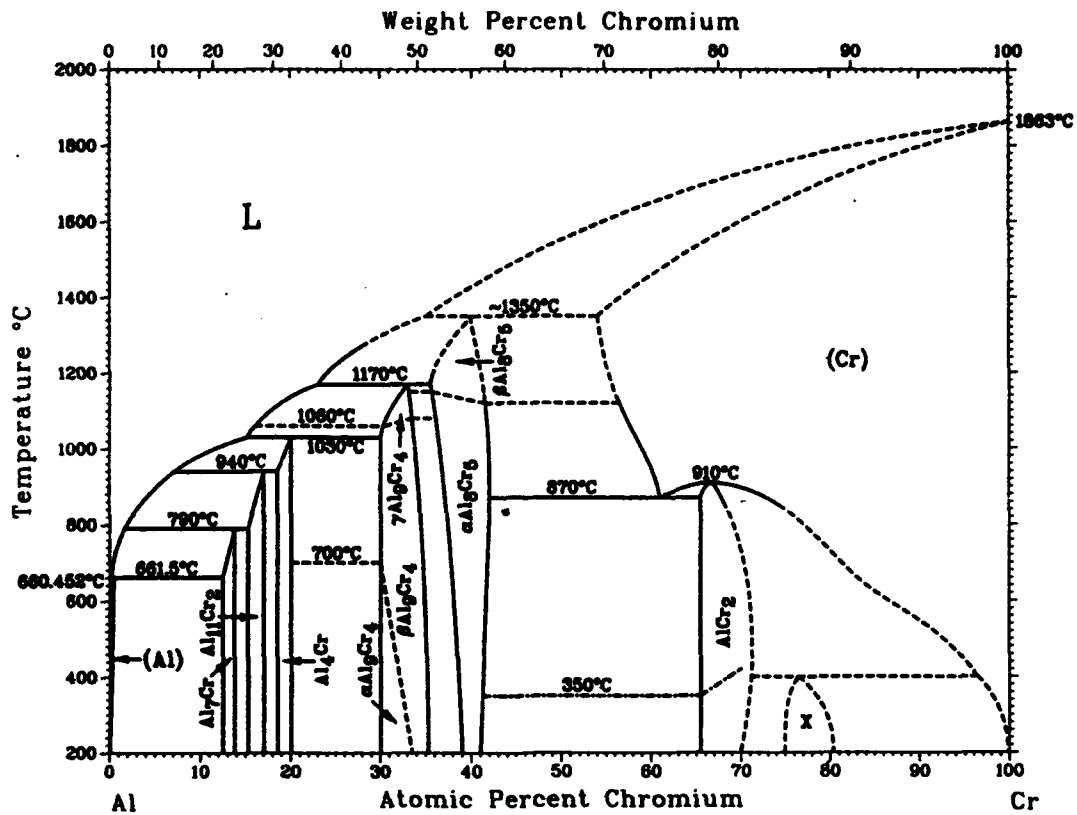
Figure 2-8. Aluminum-Chromium Phase Diagram [Ref. 21]

Figure 2-9. Aluminum-Molybdenum Phase Diagram [Ref. 21].

Weight Percent Aluminum
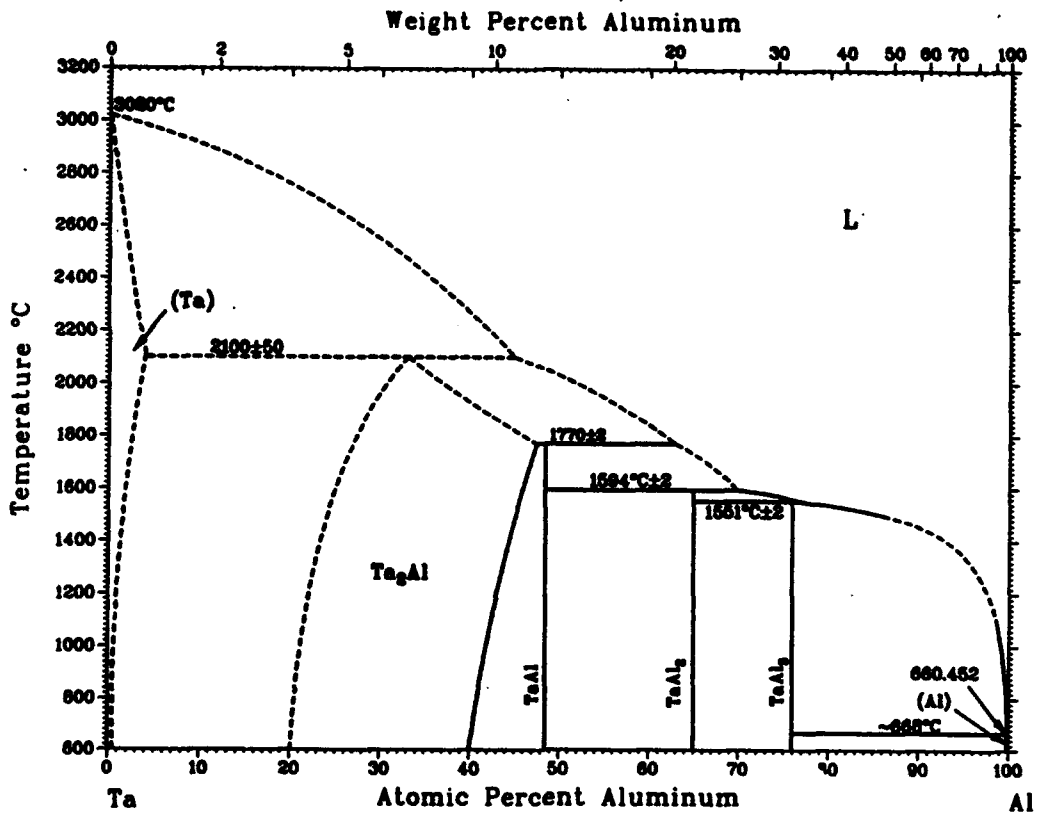
Figure 2-10. Aluminum-Tantalum Phase Diagram [Ref. 21].

Weight Percent Tungsten
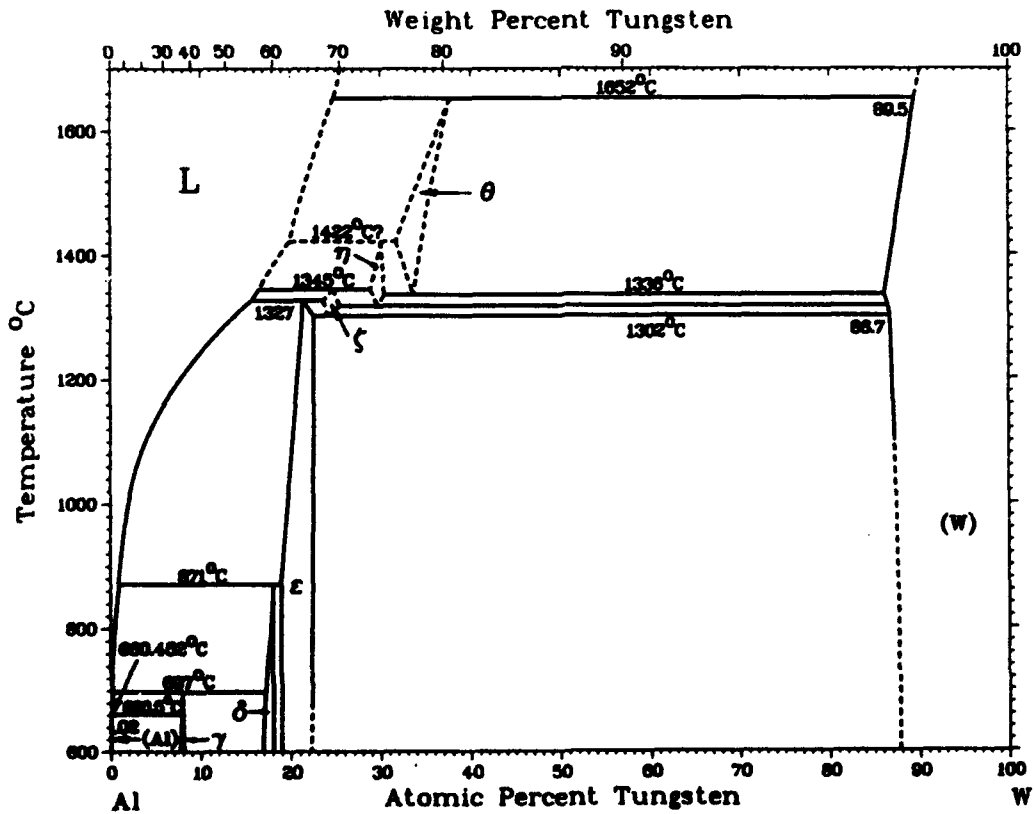
Figure 2-11. Aluminum-Tungsten Phase Diagram [Ref. 21].

16

3.0 EXPERIMENTAL PROCEDURE

Development of the corrosion resistant, nonequilibrium Mg and Al alloys was divided into two phases. In the first phase, several alloys were sputtered with various compositions and tested to assess their corrosion resistance and thermal-stability. Seven of these alloys were then chosen for more detailed corrosion testing and thermal and mechanical evaluation in phase 2.

During the first phase, sputtering rates were determined for Mg, Al, and each of the Group Vb and Vlb transition metals. Alloy compositions were predicted from the rate data and the sputter power conditions were adjusted to obtain a range of desired alloy compositions. Three to six alloys were sputtered from each binary system and compositional analysis was conducted using either energy dispersive x-ray spectroscopy (EDS) or inductively coupled plasma (ICP). X-ray diffraction (XRD) of each film was conducted to determine whether the solute was deposited during sputtering in solid solution and also if it remained in solid solution after heat treating at typical HIP processing temperatures. Concurrently, anodic and cathodic polarization curves were generated on each alloy to assess corrosion performance.

In the second phase of the program, the alloys with the best performance from phase 1 (in terms of corrosion resistance and thermal stability) were selected for further evaluation. These alloys were sputtered onto both Si wafers and Gr coupons for more detailed thermal stability and corrosion testing. XRD was conducted both before and after heat treatment at 400°C to determine if a second phase precipitated and to assess reactivity of the alloy with Gr. Anodic potentiodynamic polarization behavior was evaluated on both Si and Gr substrates. In order to investigate the galvanic compatibility of the alloys with Gr, galvanic current diagrams and galvanic current measurements were used.

3.1 602RS Loadlock Thin Film Deposition System

A 602RS Loadlock Thin Film Deposition System was used to deposit the binary and ternary Al and Mg alloys. The chamber is a box construction, 43 x 66 x 61 cm, with three co-focused cathodes that allow for a large range of alloy

compositions. Each cathode holds a 7.6 cm dia. x 0.32 cm thick target which is sputtered onto a 100-mm dia. rotating substrate holder. Cathode 1 is interfaced with an Advanced Energy (AE) MDX 1.5K power supply which provides 1500 watts at a maximum of 700 volts direct current (VDC). Power for cathode 2 is switchable for either DC or radio frequency (RF) operation. DC power is supplied by an AE MDX 1.5K which regulates power up to 1500 watts (W) at 500 VDC. RF for cathode 2 is supplied by an AE RFX-600 interfaced with an AE ATX-600 tuner. An in-line blocking filter was installed to prevent RF power from translating back to the DC power supply. The third cathode is RF power only which is supplied with an AE RFX-600 and the power conditions are tuned with the AE ATX-600. In addition, the substrate holder can heat treat specimens prior to, or during, deposition. Vacuum is maintained using a CTI Cyrotorr-8 vacuum pump that is rough pumped with a Alcatel-Drytel 100 turbomolecular drag pump. Contamination free films can be achieved because both of the vacuum pumps are oil-free and substrates are transferred into the main chamber through a loadlock that is evacuated with the turbopump. The load lock can be evacuated to approximately 10^{-5} torr within 3 min. which allows for rapid transfer of specimens into the sputter chamber, thereby avoiding any possible contamination that may be experienced by opening the chamber. During sputtering, gas is introduced at a specified flow rate and the sputtering pressure is controlled between 1.0 and 100 millitorr with a VAT, Inc. Series 64 Pressure Controller. Sputtering pressure is regulated by a combination of gas flow rate and the conductance of the high vacuum valve between the cyropump and chamber. Substrate rotation during deposition results in uniform films with a variation in the thickness of no more 0.1% from center-to-edge. Typically, the substrate is rotated at a speed of 30 rpm. All systems and subsystems are controlled by an IBM PS/2 50Z computer that allows for fully automatic operation.

3.2 Sputtering Rate Determination

Prior to depositing the alloys, sputtering rates for Al, Mg, Cr, Mo, Ta, and W were determined by sputtering films onto glass slides that were partially masked. Step heights between the coated and uncoated regions were measured using a Sloan Dektak II Profilometer with a ±5.0 nm accuracy. Three profilometer scans of between 3 and 8 μm were conducted on each glass slide

to obtain an average rate. Each element was sputtered at different power settings to obtain sputter rate versus power curves. Rate was calculated by dividing film thickness by total deposition time.

3.3 Alloy Development and Characterization

Binary alloys were deposited onto 10-cm dia. Si wafers using the predetermined sputter rates for each element. The wafers were then cleaved into smaller sections for compositional analysis, XRD, heat treatment, and corrosion testing.

Upon removal from the sputtering system load lock chamber, the alloy was immediately visually inspected and the appearance recorded. Distinguishing features such as reflectivity, cloudiness, color and surface roughness were all noted.

A total of 60 alloys were fabricated in the first phase of this task. The alloys which exhibited the best overall corrosion behavior were selected for more detailed study in phase 2. Thes new films were sputtered onto both Si and Gr substrates for corrosion testing and characterization, and a section of each film was heat treated for 1 h at 400°C.

A JEOL 840 Scanning Electron Microscope (SEM) was used to examine the microstructure of each alloy. EDS compositional analysis was performed during SEM analysis. A semi-quantitative computer program was used to analyze x-ray spectra by comparing the acquired peaks to a library of references stored on disk. The computer program uses a multiple squares analysis to accurately measure peak intensities, remove background, and to unfold overlapping peaks. Conditions for the EDS analysis were kept constant for all films to reduce error. Conditions for the EDS analysis were as follows:

Voltage:	15 kV
Magnification:	350 X
Working Distance:	35 mm
Counts/s In:	1400 to 1800
Acquisition Time:	100 sec

Each alloy was analyzed in three locations to obtain an average composition and to determine if the composition varied with position. In addition, compositions of several alloys were measured by direct current plasma emission (inductively coupled plasma (ICP)) using a Beckman Spectraspan VI.

X-ray diffraction using a Rigaku Rotoflex 12 kW rotating anode unit was conducted on each film to ensure that the solute was in solid solution with either Al or Mg. This was done immediately after sputtering and following heat treatment at 400°C for 1 h. Intensity versus diffraction angle (2θ) was measured for each alloy before and after heat treating and plotted together for direct comparison of the effect of heat treatment on the thermal stability of the alloy.

Heat treating was conducted in the DV-602 RS Thin Film Deposition chamber fitted with a hot stage. The procedure involved bringing the stage to 400 °C while the specimens were in the load lock. Following this, the specimens were transferred into the chamber for heat treatment for one hour and then removed through the load lock. During the heat treating process, a pressure of 100 millitorr was maintained in the chamber with high purity Ar as the cover gas.

3.4 Corrosion Testing

Potentiodynamic Polarization Measurements

Over 160 anodic potentiodynamic polarization experiments were conducted on the Mg alloys and over 50 scans were generated on the Al alloys using either an EG&G Princeton Applied Research (PAR) Model 273 Potentiostat or a EG&G PAR Versastat Potentiostat which were computer controlled with Model 352 software. For this year's investigation the alloys were deposited onto glass, Si single crystal wafers, and graphite. In the case of the graphite and glass substrates, the specimens were tested using an EG&G PAR Model K0235 flat cell. For the alloys deposited onto Si single crystal wafers, individual specimens were prepared from cleaved portions of the wafers by attaching a coated lead wire and masking the connections and the back and edges of the

20

specimen with a marine epoxy paint (Interlux 404/414). Polarization curves were generated at scan rates ranging from 1 mV/s to 0.008 mV/s with the majority of tests being conducted at a rate of 0.2 mV/s. The experiments were conducted in 0.1M NaCl with the pH adjusted to 8 (a few experiments were conducted at a pH of 10) and a few were also conducted in artificial seawater (conforming to ASTM std D1141). Most experiments were conducted without aeration--a condition which is more reproducible than attempting to maintain a constant level of aeration for a large number of experiments. All experiments were conducted on at least duplicate specimens at ambient room temperature (23 to 27 C). After immersion and prior to polarization, the open circuit potential for the Al specimens were allowed to stabilize for at least 1 hour. For most of Mg alloy experiments, E_{corr} was allowed to stabilize for only a few minutes since exposure to these solutions for one hour prior to polarization often resulted in total loss of the thin film. As a result of the pseudo-passivation observed for the Al-Ta alloys it was possible to allow E_{corr} for these specimens to stabilize for 1 hour prior to polarization. All potentials given in this report are relative to a saturated calomel reference electrode (SCE).

Cathodic polarization behavior of the brittle P75 graphite was evaluated using fibers which had been embedded in a dielectric polyetheretherketone (PEEK). The top and one edge of the PEEK graphite sample were abraded with 600 grit paper to expose the fibers and a lead wire was attached to the top of the specimen. Prior to testing, all but the one abraded surface of the specimen was coated with a marine epoxy paint. The surface area of the graphite was determined by measuring the tested surface area and multiplying it by the fiber volume fraction (53.8%) which was calculated with a Buehler Omnimet II Image Analyzer. Cathodic polarization scans were conducted at a scan rate of 0.2 mV/s under the same conditions as described above.

The galvanic corrosion performance of nonequilibrium alloy/graphite couples was estimated using galvanic current diagrams [Ref. 23]. In these diagrams, the anodic curves for the alloys are superimposed on the cathodic polarization curve for Gr. Assuming an insignificant IR drop between the metal and the Gr, no contributions from reverse reactions, and uniform current distribution, the intersection of the anodic and cathodic curves can be used to estimate the current present in a galvanic couple.

Galvanic Testing

Galvanic testing was performed by coupling the alloys to the P75 graphite specimens through an ESC Model 440 multichannel potentiostat/zero resistance ammeter (operating in the ZRA mode) and monitoring the galvanic current as a function of time. These 1 week experiments were conducted in non-aerated 0.1 M NaCl for the Al and Al alloys and artificial seawater for the Mg and Mg-Cr alloy.

4.0 RESULTS

4.1 PHASE 1: Preliminary Alloy Development and Testing

4.1.1 Sputter Deposition Rate Evaluation

Sputtering rates for Al, Mg, Cr, Mo, Ta, and W were determined using a Dektak profilometer and are plotted in Figures 4-1 and 4-2. For Al and Mg, sputtering rates were determined using both DC and RF power. The rate for DC sputtering is approximately double that of the RF rate. For example, at ~240 W, Al sputtered at a rate of 0.29nm/s DC and 0.16nm/s RF. Similarly, Mg sputtered at a rate of 1.07nm/s DC and 0.43nm/s RF. This also shows that the deposition rate of Mg is approximately triple the rate of Al for both DC and RF sputtering. DC sputtered films were very cloudy for Mg and less specular for Al. Therefore, although the sputtering rate was higher for DC, RF was selected to fabricate the alloys. If higher rates for Al or Mg were needed, two sources were used.
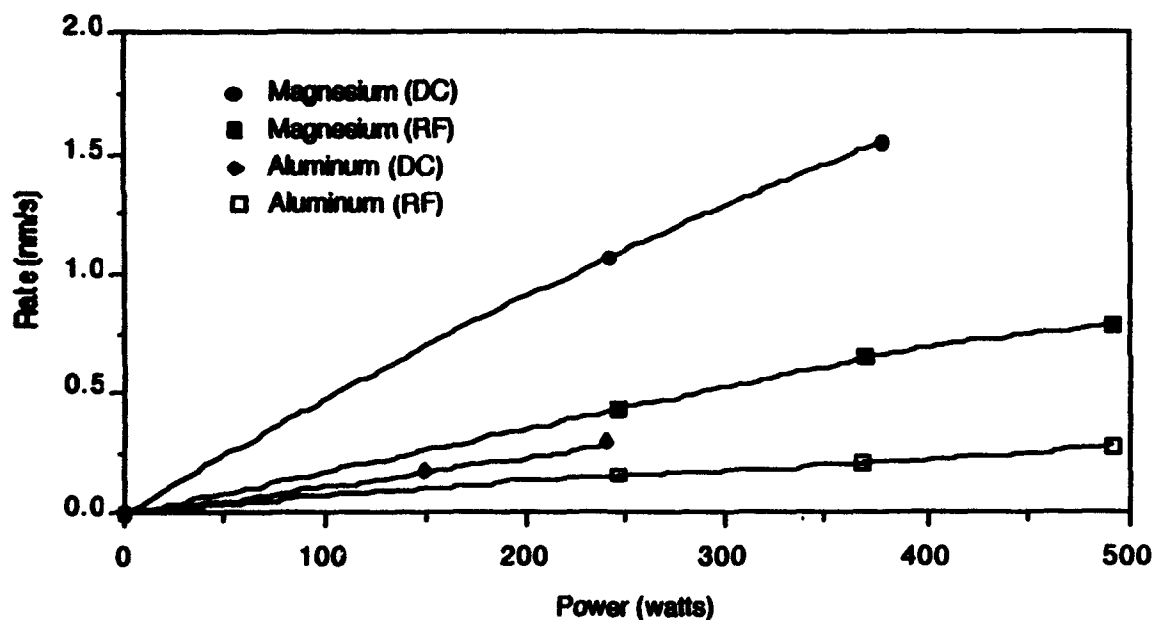
Figure 4-1. Deposition rate for DC and RF sputtered Mg and Al determined using Dektak profilometer measurements.
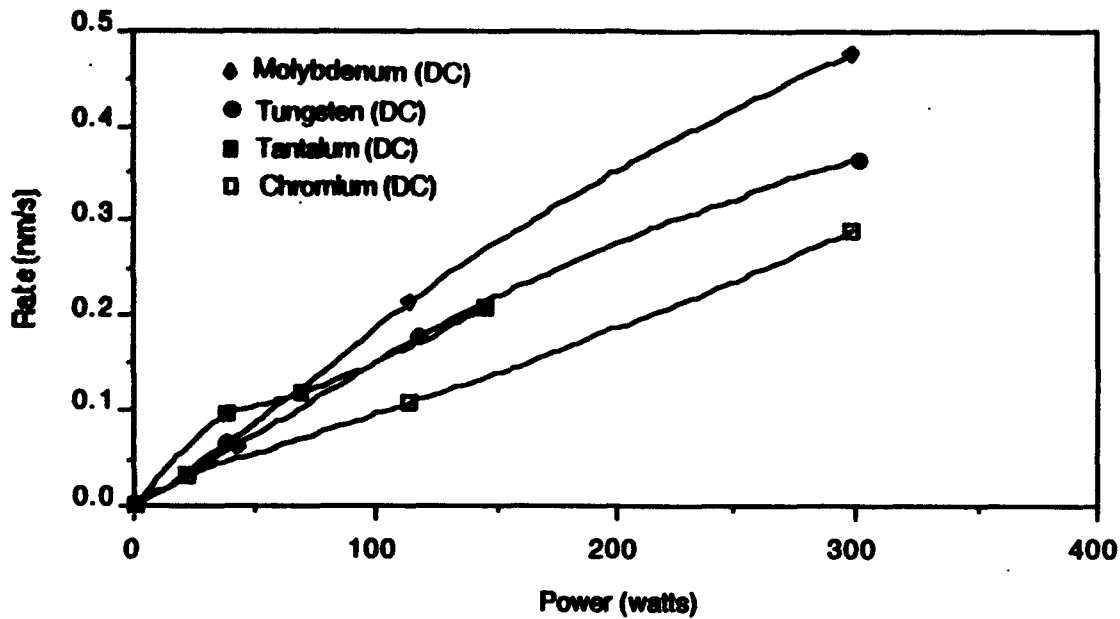
Figure 4-2. *Deposition rate for DC sputtered Cr, Ta, Mo, and W determined using Dektak profilometer measurements.*

Rates for Cr, Mo, Ta, and W using DC power are also plotted in Figure 4-2. Comparing the rate at similar power settings indicated Cr sputtered at the slowest rate, and Mo sputtered at the highest rate. For example, for a power setting of 241 W, deposition rates were measured at 0.23 nm/s, 0.39 nm/s, 0.35 nm/s, and 0.37 nm/s for Cr, Mo, Ta, and W, respectively. To achieve atomic percents between 1 and 10%, deposition rates were also measured at much lower cathode power. Sputtering rates at 38 W DC were measured at 0.037nm/s, 0.064nm/s, 0.10nm/s, and 0.063nm/s for Cr, Mo, Ta, and W, respectively.

4.1.2 Alloy Development

Using the sputter rates determined above, target alloy compositions as a function of the cathode power were calculated. Composition was predicted using the following relationship:

$$\text{solute (at. \%)} = \frac{R_1\rho_1/MW_1}{R_1\rho_1/MW_1 + R_2\rho_2/MW_2} \times 100 \qquad (1)$$

where R is the measured sputtering rate, ρ is the density, MW is the molar weight, and the subscripts 1 and 2 refer to the solute and primary binary alloy constituent (Al or Mg), respectively. To obtain solute concentrations between 0.5 and 10 at. %, the lowest power settings were required. For example, power settings of 1%, 2%, and 3% were used for DC sputtering the solute, which corresponded to 7, 22, and 38 W, respectively.

Alloys were sputtered from 30 to 120 minutes to achieve a desired thickness of no less than 2μm. Visual appearance of each alloy was recorded upon removal, after sputtering, and after heat treating. For the most part, each alloy had a highly reflective metallic appearance indicating low oxide content. A few exceptions were the 2 gun Mg alloys, which had a cloudy oxidized appearance. This was attributed to an increased grain size resulting from the rapid deposition rate.

4.1.3 Compositional Analysis

Compositions measured by EDS and ICP are listed in Table 4-1 for the Mg-Group Vb & VIb alloys and the Al-Group Vb & VIb alloys. Examination of this data reveals good correlation between EDS semi-quantitative values and the predicted composition values. Differences between measured and predicted values likely resulted from errors in the rate calculation perturbated from the Dektak measurements and from semi-quantitative EDS analysis due to the high absorption metals in the alloys.

Closer examination of the Mg alloy data shows solute concentrations fall into two ranges based on whether two guns or one gun of Mg was co-sputtered with the solute element. When two guns of Mg were sputtered, solute concentration ranged from 0.5 at. % to 4.0 at. %. Using one gun of Mg at 480 W resulted in solute concentrations between 3 and 13 at. % depending on the solute sputter source power.

Two exceptions to these ranges were the Mg-1.5 at% Mo, Mg-4.6 at.% Mo, Mg-7.6 at.% Mo alloy sets and the Mg-1 at.% W, Mg-4.5 at.% W, Mg-7.4 at.% W alloy sets. For these alloys the solute concentration was much lower

Table 4-1. *Alloy composition measured by either Semi-Quantitative Energy Dispersive X-ray Spectroscopy on a SEM or Inductively Coupled Plasma.*

Alloy	Alloy Designation	Alloy Composition (at. %)		
		Predicted	EDS	IPC
Mg-Cr	Mg480.C.Cr10.S.20106.1	1.7Cr	2.4Cr	2.65
	Mg480.C.Cr20.S.20106.1	5.1Cr	7.2Cr	
	Mg480.C.Cr40.S.11215.1	8.5Cr	11.8Cr	
Mg-Mo	Mg480.C.Mo10.S.10906.1	1.5Mo	0.9Mo	
	Mg480.C.Mo20.S.10906.1	4.6Mo	1.8Mo	
	Mg480.C.Mo40.S.10906.1	7.6Mo	2.3Mo	
	Mg2/480.C.Mo10.S.11025.1	0.9Mo	-	
	Mg2/480.C.Mo20.S.11025.1	2.8Mo	1.3Mo	
	Mg2/480.C.Mo40.S.11025.1	4.7Mo	2.4Mo	1.35
Mg-Ta	Mg480.C.Ta10.S.11210.1	2.7Ta	3.0Ta	
	Mg480.C.Ta20.S.11210.1	8.2Ta	7.3Ta	
	Mg480.C.Ta40.S.11210.1	13.3Ta	13.0Ta	
	Mg2/480.C.Ta10.S.11030.1	1.2Ta	1.2Ta	
	Mg2/480.C.Ta20.S.11030.1	3.5Ta	2.9Ta	
	Mg2/480.C.Ta40.S.11030.1	5.9Ta	4.6Ta	1.39
Mg-W	Mg480.C.W10.S.10825.1	1.0W	-	5.31*
	Mg480.C.W20.S.10825.1	4.5W	-	
	Mg480.C.W40.S.10825.1	7.4W	-	11.44†
	Mg480.C.W10.S.11207.1	1.0W	3.2W	
	Mg480.C.W20.S.11207.1	4.5W	8.2W	
	Mg480.C.W40.S.11207.1	7.4W	12.1W	
Al-Cr	Al2/480.C.Cr10.S.11004.1	2.4Cr	5.2Cr	
	Al2/480.C.Cr20.S.11004.1	7.3Cr	9.3Cr	
	Al2/480.C.Cr40.S.11004.1	12.0Cr	12.6Cr	11.61
Al-Mo	Al480.C.Mo10.S.10825.1	4.3Mo	-	
	Al480.C.Mo20.S.10825.1	12.3Mo	-	
	Al480.C.Mo40.S.10825.1	19.6Mo	-	25.9
Al-Ta	Al2/480.C.Ta10.S.11005.1	2.8Ta	6.38Ta	
	Al2/480.C.Ta20.S.11005.1	8.2Ta	10.48Ta	
	Al2/480.C.Ta40.S.11005.1	13.4Ta	16.27Ta	8.16
Al-W	Al480.C.W10.S.10825.1	4.1W	21.7	
	Al480.C.W20.S.10825.1	12.1W	33.0	
	Al480.C.W40.S.10825.1	19.0W	40.0	25.57
	Al2/480.C.W10.G.11117.1	2.1W	5.32	
	Al2/480.C.W20.G.11117.1	6.4W	7.64	
	Al2/480.C.W40.G.11117.1	10.5W	10.36	

* 16.51 At. % Al, † 16.9 At. % Al

even though the same power was used. These were the first two alloy families sputtered, and it appears that the deposition rate of Mg significantly decreased. We believe this was due to reduction in the magnetic strength of the Co-Sm magnets as a result of overheating the targets during sputtering. Reduction in magnetic field strength caused a reduction in plasma confinement at the target and subsequent reduction of the sputtering rate. An early deposition rate measurement for the Mg was 4.6 nm/s as compared to approximately 1.2 nm/s for cathode 2 and 0.8nm/s for cathode 3 measured later on during the program. These rates were based on films sputtered at 480 W and 7.0 millitorr Ar gas pressure.

Solute concentrations for the Al binary alloys were much higher due to the low sputter rate of Al; 0.28nm/s compared to 1.2 nm/s for Mg at 480 W and 7.0 millitorr Ar. As an example, the Al480.C.W40 had a measured W concentration of 25 at. % as compared to 12 at. % for the Mg480.C.W40 alloy. Solute concentrations ranged from 8 to 25 at. % for one gun Al, and from 2.5 to 14 at. % when two guns of Al were co-sputtered with the solute element. Our investigation focused on using two guns of Al co-sputtered with the solute element to keep to solute concentrations between 2 and 10 at. %.

4.1.4 Microstructural Examination

All the Al-based binary alloys were featureless with no resolvable grain size up to the limit of the SEM, which was approximately 50,000X. One exception was the Al-Ta alloys, where small particles of Ta were found on the surface.

Many of the Mg-based alloys were also featureless and the grain structure was too fine to resolve. However, for the Mg-Mo alloys, a grain structure was resolvable as shown in Figures 4-3 and 4-4. The Mg-0.9 at.% Mo, Mg-2.8 at.% Mo and Mg-4.7 at.% Mo alloys had an average grain size of ~0.3 μm (Figure 4-3). For the Mg-1.5 at.% Mo, Mg-4.6 at.% Mo, and Mg-7.6 at.% Mo alloys, SEM (Figure 4-4) revealed a grain size of ~0.25μm. In both cases, large ~0.05 μm voids were found between grains.

SEM examination also revealed small particles of Ta on the surface of the

27

a)

0003　10KV　X10,000　1Pm　WD20

b)

0002　10KV　X30,000　1Pm　WD20
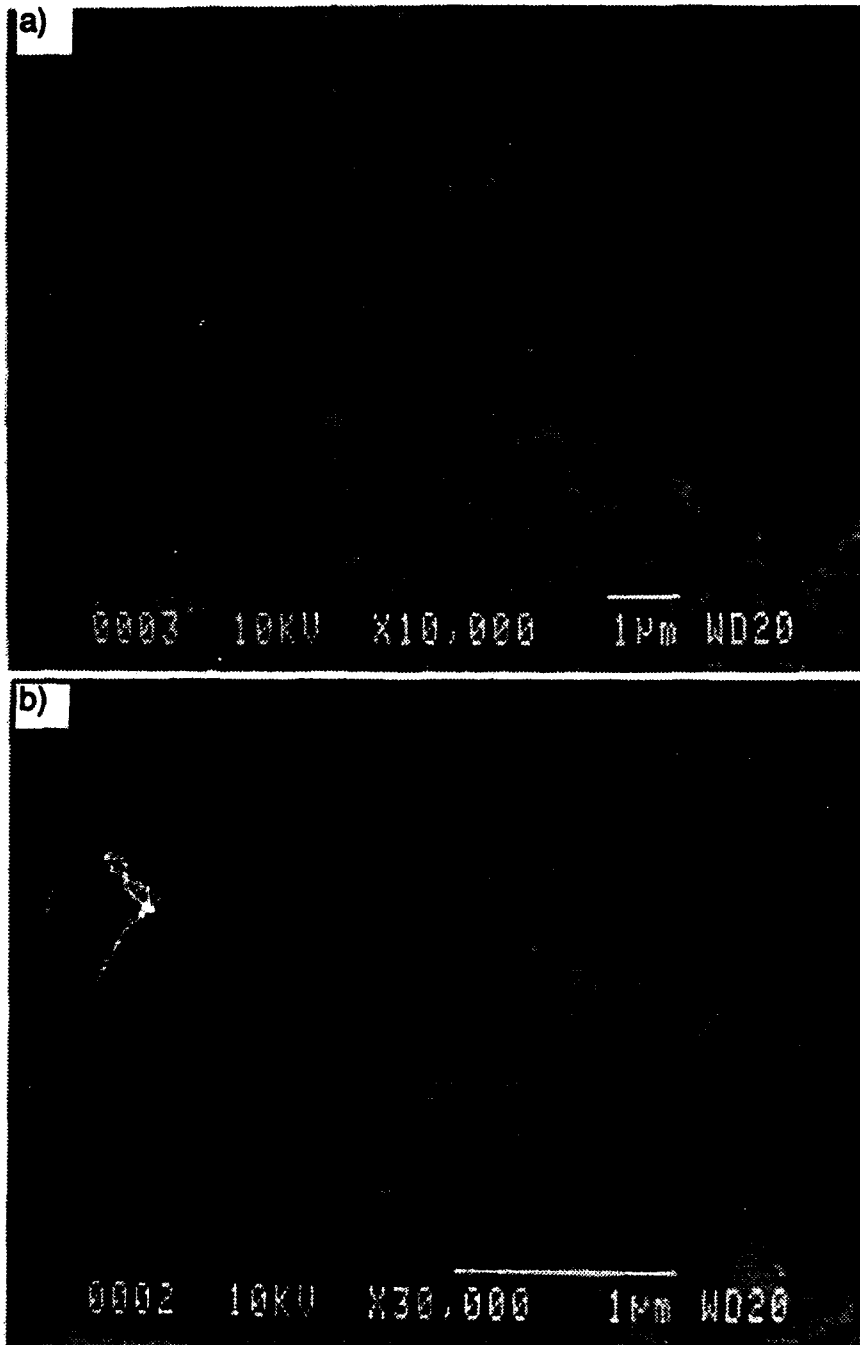
Figure 4-3. SEM Photomicrographs of Mg2/490.C.Mo40.S.11025.1
showing ~0.3μm hexagonal grains.
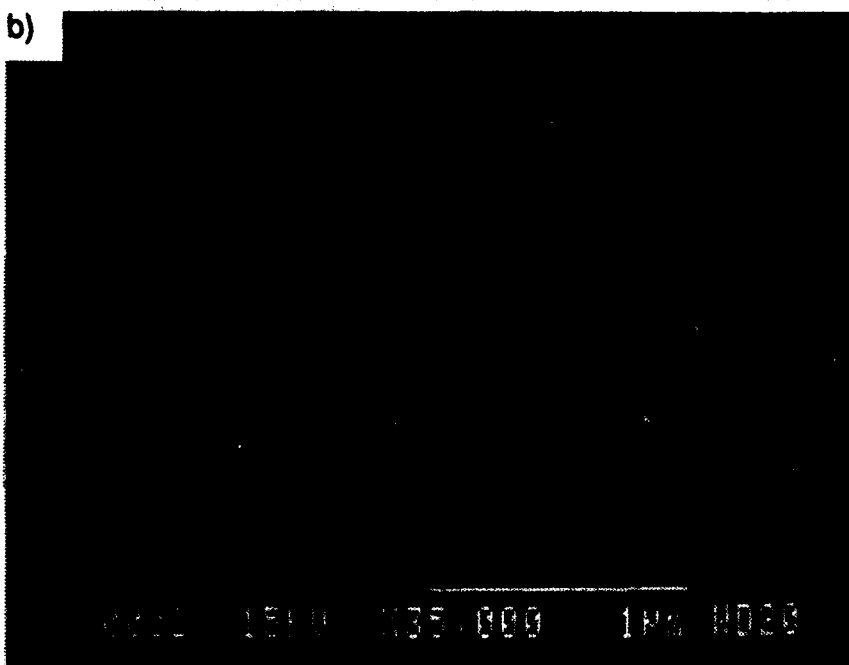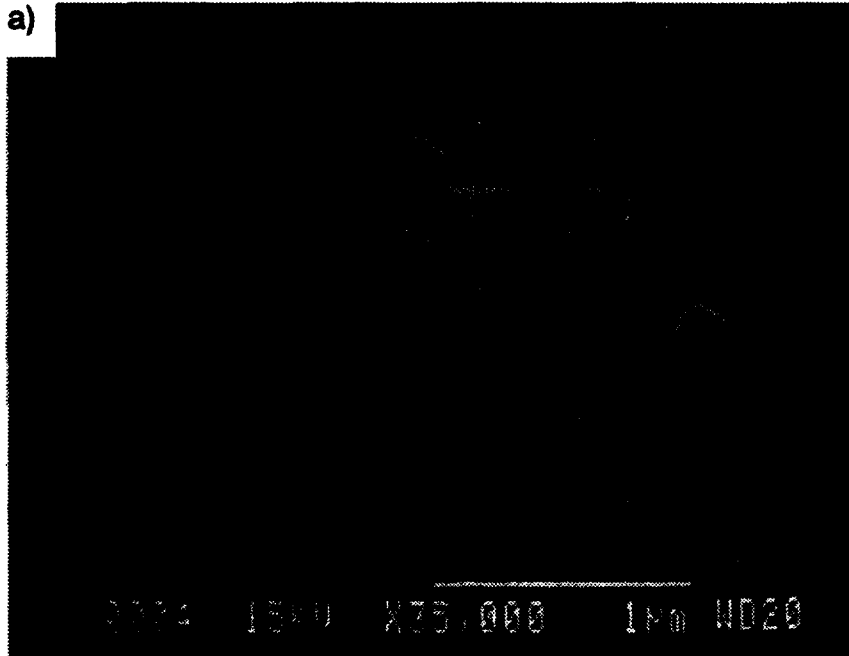
Figure 4-4. SEM micrographs of a) Mo480.C.Mo10.S.10906.1 and
b) Mo480.C.Mo40.S.10906.1 showing ~0.25μm grains.

Mg-Ta and Al-Ta alloys. These tantalum particles were attributed to poor target material.

4.1.5 X-Ray Diffraction

A summary of the x-ray diffraction (XRD) results for the Mg alloys is presented in Table 4-2. An identical summary for the Al binary alloys is given in Table 4-3. For many of these alloys, interpretation of the data was difficult because no phase diagrams exist. The results were also complicated by reaction of the alloy with the Si wafer, as well as the preferred orientation that occurs naturally in sputter deposited films.

Table 4-2. Summary of XRD Results for the Mg-Base-Group Vb and Vlb Alloys.

Film Designation	Before Heat Treatment	*	After Heat Treatment	
Mg-Mo				
Mg480.C.Mo10.S.10906.1	Si and Mg Peaks, Peak Shift	SS	Mg Peak Intensity Ratio Change, Mg_2Si	SS
Mg480.C.Mo20.S.10906.1	Si and Mg Peaks, Peak Shift	SS	Mg Peak Intensity Ratio Change, Mg_2Si	SS
Mg480.C.Mo40.S.10906.1	Si and Mg Peaks, Peak Shift	SS	Mg Peak Intensity Ratio Change, Mg_2Si	SS
Mg2/480.C.Mo10.S.11025.1	Si and Mg Peaks, Peak Shift	SS	Mg Peak Intensity Ratio Change, Mg_2Si	SS
Mg2/480.C.Mo20.S.11025.1	Si and Mg Peaks, Peak Shift	SS	Mg Peak Intensity Ratio Change, Mg_2Si	SS
Mg2/480.C.Mo40.S.11025.1	Si and Mg Peaks, Peak Shift	SS	Mg Peak Intensity Ratio Change, Mg_2Si	SS
Mg-W				
Mg480.C.W10.S.10825.1	Si and 2 Mg Peaks	SS	Mg Peak Intensity Ratio Change, Mg_2Si	SS
Mg480.C.W20.S.10825.1	Single Mg and Si Peaks	SS	Mg Peak Intensity Ratio Change, Mg_2Si	SS
Mg480.C.W40.S.10825.1	4 Si and Single Mg Peak	SS	Mg Peak Intensity Ratio Change, Mg_2Si	SS
Mg480.C.W10.S.11208.1	Mg, Si and W Peaks	P	Mg Peak Intensity Ratio Change, Mg_2Si	P
Mg480.C.W20.S.11208.1	Mg, Si and W Peaks	P	Mg Peak Intensity Ratio Change, Mg_2Si	P
Mg480.C.W40.S.11208.1	Mg, Si and W Peaks	P	Mg Peak Intensity Ratio Change, Mg_2Si	P
Mg-Cr				
Mg2/480.C.Cr10.	-	-		-
Mg2/480.C.Cr20.	-	-		-
Mg2/480.C.Cr40.	-	-		-
Mg-Ta				
Mg2/480.C.Ta10.S.11030.1	Mg, Si and Ta Peaks	P	Mg, Si, Ta and Mg_2Si Peaks	P
Mg2/480.C.Ta20.S.11030.1	Mg, Si and Ta Peaks	P	Mg, Si, Ta and Mg_2Si Peaks	P
Mg2/480.C.Ta40.S.11030.1	Mg, Si and Ta Peaks	P	Mg, Si, Ta and Mg_2Si Peaks	P
Mg2/480.C.Ta10.S.11210.1	Mg and Si Peaks	SS	Mg Peak Intensity Ratio Change, Mg_2Si	SS
Mg2/480.C.Ta20.S.11210.1	Mg and Si Peaks	SS	Mg Peak Intensity Ratio Change, Mg_2Si	SS
Mg2/480.C.Ta40.S.11210.1	Mg and Si Peaks	SS	Mg Peak Intensity Ratio Change, Mg_2Si	SS

SS - Solid Solution, P - Precipitate

Table 4-3. Summary of XRD Results for the Al-Base-Group Vb and Vlb Binary alloys.

Film Designation	Before Heat Treatment	*	After Heat Treatment	*
Al-Mo				
Al480.C.Mo10.S.10825.1	Si and Single Broad Al Peak	SS	Crystalline Al, Several New Peaks	SS
Al480.C.Mo20.S.10825.1	Si and Single Broad Al Peak	SS	Single Al Peak Narrowed, No New Peaks	SS
Al480.C.Mo40.S.10825.1	Si and Single Broad Al Peak	SS	Single Al Peak Narrowed, No New Peaks	SS
Al-W				
Al480.C.W10.S.10825.1	Si and Single Broad Al Peak	SS	Single Al Peak Narrowed, No New Peaks	SS
Al480.C.W20.S.10825.1	Si and Single Broad Al Peak	SS	Single Al Peak Narrowed, No New Peaks	SS
Al480.C.W40.S.10825.1	Si and Single Broad Al Peak	SS	Single Al Peak Narrowed, No New Peaks	SS
Al-Cr				
Al2/480.C.Cr10.S.11004.1	Al and Si Peaks, Peak Shift	SS	New Peaks, Possibly Cr$_4$Si$_4$Al$_{13}$	P
Al2/480.C.Cr20.S.11004.1	Al and Si Peaks, Peak Shift	SS	New Peaks, Possibly Cr$_4$Si$_4$Al$_{13}$	P
Al2/480.C.Cr40.S.11004.1	Al and Si Peaks, Peak Shift	SS	New Peaks, Possibly Cr$_4$Si$_4$Al$_{13}$	P
Al-Ta				
Al2/480.C.Ta10.S.11005.1	Al and Si Peaks, Peak Shift	SS	New Peaks, Possibly Al$_3$Ta	P
Al2/480.C.Ta20.S.11005.1	Al and Si Peaks, Peak Shift	SS	New Peaks, Possibly Al$_3$Ta	P
Al2/480.C.Ta40.S.11005.	Al and Si Peaks, Peak Shift	SS	New Peaks, Possibly Al$_3$Ta	P

For the first phase of this task, examination of the data was simplified to a go-no go process. If only the Si and Mg or Al peaks were found, the alloying element was in solid solution and the alloy was acceptable. If several additional peaks formed after heat treating that could not be related to either Al or Mg, precipitation was assumed to have occurred without performing detailed examination to determine the phases that had formed. An exception to this process was the Mg alloys where Mg$_2$Si formed after heat treatment. This reaction would not have occurred if the alloy was deposited onto Gr fibers and thus these peaks were identified and removed from further consideration.

Mg-Group Vb and Vlb Alloys

Mg-Cr

XRD characterization for this alloy was not conducted.

Mg-Mo

In general, the diffraction patterns for all compositions of the Mg-Mo alloys were very similar. In the as-sputtered condition, only the Si and several Mg

peaks were found, indicating a solid solution alloy. There was some evidence of peak shift due to expansion of the Mg lattice by substitutional Mo atoms. After heat treating, the Mg_2Si peaks were evident and, in some cases the relative intensity of the Mg peaks had changed. This was likely due to shifting of the Mg grain orientation by changing the residual stress state of the films during heat treatment. No precipitate peaks, such as elemental Mo, were found after heat treating which indicates the Mo was retained in solid solution.

Mg-Ta

The Mg-Ta diffraction patterns were very similar to the Mg-Mo patterns. Before heat treatment only the Si and Mg peaks were found, which indicated the Ta was in solid solution with the Mg. After heat treating, the presence of Mg_2Si indicated the Mg alloy had reacted with the Si, but no other peaks were present that would indicate that anything other than Mg was present.

Mg-W

For the one gun Mg-W alloys, only the Mg and Si peaks were present indicating the W was in solid solution. After heat treating, the only other peak detected was the Mg_2Si peak at 40°, indicating the film was a single phase. However, compositional analysis revealed that this alloy contained a large amount of Al. Therefore, new Mg-W alloy films were sputtered at a later time in the program. XRD patterns for these alloys showed the presence of W in the as-sputtered alloy. The intensity of the W peak at 39° decreased after heat treatment because it was next to a strong Mg_2Si peak. Nonetheless, Mg does not appear to retain the nonequilibrium concentrations of W investigated in this program.

Al-Cr

In the as-sputtered condition, the XRD pattern revealed only Al and Si peaks indicating that the Cr was in solid solution. The Al peaks were shifted to slightly higher angles, indicating lattice parameter contraction, which is consistent with the smaller relative size of the Cr atom. After heat treatment, several new peaks were detected that did not correspond to Al. Preliminary examination indicated the precipitated phase could be either $Al_{17}Cr_9$ or $Cr_4Si_4Al_{13}$. This phase was evident in the Al-5.2 at.% Cr, Al-9.3 at.% Cr and

Al-12.6 at. % Cr alloys. Therefore, any corrosion resistance afforded by non-equilibrium alloying of Al with Cr at these concentrations would likely be lost after consolidation of the composite.

Al-Mo

The XRD patterns for the as-sputtered Al-Mo contained broad peaks centered at 40° and ~20°, neither of which are exact reflection for Al. These broad, low intensity peaks are usually associated with a very fine grain size or an amorphous structure. The peak at 40° could be a combination of the normal Al peaks at 38.4° and 44.7°. The shift from either of these angles may be a result of the ultra fine grain size of the sputtered alloys, the lattice parameter shift as a result of W in solid solution in the Al, and lack of properly oriented planes in the highly textured film. After heat treating, several new peaks were present in the Al-4.3 at.% Mo XRD patterns indicating the formation of a precipitate. However, the diffraction patterns for the higher Mo concentration alloys looked very similar before and after heat treating, suggesting the Mo remained in solid solution with the Al. It was speculated that a further reduction in Mo concentration would also result in an unstable alloy, therefore two-gun Al-Mo alloys were not fabricated.

Al-Ta

As with the Cr alloys, precipitation of Ta intermetallic compound occurred after heat treatment. Preliminary examination of the diffraction pattern indicated the precipitated phase could be Al_3Ta and Al_2Ta. From a thermal stability perspective Al-Ta alloys do not appear attractive for enhancing corrosion resistance through solid solution alloying.

Al-W

Diffraction patterns for the Al-W were very similar to Al-Mo with the very broad peaks centered at ~20° and 40°. Again, this was difficult to explain. For the Al-12.1 at.% W and Al-19 at.% W, these XRD patterns remained effectively the same after heat treatment suggesting that the Al and W are present as a single phase structure, not necessarily a structure consisting of W in solid solution with Al. However, for the lower W concentration alloy, Al-4.1 at.% W, several new peaks were present after heat treatment that were not Al peaks indicating precipitates had formed. It was speculated that alloys with a further

decrease the solute concentration would also precipitate and these alloys were not examined.

Grazing Incident Diffraction

Grazing incident diffraction (GID) was conducted on a Mg-1.0 at.% W alloy deposited on both a Si wafer and a glass substrate during the same run. This was done to determine if the alloy composition or film texture were dependent on the type of substrate. The rationale behind using glass was that it would permit us to monitor the propagation of a pit through the film by optically monitoring the specimen during polarization and watching for pinholes.

Figures 4-5, through 4-7 show the GID patterns taken at x-ray incident angles of 1°, 2°, and 5° for the Mg-W alloy on glass and Si. The Mg peaks at 34.8° and 63.1° were the two major peaks detected. At 1°, the highest intensity peak was the Mg peak at $2\theta = 63.1°$. This indicated the Mg grains are primarily aligned with the (103) plane perpendicular to the surface. Proceeding deeper into the specimen with an x-ray incidence angle of 2°, the intensity of the 63.2° begins to decrease while the intensity of the 34.8° peaks increases. And at an incidence angle of 5°, the 34.8° peak, which corresponds to the (002) plane had the highest intensity. This data reveals that the crystallographic texturing of the Mg-W alloy changes as the film is deposited.

The area of the glass was larger than the area of the Si; therefore, peak intensity differences were a result of the number of counts detected. To determine if the texturing was different between the Mg-W on Si and Gl, the ratio of intensity between the 63.1° and the 34.8° peaks was calculated for the both Si and glass substrates. This ratio was then plotted as a function of beam incident angle (Figure 4-8). This plot shows that the ratio is the same for the Si and glass, which indicates that film texturing was independent of substrate.

34
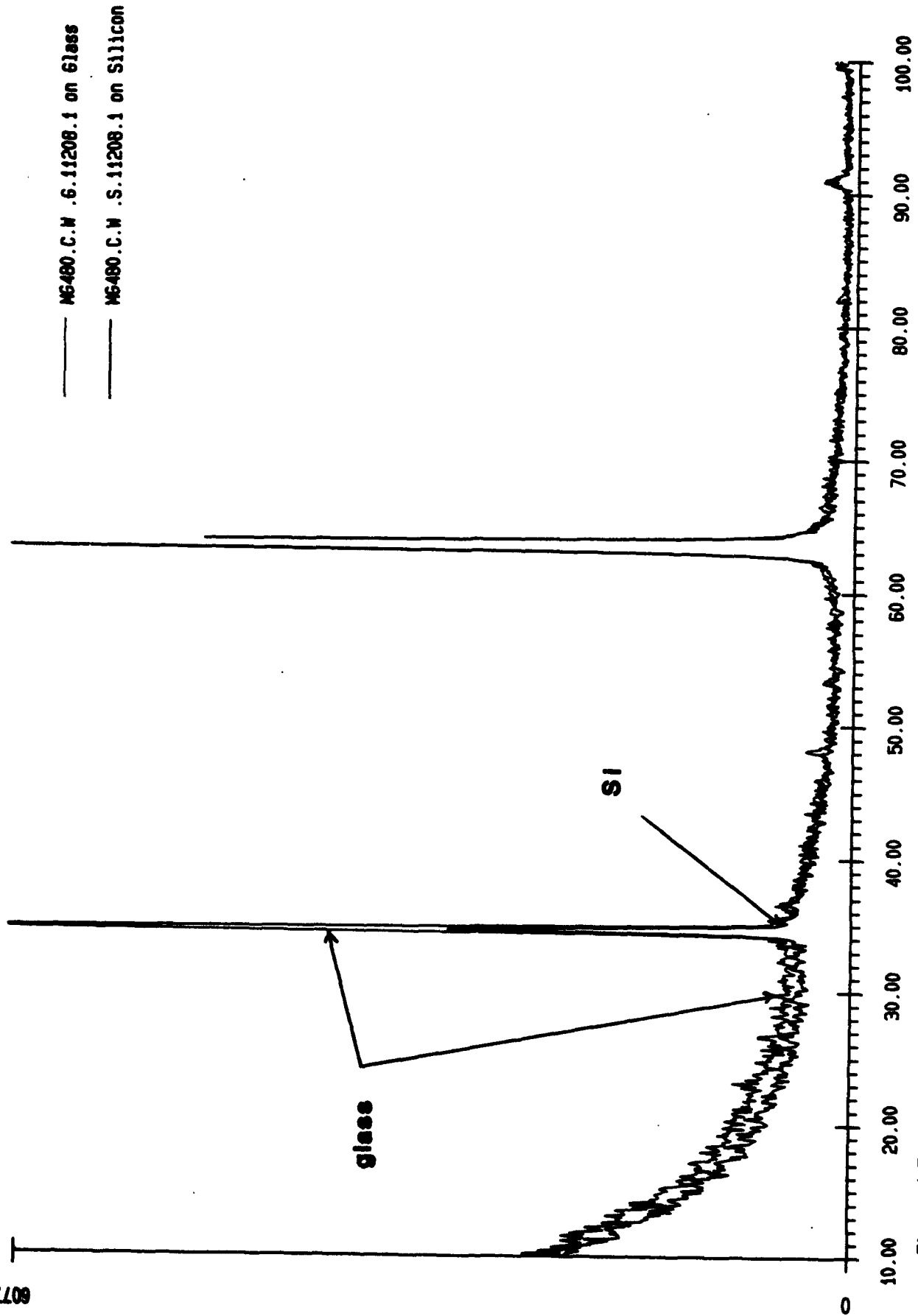
Figure 4-5. Grazing incident diffraction at 1° of Mg-N deposited on glass and silicon substrates

M6480.C.W.6.11208.1 on Glass

M6480.C.W.S.11208.1 on Silicon

SI

glass

Figure 4-6. Grazing incident diffraction at 2° of Mg-N deposited on glass and silicon substrates

M6480.C.M .G.11208.1 on Glass

M6480.C.M .S.11208.1 on Silicon

glass

Si

15122
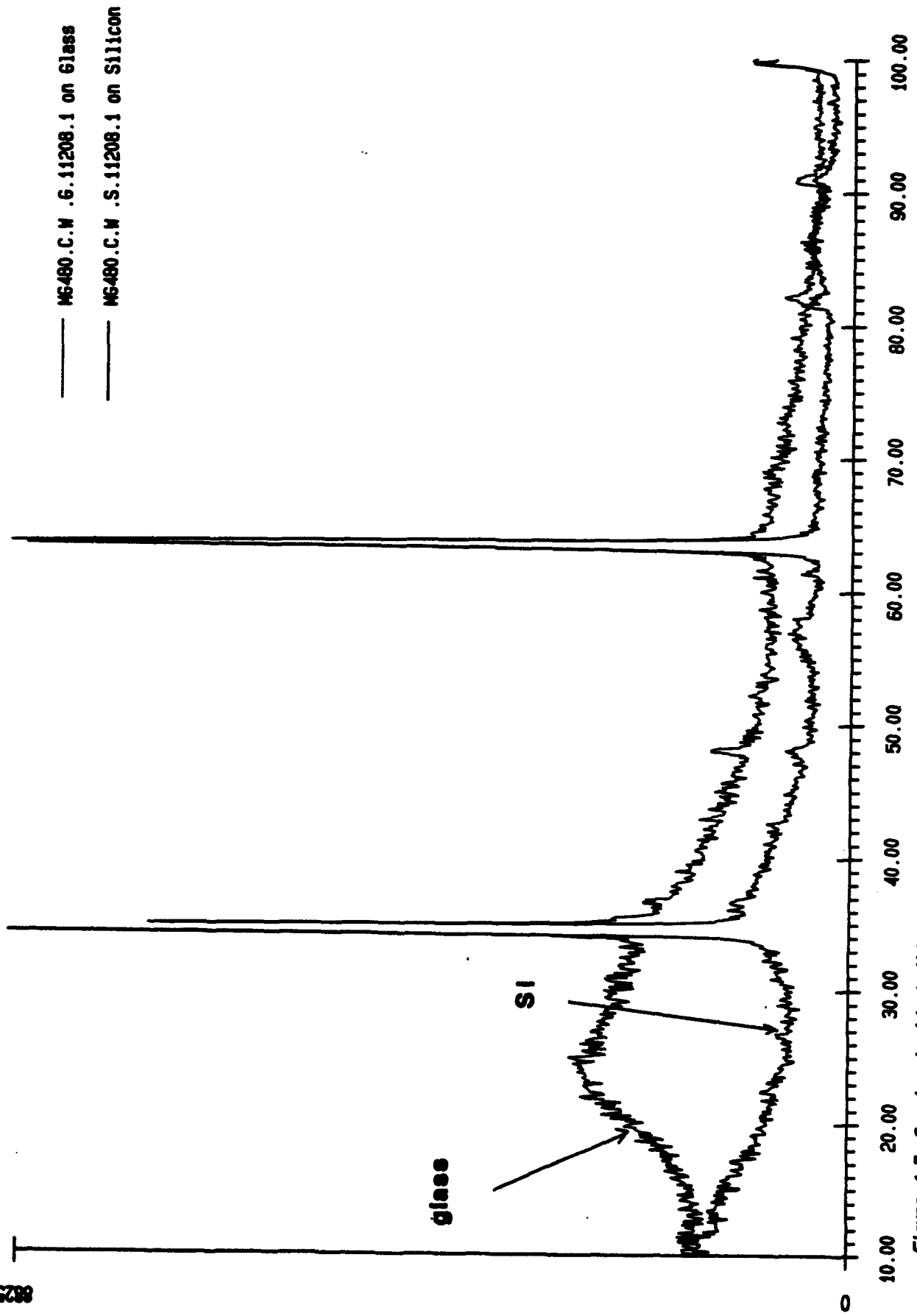
Figure 4-7. Grazing incident diffraction at 5° of Mg-M deposited on glass and silicon substrates

MG480.C.W .G.11208.1 on Glass

MG480.C.W .S.11208.1 on Silicon
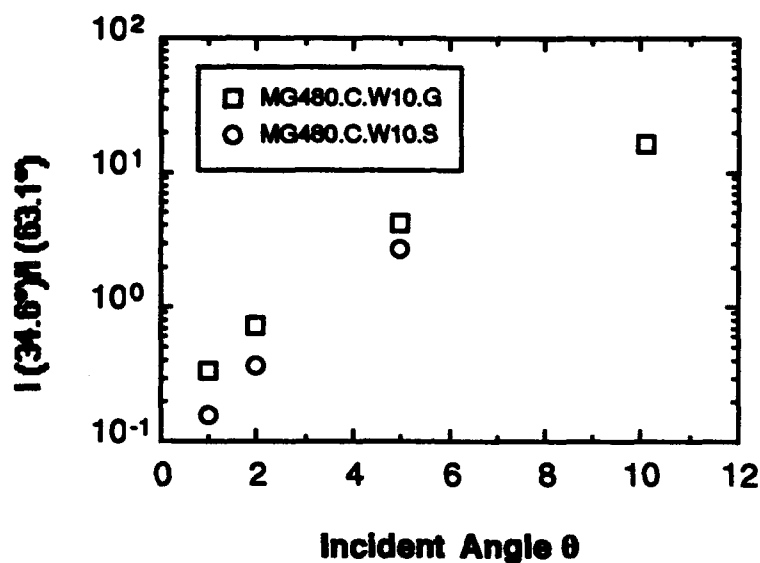
Figure 4-8. Mg peak intensity ratio for Mg-W film deposited on Gr and glass.

4.1.6 Corrosion Performance

Mg Alloys

The addition of transition metals to Mg had a significant effect on its corrosion behavior. The primary consequence of these additions was a several hundred millivolt positive shift in E_{corr}. Figures 4-9 through 4-11 show the anodic polarization behavior in 0.1M NaCl for the lowest through the highest solute concentration alloys. In this solution, pure sputtered Mg exhibits a small quasi-passive region at potentials negative to -1575 mV which was not observed for the the Mg-Cr, Mg-Mo, or Mg-W alloys. However, a quasi-passive region was noted for the low and intermediate concentration Mg-Ta alloys extending to potentials of approximately -1350 mV.
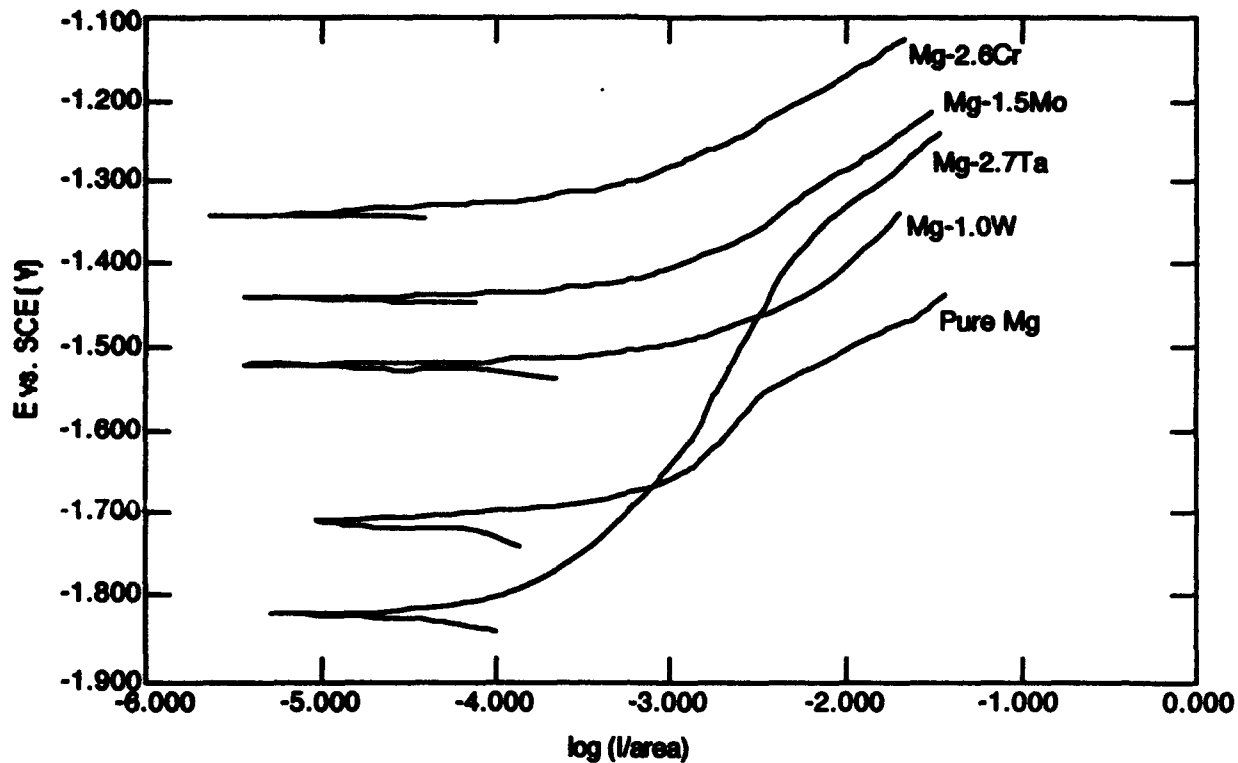
Figure 4-9. Anodic polarization behavior for lowest concentration Mg alloys.
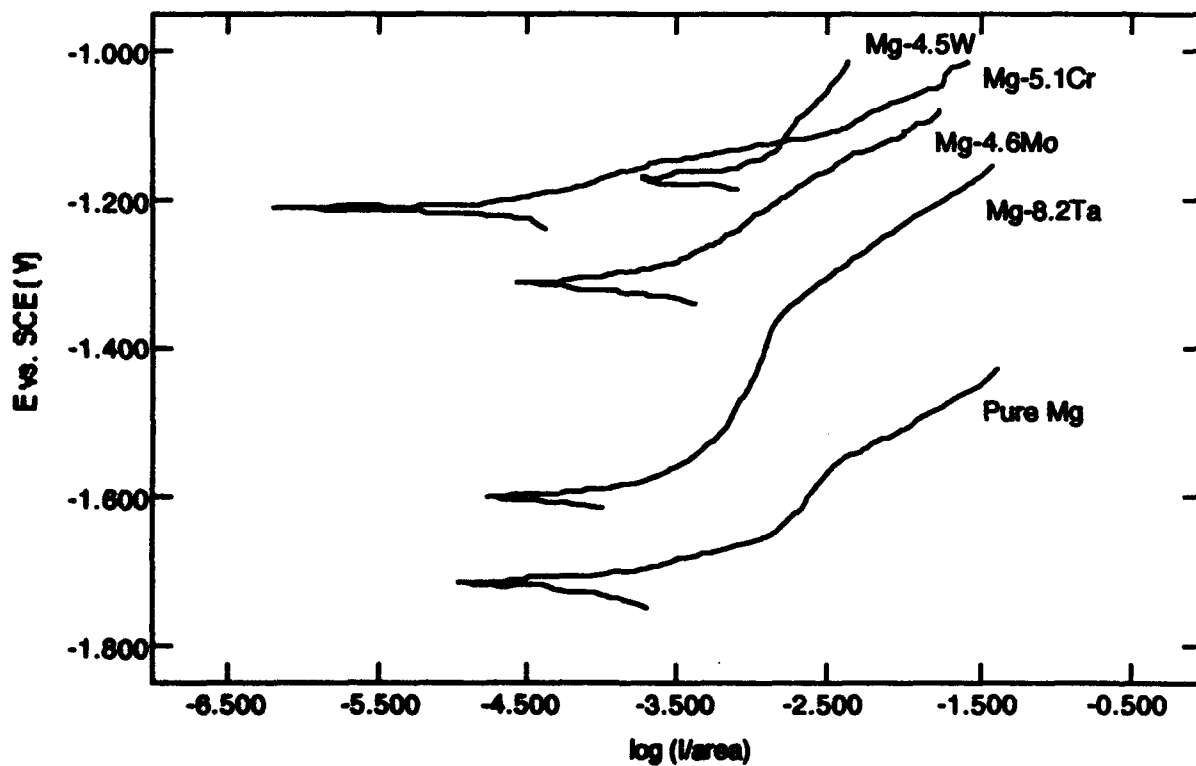
Figure 4-10. Anodic polarization behavior for medium concentration Mg alloys.

39
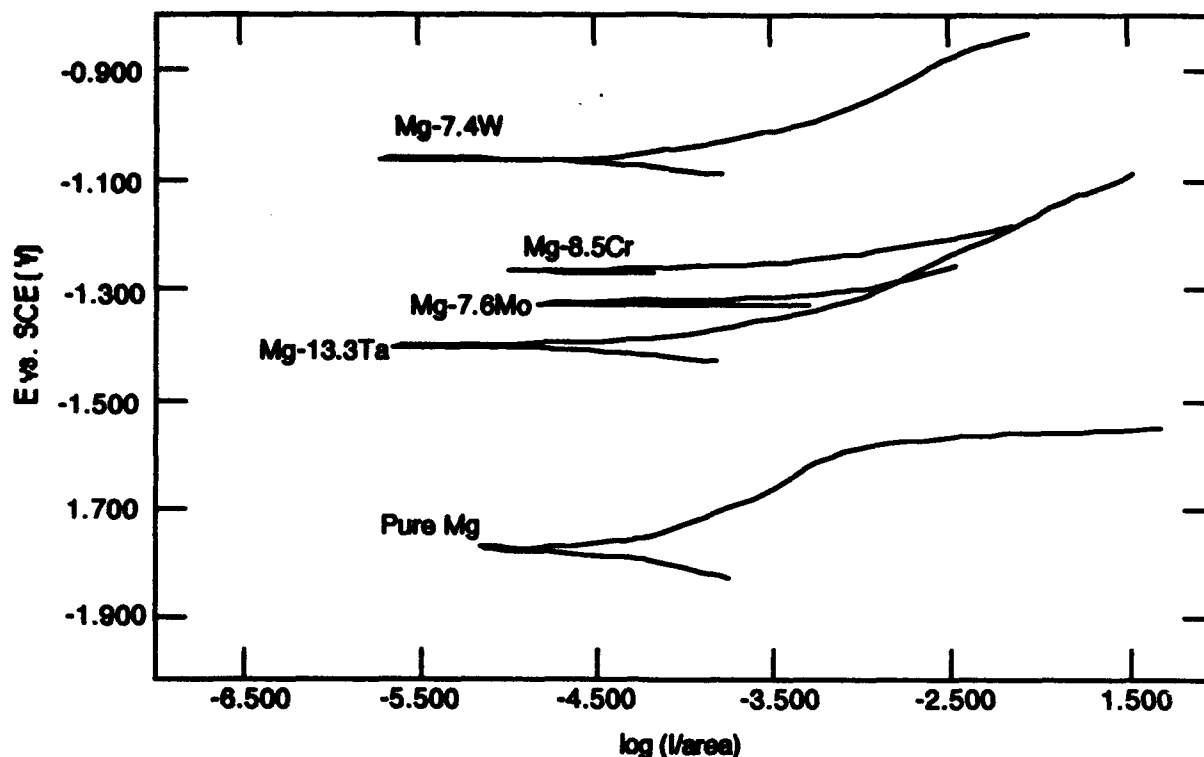
Figure 4-11. Anodic polarization behavior for highest concentration Mg alloys.

The quasi-passive nature of the Mg-2.7%Ta alloy is more clearly shown in Figure 4-12 which was generated at a scan rate of 0.2 mV/s. As was mentioned earlier, the rapid corrosion of the Mg and Mg alloys made it necessary to conduct the experiments on these alloys at scan rate faster than the ASTM standard rate for generating a slow potentiodynamic curve of 0.2 mV/sec. The increase in scan rate was believed to have had little effect on the general shape of the polarization curve for the active alloys, but the higher scan rate did have a significant effect on the shape of the curve for the alloys exhibiting passivation tendencies. At the lower scan rates, the passive region was more clearly defined with a passive current density that was independent of potential and a distinct E_p. Figure 4-13 compares the polarization curves for the Mg-Ta alloys generated at a scan rate of 0.2mV/s. Increasing the Ta concentration increased both E_{corr} and E_p, and at the highest solute concentration no evidence of passivity was observed--most likely as a result of the high value for E_{corr}.

A comparison of Figures 4-9 through 4-11 reveals that at the lower solute concentrations Cr had the greatest effect on E_{corr} (increasing it by ~ 380 mV);
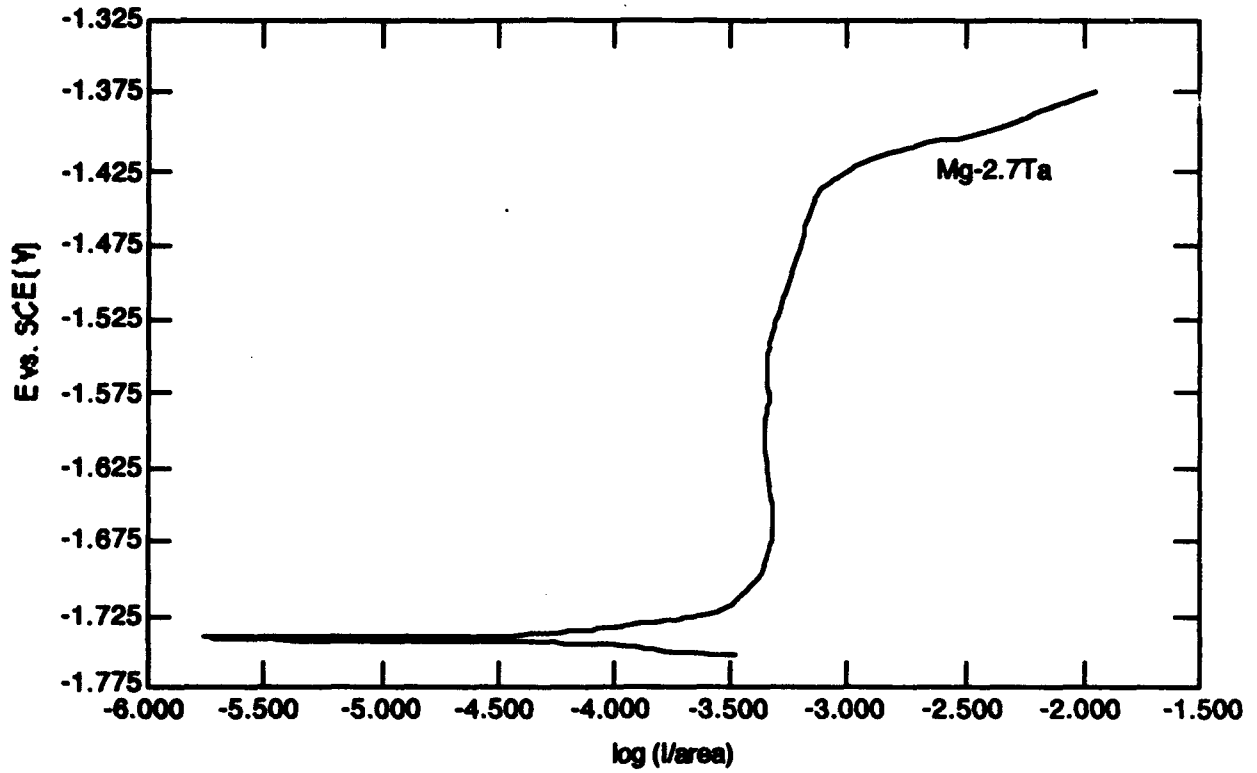
Figure 4-12. *Anodic polarization curve depicting the quasi-passive nature of the Mg-2.7%Ta alloy.*
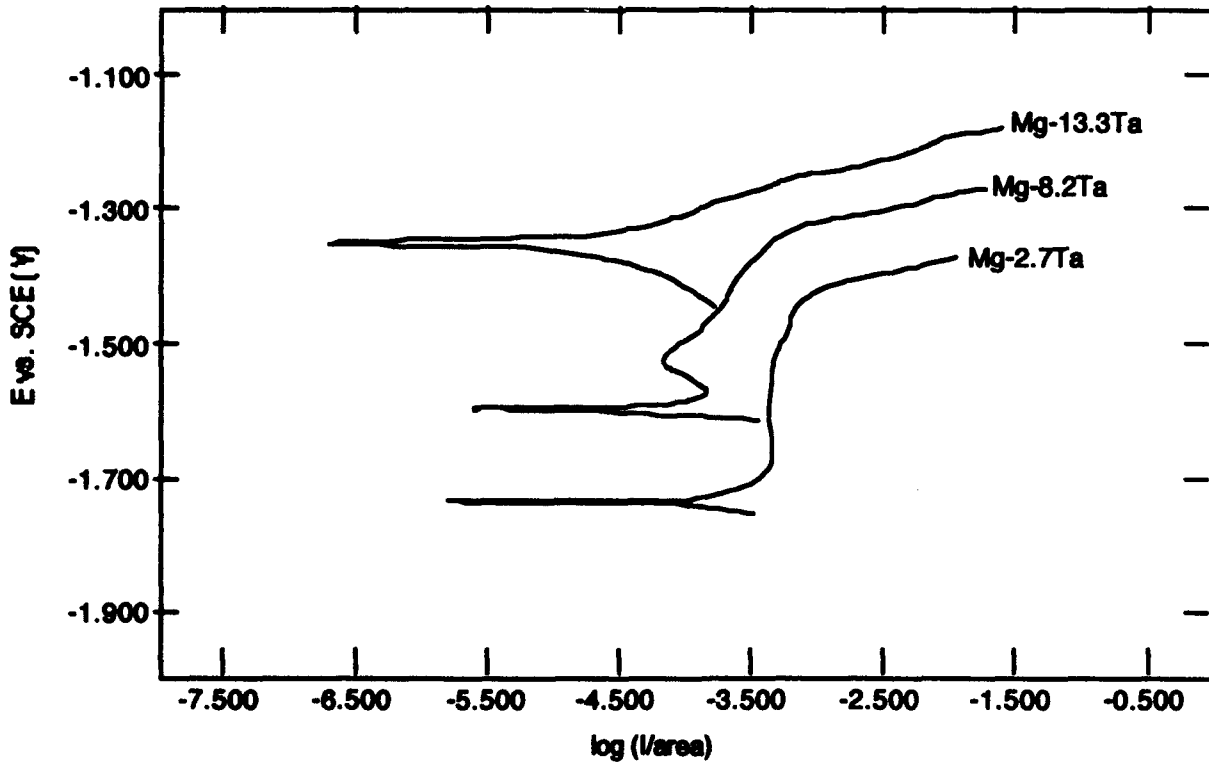
Figure 4-13. *A comparison of Mg-Ta alloys with different Ta concentrations.*

whereas, at higher solute concentrations W had the greatest effect (increasing it by ~ 700 mV). While the lack of extensive regions of active dissolution made it difficult to identify accurate Tafel slopes for each of the alloys, the data do suggest similar dissolution rates for the Cr, Mo, and W alloys. Exposure of the Mg and the Mg-Cr alloys to artificial seawater resulted in behavior almost identical to that observed in the 0.1M NaCl, as illustrated in Figure 4-14. Figure 4-15 shows the anodic polarization behavior for two very high Cr concentration alloys in artificial seawater. The 60% Cr alloy exhibited an E_{corr} of -750 mV and a narrow active-passive transition; whereas, the 90 % Cr alloy exhibited an E_{corr} of -350 mV and passivated spontaneously. While the very high solute concentration for these alloys would prohibit their use in weight critical applications, it is interesting to note the extent to which the electrochemical behavior of Mg can be altered with the addition of Cr.

Since the goal of this research is to develop nonequilibrium alloys for use in graphite reinforced composites, the galvanic corrosion performance of the alloys coupled to graphite is of great interest. Figures 4-16 through 4-19 show the galvanic diagrams [Ref. 23] for the highest solute concentration of each of the alloys coupled to P75 graphite. These diagrams are based on areas of 1 cm^2 and the polarization behavior for Al is also included in each diagram for comparison. For each of the alloys, the anodic polarization curve intersects the cathodic curve in the limiting current density region at a current of approximately 520 μA. In the case of pure Mg, the very negative E_{corr} for this metal results in cross-over of the anodic and cathodic curves in the hydrogen evolution region of the cathodic curve. Galvanic corrosion of the Mg in this instance is driven by hydrogen evolution on the graphite and results in corrosion rates an order of magnitude higher than that predicted for the Mg alloy/Gr couples. The high E_{corr} values for the Mg-Cr and Mg-W alloys lead to cross-over of the anodic and cathodic curves well within the limiting current region of the cathodic reaction; whereas, the Mg-Mo and Mg-Ta alloys cross-over at a point closer to where hydrogen evolution becomes the predominate cathodic reaction. This point could be of importance if the local conditions existing in the composite were to lead to a reduction in the overvoltage needed for hydrogen evolution.

The most promising Mg alloys from a corrosion standpoint were the Mg-Cr and the Mg-W because of their high E_{corr} values, and the low solute Mg-Ta
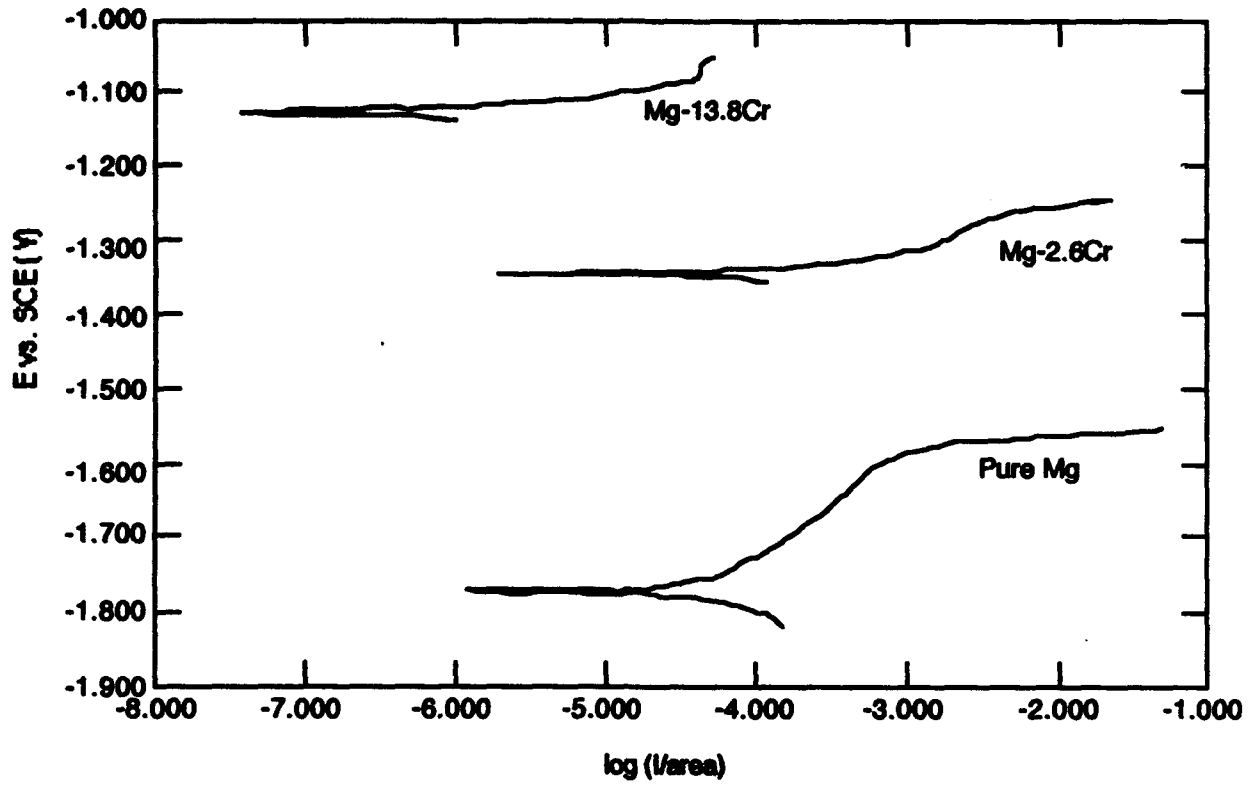
Figure 4-14. Mg and Mg-Cr alloys tested in artificial seawater.
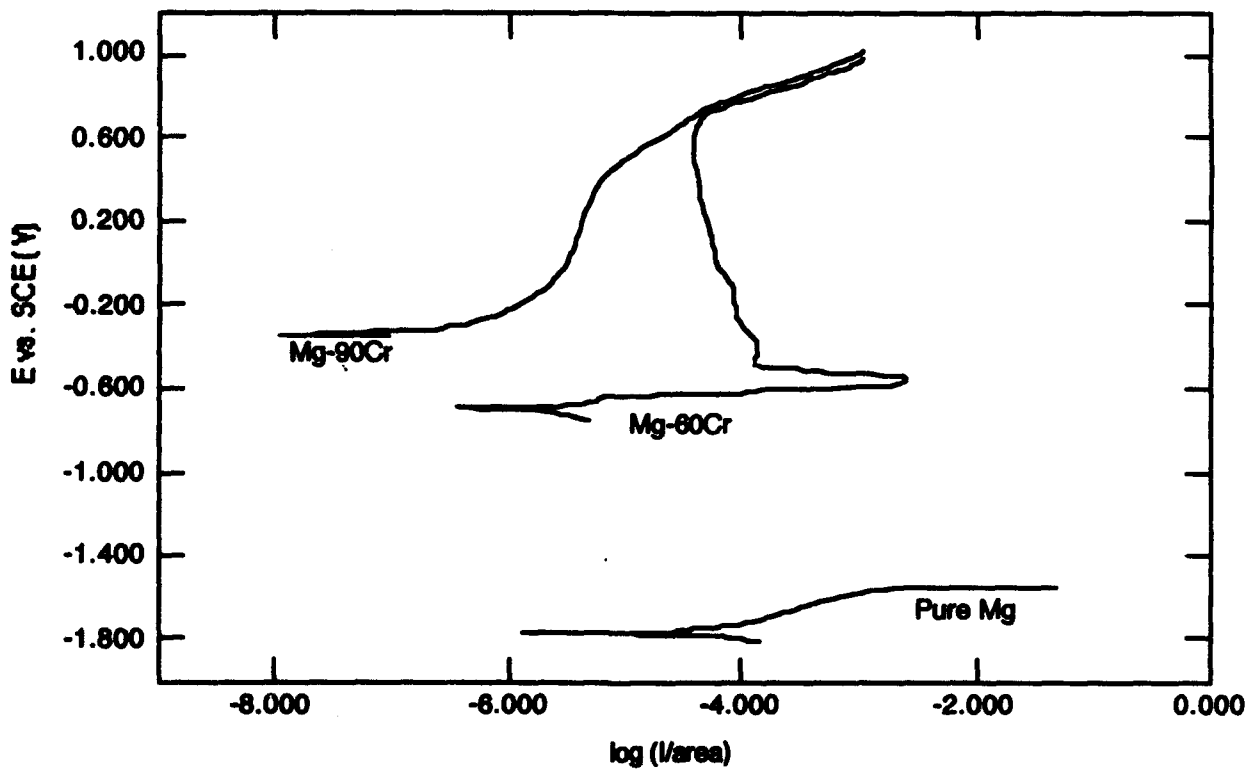
Figure 4-15. Anodic polarization behavior for 2 very high Cr concentration alloys in seawater.

43
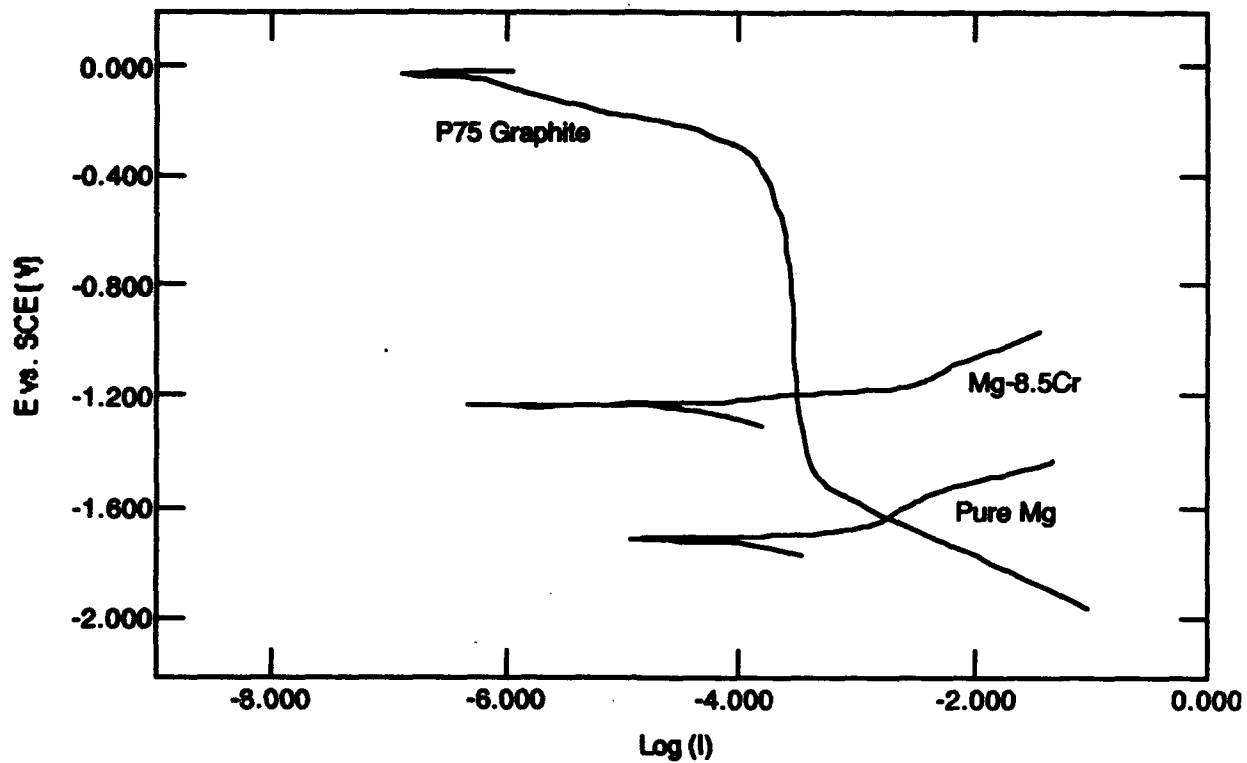
Figure 4-16. *Galvanic diagrams for pure Mg and Mg-8.5Cr coupled to P75 graphite.*
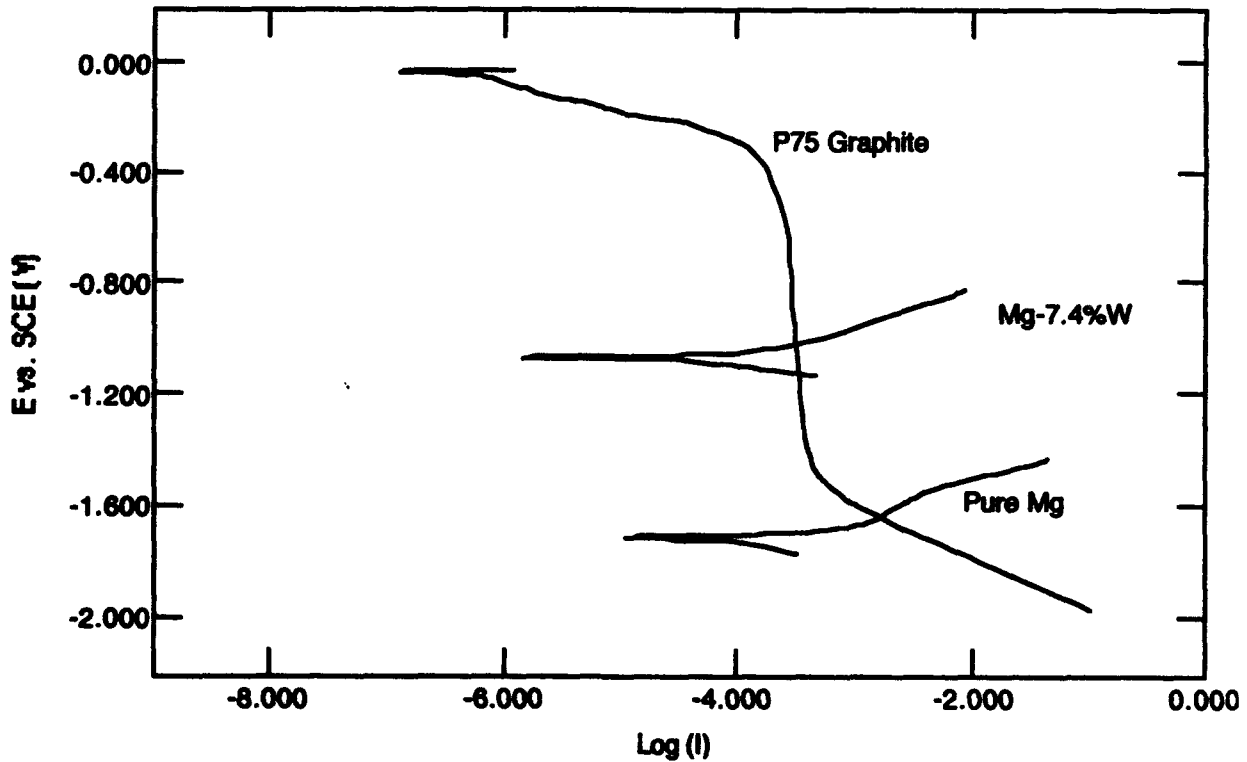
Figure 4-17. *Galvanic diagrams for pure Mg and Mg-7.4W coupled to P75 graphite.*

44
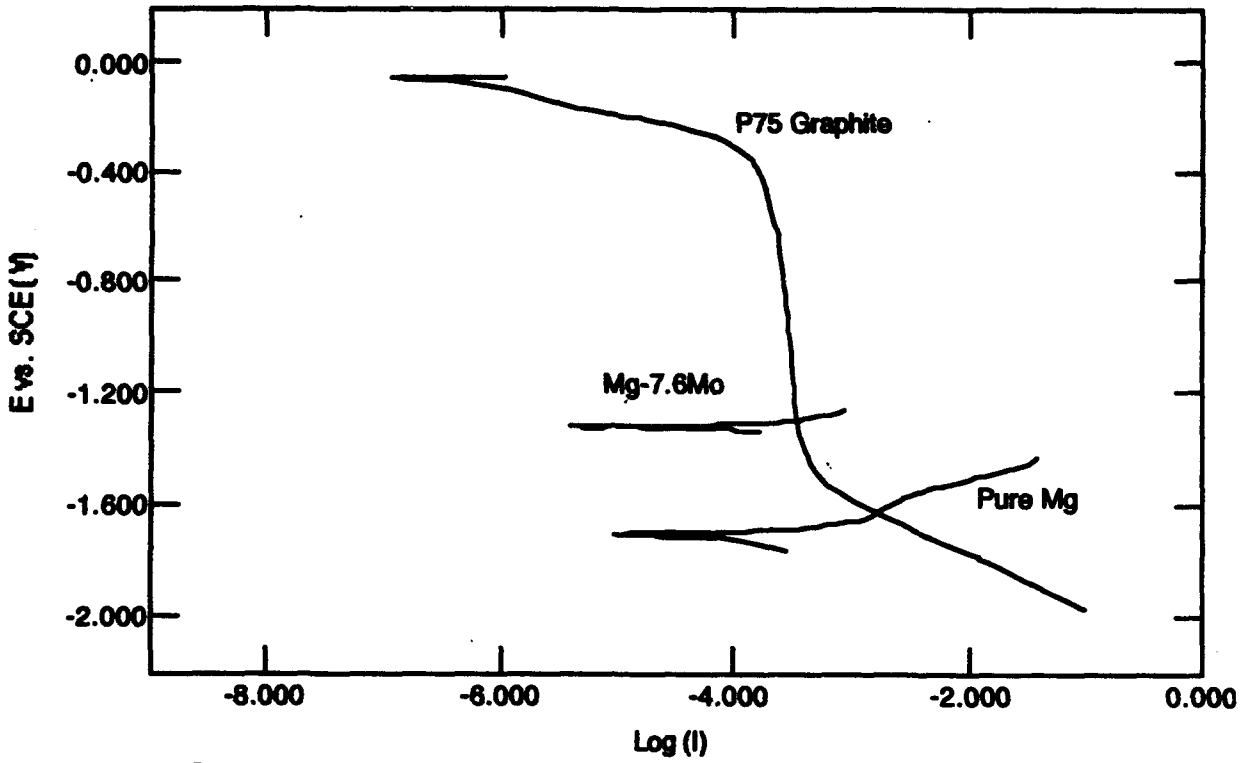
Figure 4-18. Galvanic diagrams for pure Mg and Mg-7.6Mo coupled to P75 graphite.
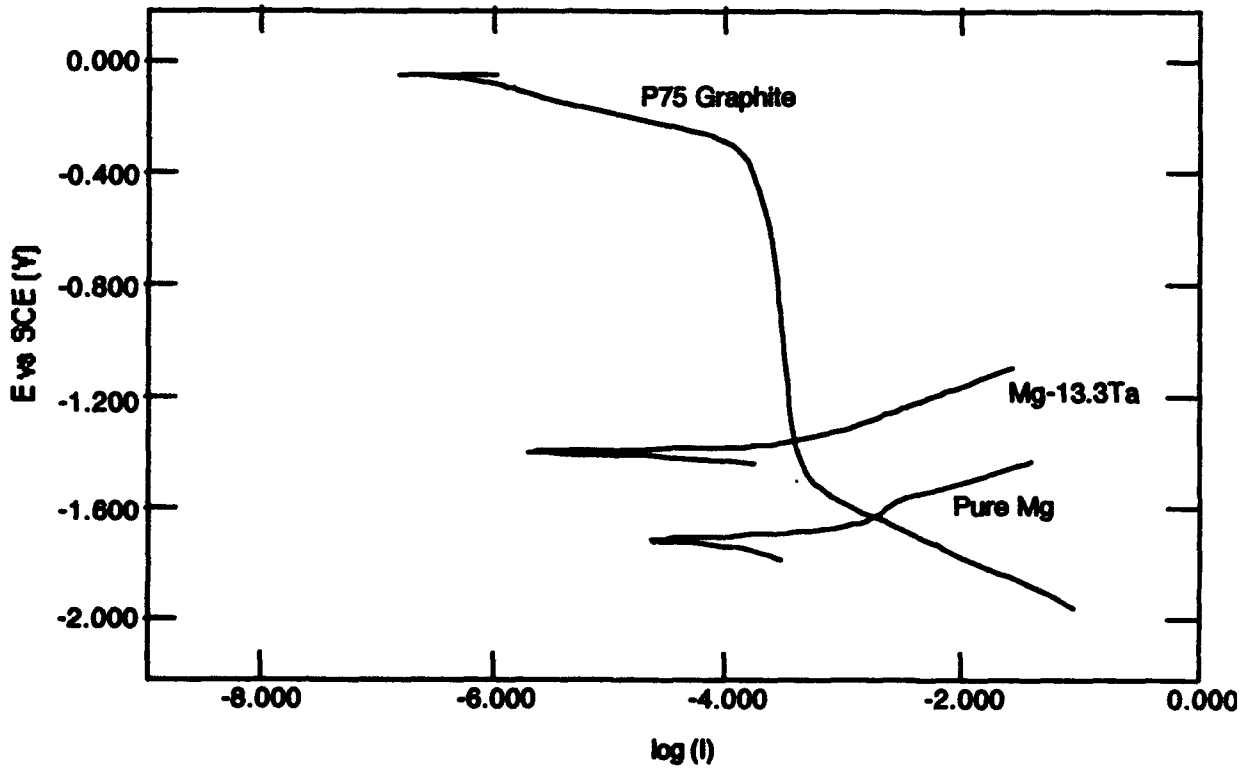
Figure 4-19. Galvanic diagrams for pure Mg and Mg-13.3Ta coupled to P75 graphite.

45

alloys because they exhibited passivity. In addition to corrosion resistance, thermal stability will be of critical importance to the alloy chosen for the composite and both of these issues were considered in the down selection of alloys for phase 2.

Al Alloys

Table 4-4 summarizes the results of the anodic polarization experiments conducted on the nonequilibrium Al alloys. A comparison of representative curves for each of the low solute concentration alloys is presented in Figure 4-20. The Al-W alloy exhibited the largest passive region extending from -760 to +460 mV. The next largest passive region, and the one with the lowest i_p, was observed for the Al -Mo alloy. Similar pitting potentials of approximately -200 mV were observed for both the Al-2.8%Ta and the Al-2.4%Cr alloys. Figure 4-21 shows that at the highest solute concentrations E_p for the Al-Cr is only shifted slightly in the positive direction to -140 mV, whereas, E_p for the Al-25.6 %W and the Al-25.9%Mo alloys are shifted to +800 mV and + 625 mV, respectively. It is interesting to note that passivity is also maintained for these alloys at pH values in excess of 8. Figures 4-22 through 4-25 show the anodic polarization behavior for the highest solute concentration alloys in a 0.1M chloride solution with the pH adjusted to 10 (with NaOH). In each case, the passive film appears to be slightly less protective at the higher pH--probably resulting from an increase in dissolution of the alloy through the passive film. Similar E_p values were noted at pH 8 and 10 for the Al-W, Al-Mo, and Al-Cr alloys; whereas, a slightly higher E_p was noted for the Al-Ta alloys at pH 8. The polarization behavior at pH values outside the neutral range is of importance since the localized pH could shift out the neutral range with time.

Galvanic diagrams for the aluminum alloys coupled to P75 graphite are presented in figures 4-26 through 4-29. Again, these diagrams are based on an area ratio of 1:1 and for comparison purposes, an anodic polarization curve for pure sputtered Al is also shown. In the case of pure aluminum coupled to P75 graphite, the cathodic current limited, oxygen reduction curve crosses the anodic curve in the region were pitting is observed and, as a result, relatively high corrosion rates would be expected for the aluminum as a

Table 4-4. Summary of results of the anodic polarization experiments conducted on the nonequilibrium Al alloys.

SAMPLE	SCAN (mV/s)	Ecorr (mV-SCE)	Eb (mV-SCE)	Ipass (μA/cm)
Al	0.2	-1070	-720	0.18
Al	0.2	-980	-700	0.05
Al - 4.30 Mo	0.2	-520	100	- - -
Al - 4.30 Mo	0.2	-540	100	- - -
Al - 4.30 Mo	0.2	-550	155	0.63
Al - 12.3 Mo	1	-550	525	6.50**
Al - 25.9 Mo	0.2	-440	750	3.00
Al - 25.9 Mo	0.2	-427	700	0.60
Al - 25.9 Mo	0.2	-460	600	0.80
Al - 25.9 Mo *	0.2	-495	770	1.90
Al - 25.9 Mo *	0.2	-540	760	4.17
Al - 4.1 W	0.2	-760	460	5.01**
Al - 4.1 W	0.2	-730	450	0.60
Al - 12.1 W	1	-710	700	6.50**
Al - 25.6 W	0.2	-625	- - -	1.74
Al - 25.6 W	0.2	-615	800	0.63
Al - 25.6 W *	0.2	-655	840	1.58
Al - 25.6 W *	0.2	-645	850	1.80
Al - 2.8 Ta	0.2	-890	-200	3.89**
Al - 2.8 Ta	0.2	-1106	-200	2.06**
Al - 8.2 Ta	1	-1180	-90	6.69**
Al - 13.4 Ta	0.2	-905	280	4.37**
Al - 13.4 Ta	0.2	-905	10	5.32**
Al - 13.4 Ta *	0.2	-1040	125	1.78
Al - 2.4 Cr	0.2	-940	-180	10.37**
Al - 2.4 Cr	0.2	-981	-200	67.11**
Al - 11.6 Cr	0.2	-890	-140	2.69**
Al - 11.6 Cr	0.2	-865	-100	0.18**
Al - 11.6 Cr *	0.2	-920	-5	0.79
Al - 11.6 Cr *	0.2	-940	-5	4.64**
(0.1MNaCl, pH 8, AS IS)	* = pH 10			
	** = AVG			

47
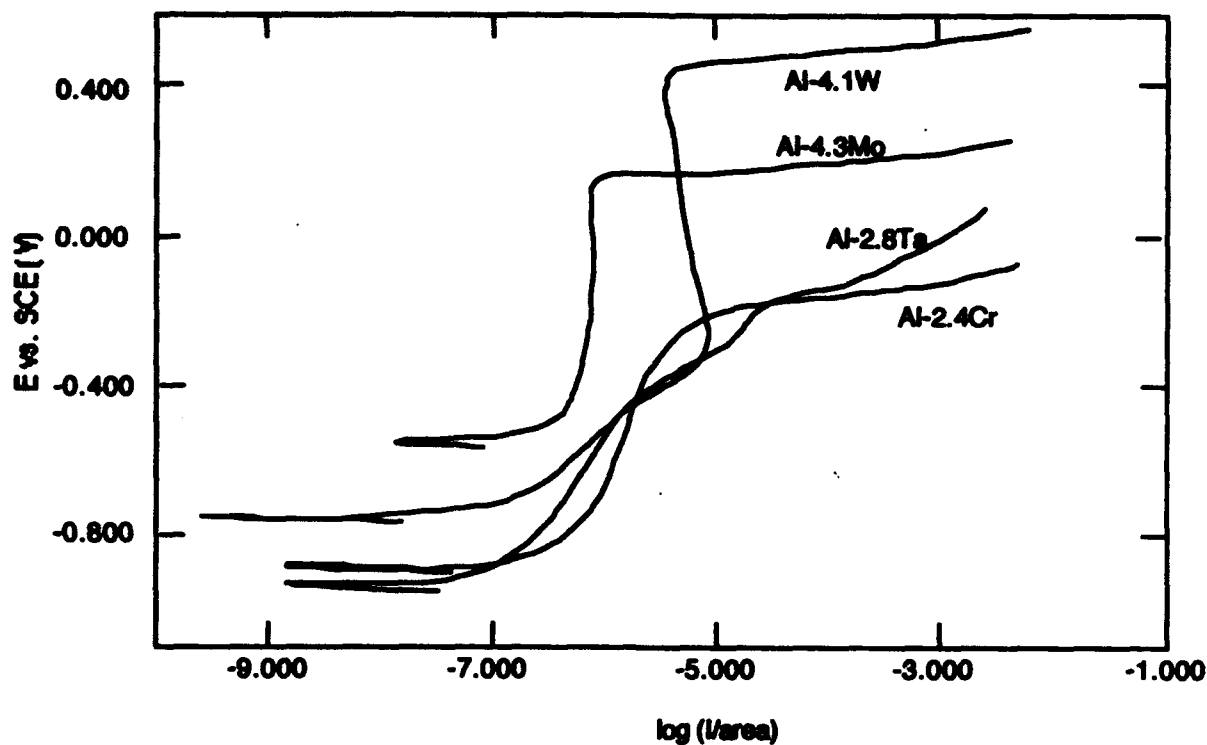
Figure 4-20. Comparison of anodic polarization curves for the low solute concentration Al alloys.
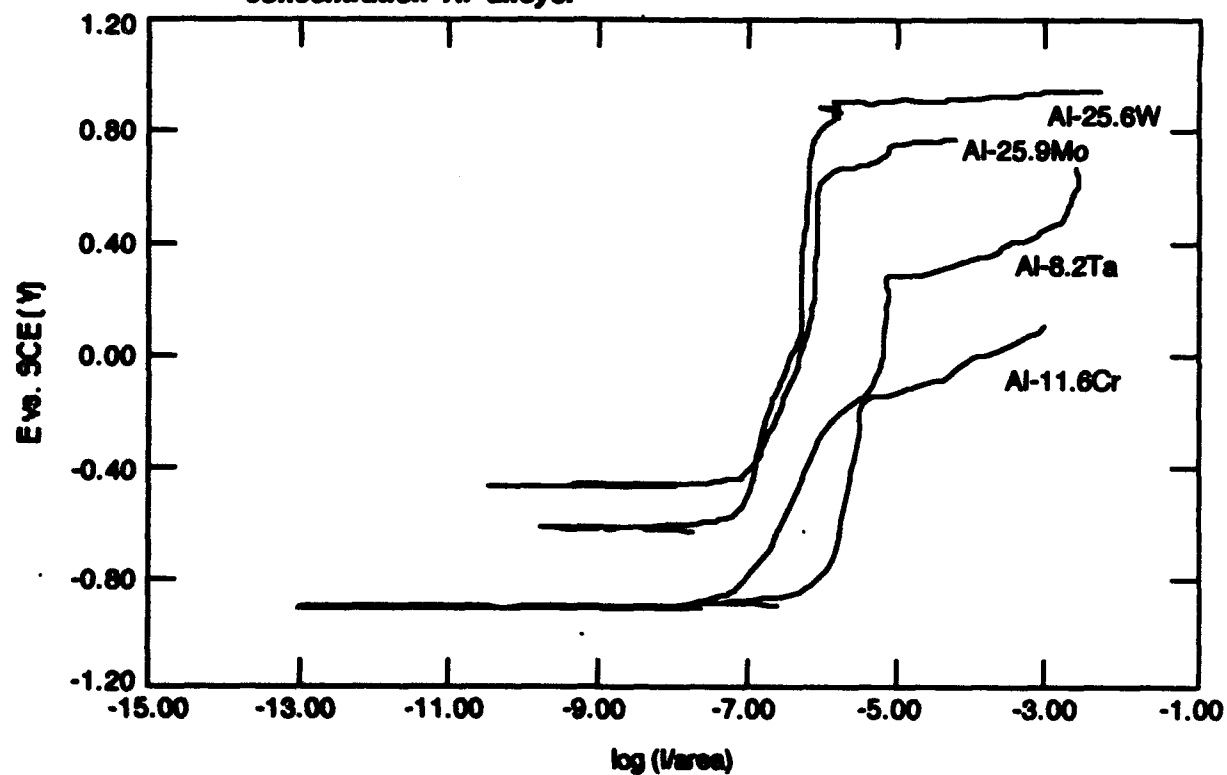
Figure 4-21. Comparison of anodic polarization diagrams for the highest solute concentration Al alloys.

48
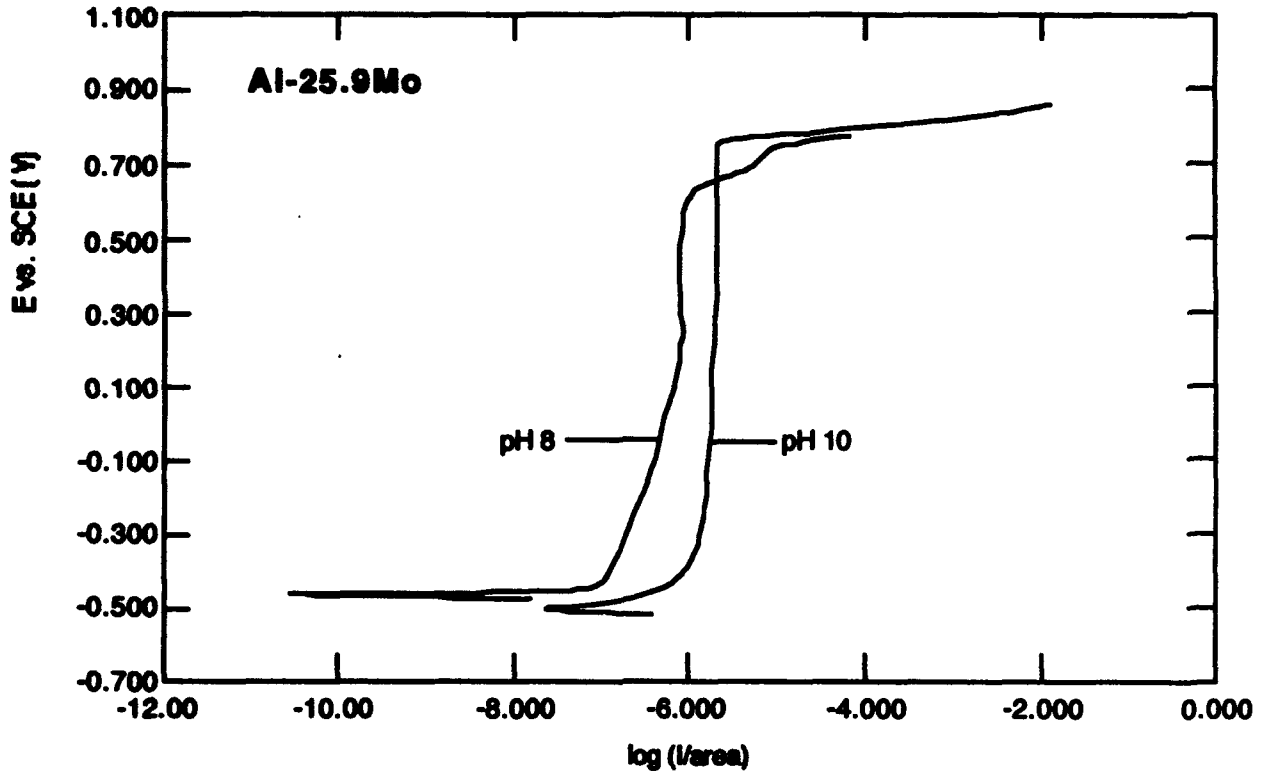
Figure 4-22. Anodic polarization diagrams for Al-25.9Mo at pH's of 8 and 10.
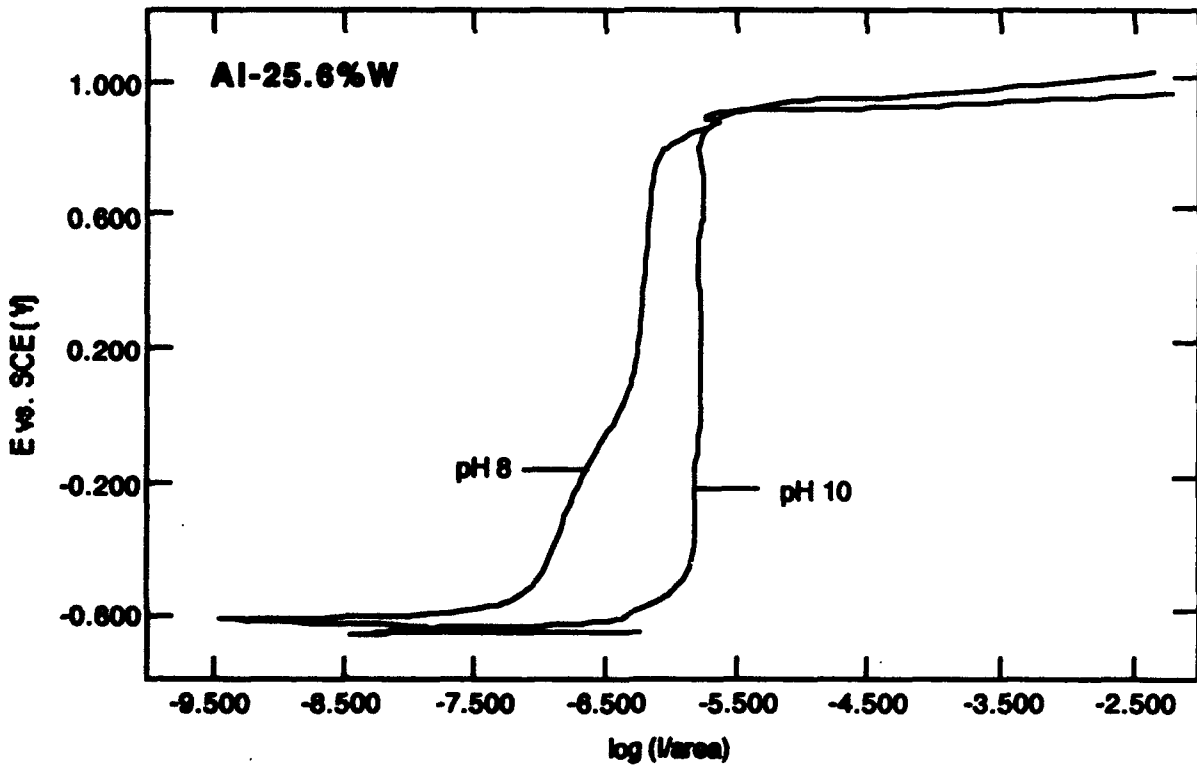
Figure 4-23. Anodic polarization curves for Al-25.6W at pH's of 8 and 10.

49
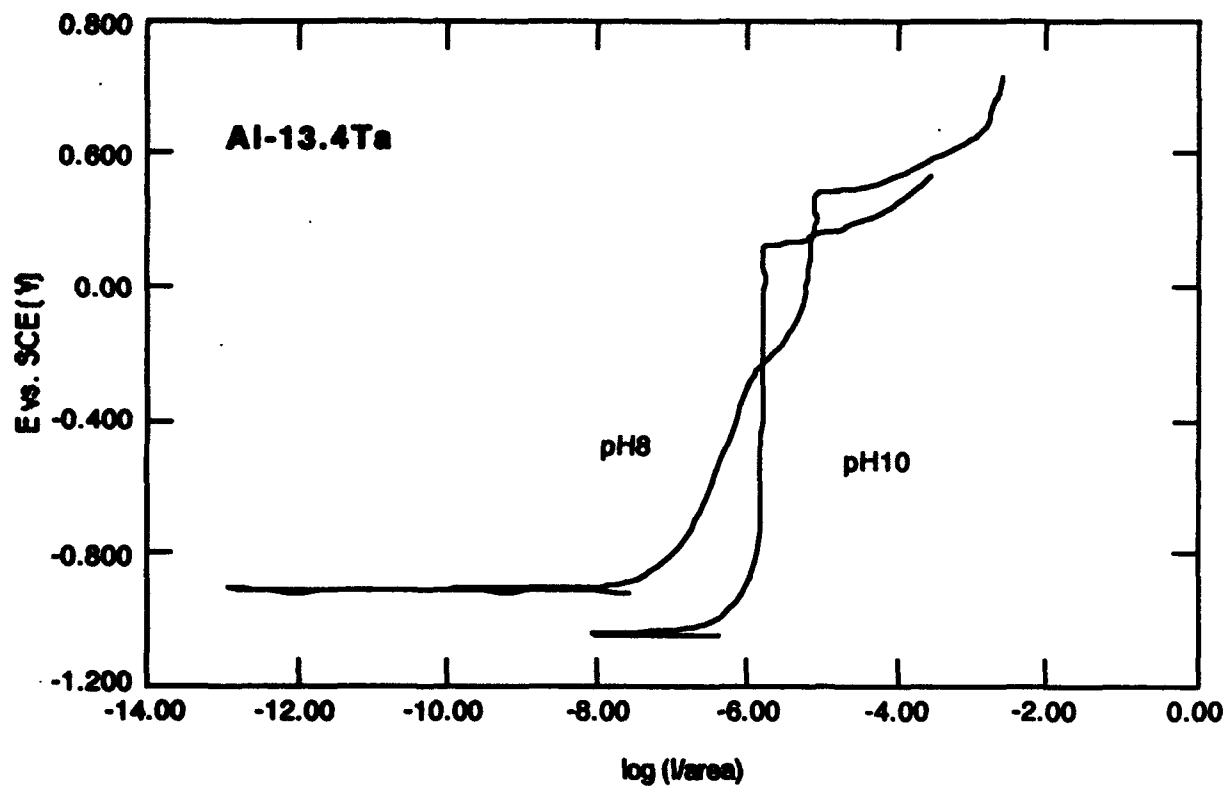
Figure 4-24. Anodic polarization curves for Al-13.4Ta at pH's of 8 and 10.
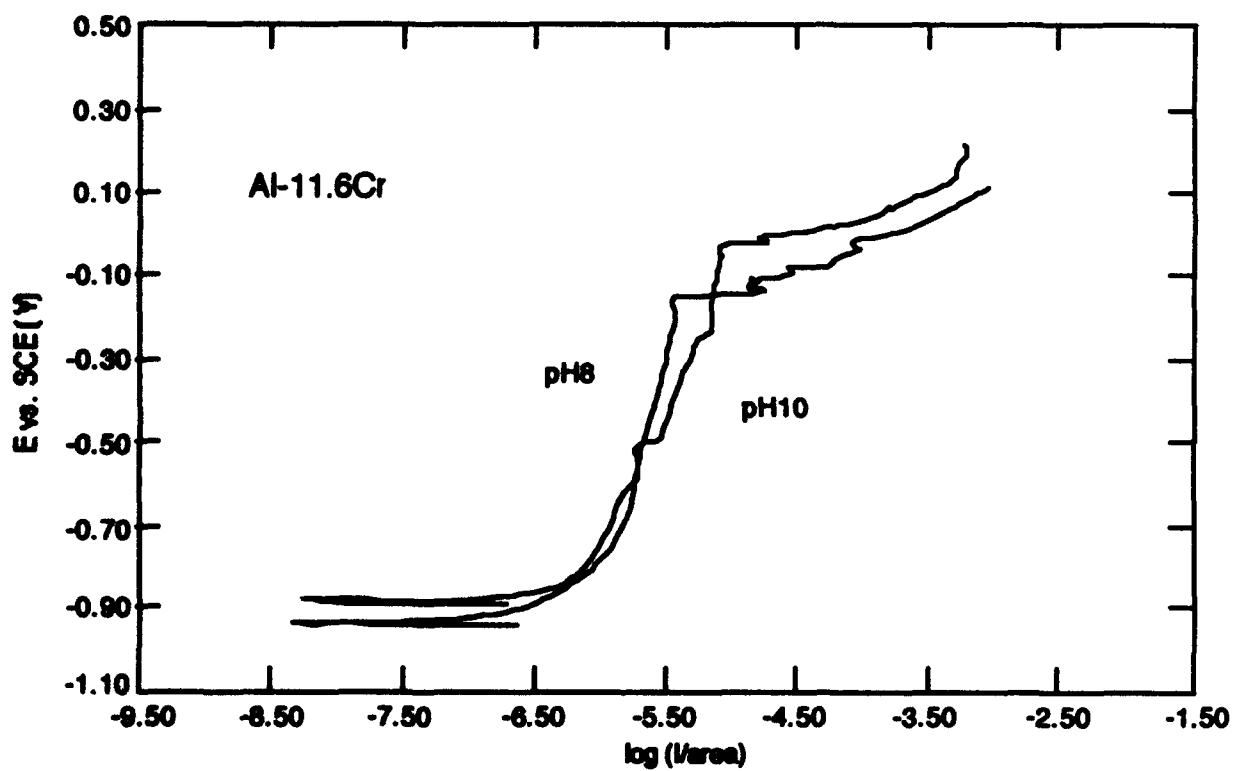
Figure 4-25. Anodic polarization curves forAl-11.6Cr at pH's of 8 and 10.

50
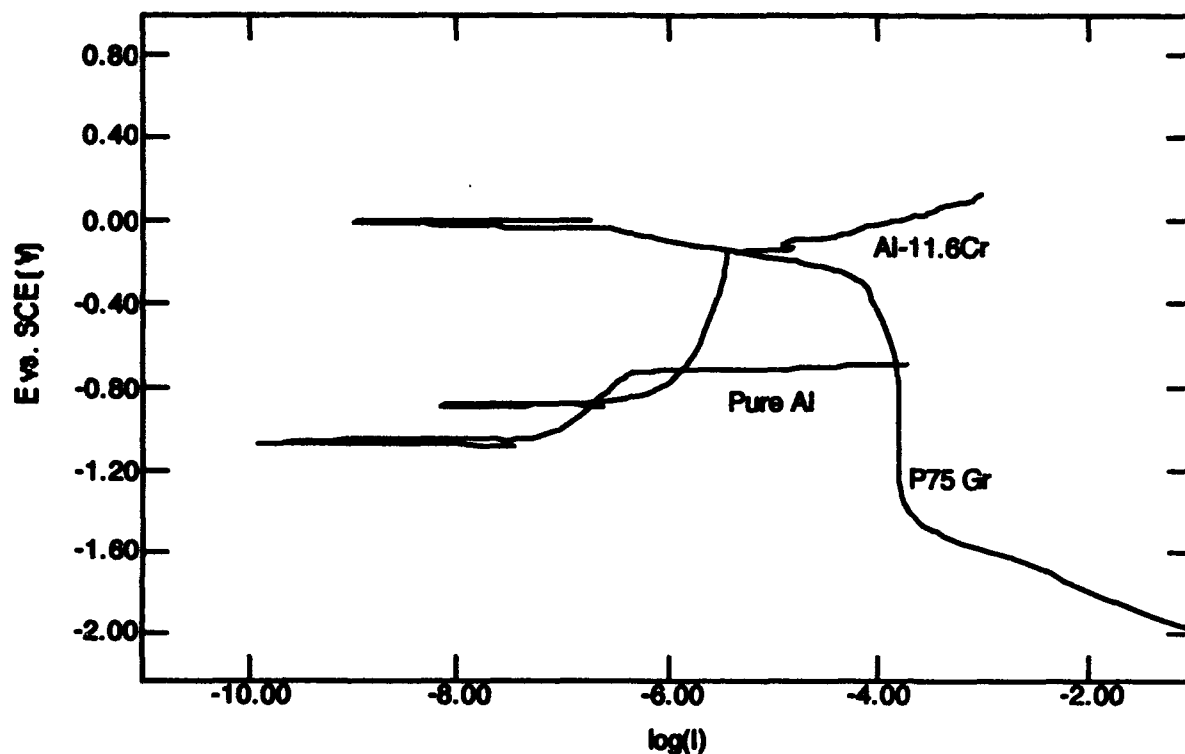
Figure 4-26. Galvanic diagrams for pure Al and Al-11.6Cr coupled with P75 graphite.
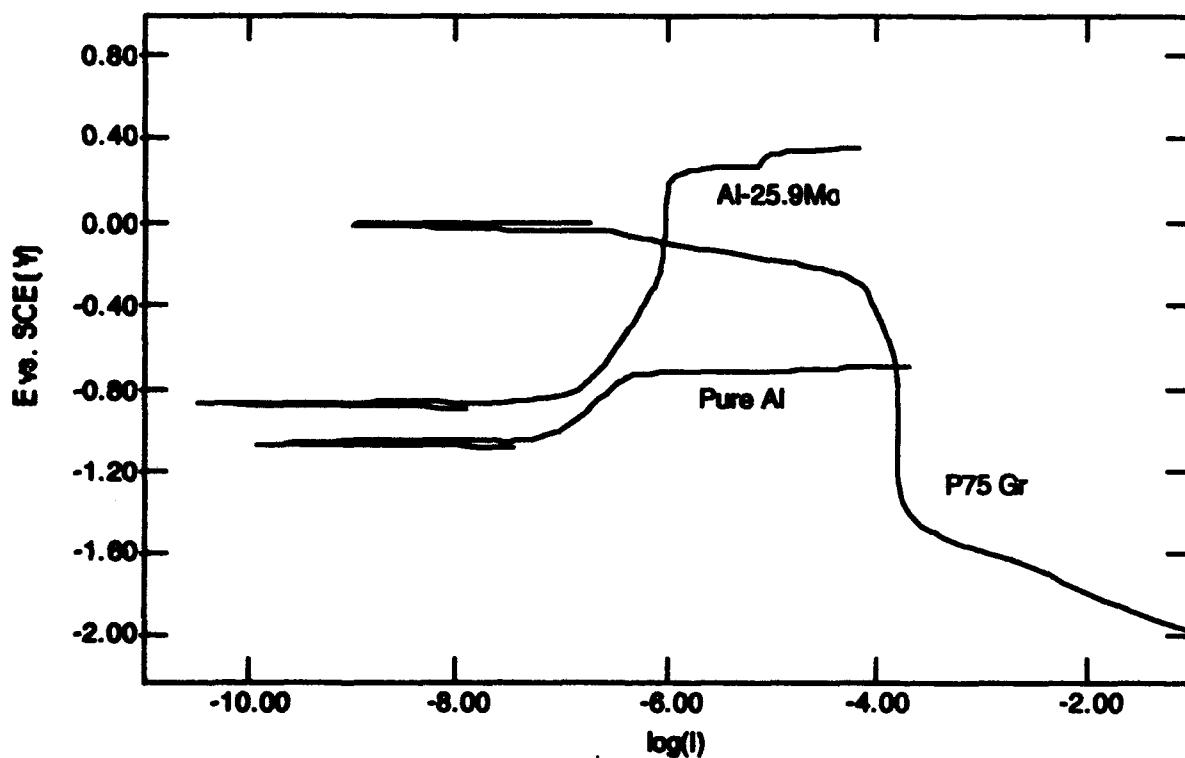
Figure 4-27. Galvanic diagrams for pure Al and Al-25.9Mo coupled with P75 graphite.
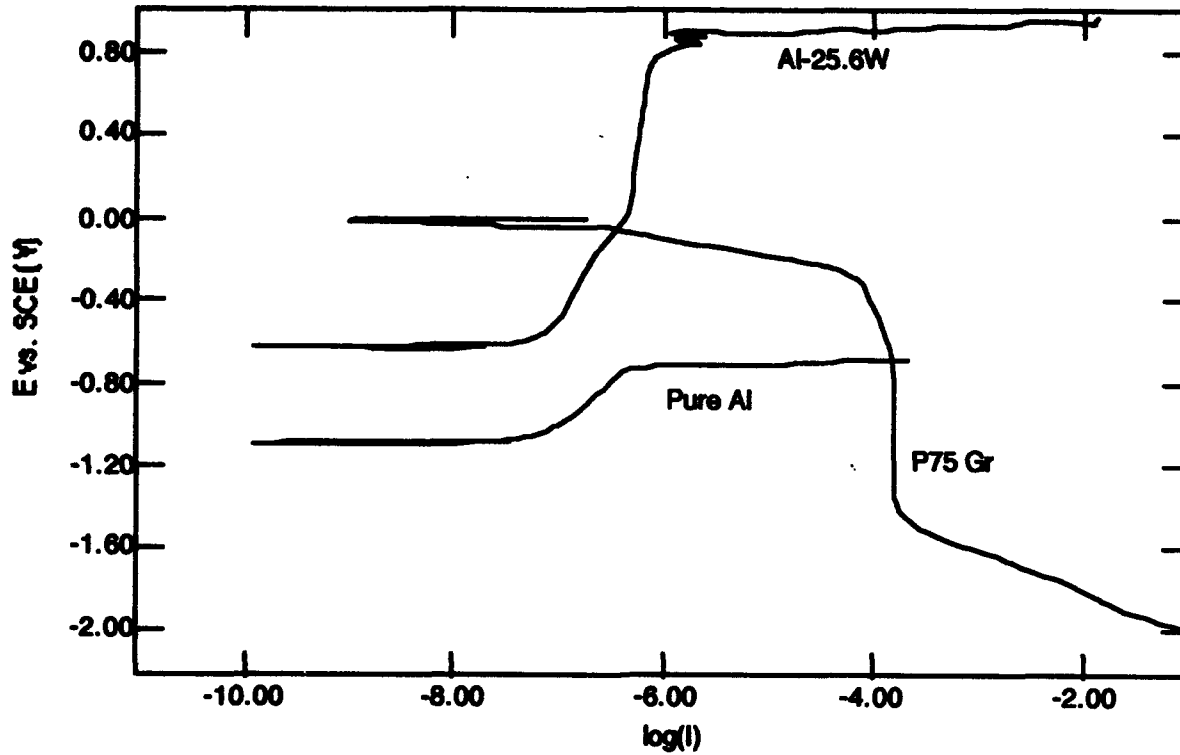
Figure 4-28. Galvanic diagrams for pure Al and Al-25.6W coupled with P75 graphite.
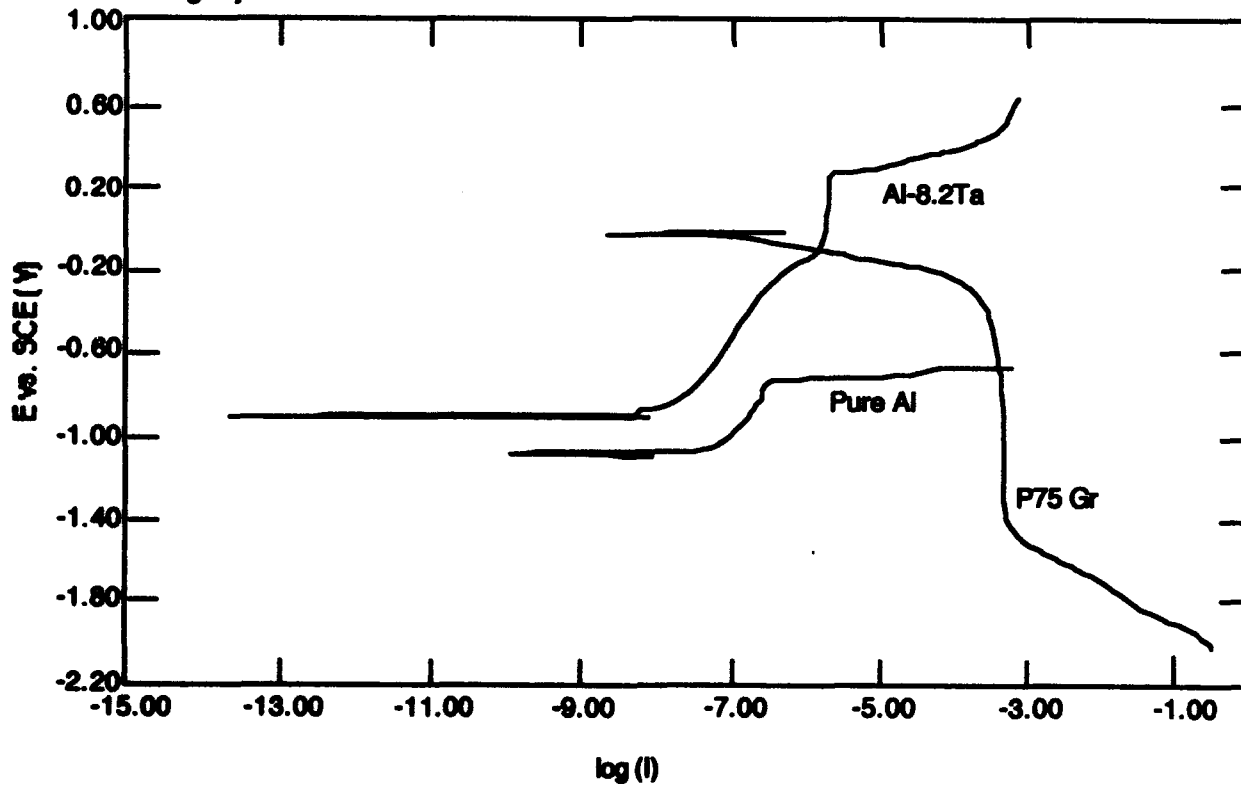
Figure 4-29. Galvanic diagrams for pure Al and Al-8.2Ta coupled to P75 graphite.

consequence of galvanic coupling. For each of the Al alloys, the cathodic oxygen reduction curve crosses the anodic curve in the passive region resulting in low galvanic corrosion rates. These diagrams share the same limitations as anodic and cathodic polarization data for the evaluation of corrosion behavior since the actual galvanic corrosion rates can be effected by changing surface conditions which may not be predicted from short-term laboratory experiments.

All of the aluminum alloys were promising from a corrosion standpoint with the largest passive regions and lowest passive current densities exhibited by the Al-W and Al-Mo alloys. Again, down-selection of alloys for phase 2 will also be dependent on the thermal stability of the alloy.

4.2 PHASE 2: CHARACTERIZATION OF DOWN-SELECTED ALLOYS

Based on a combination of corrosion performance and thermal stability, the alloys listed in Table 4-5 were chosen for further evaluation in phase 2. The ternary alloys were chosen to optimize corrosion resistance and minimize alloy density. At this stage in the research, the alloys were deposited onto both Si wafers and Gr coupons.

4.2.1 Alloy Development

Visual appearance of each of these alloys is listed in Table 4-6. Initially the sputter time was increased to 120 min to increase the thickness of material available for corrosion testing. However, after heat treating, the Mg alloys delaminated from the Si substrate. This was a result of the residual stresses in such a thick film (8 μm) coupled with the formation of a brittle Mg_2Si layer at the substrate-alloy interface. The Al alloys that were in the range of 2 μm thick did not delaminate. Figure 4-30 shows a photomicrograph of a delaminated Mg alloy. As a result, the Mg alloys were resputtered for only one hour resulting in a film approximately 4 μm thick. These alloys did not delaminate after heat treating.

53

Table 4-5. Down-Selected Alloys

Alloy	Substrate	Designation	Composition
1	Si	Al480.C.W40.S.20126.1	Al -25.9*W
	Gr	Al480.C.W40.C.20202.1	Al -25.9W
2	Si	Al480.C.Mo40.S.20127.1	Al-19.1Mo
	Gr	Al480.C.Mo40.C.20202.1	Al-19.1Mo
3	Si	Mg480.C.Al120.C.W40.S.20202.1	Mg-17.7Al-15.13W
	Gr	Mg480.C.Al120.C.W40.C.20202.1	Mg-17.7Al-15.13W
4	Si	Al480.C.Mg90.C.W40.S.20202.1	Al-2.2Mg-16.9W
	Gr	Al480.C.Mg90.C.W40.C.20202.1	Al-2.2Mg-16.9W
5	Si	Mg480.C.Ta40.C.W40.S.20202.1	Mg-14.87Ta-11.1W
	Gr	Mg480.C.Ta40.C.W40.C.20202.1	Mg-14.87Ta-11.1W
6	Si	Mg480.C.Ta40.S.20202.1	Mg-14.9Ta
	Gr	Mg480.C.Ta40.C.20202.1	Mg-14.9Ta
7	Si	Mg480.C.Cr10.S.20126.1	Mg-4.53Cr
	Gr	Mg480.C.Cr10.C.20202.1	Mg-4.53Cr

*atomic percent determined from EDS

An example of the films deposited on the Gr coupon is shown in Figure 4-31. The lines are due to the underlying Gr grain structure. No change in visual appearance occurred after heat treatment.

4.2.2 Compositional Analysis

Compositions of the 7 down-selected films determined by EDS semi-quantitative analysis along with sputter times and film thicknesses are listed in Table 4-7. These values are very similar to the ones obtained for the previous alloys. One interesting item to note is that the Ta and W concentrations were much lower for the Mg-Ta-W ternary on Gr than on the Si wafer. This was probably a result of increased fluorescence from the Si substrate.

Table 4-6. Visual appearance of Down-Selected Alloys Deposited on Si and Gr.

Alloy Designation	*	Visual Appearance
1. Al480.C.W40.S.20126.1	B	Highly Reflective, No Cloudiness
	A	Highly Reflective, No Cloudiness
1. Al480.C.W40.C.20202.1	B	Diffuse Metallic Gray, Gr Grain Boundaries Evident
	A	No Change
2. Al480.C.Mo40.S.20126.1	B	Highly Reflective, No Cloudiness
	A	Highly Reflective, No Cloudiness
2. Al480.C.Mo40.C.20202.1	B	Diffuse Metallic Gray, Gr Grain Boundaries Evident
	A	No Change
3. Mg480.C.Al120.C.W40.S.20202.1	B	Highly Reflective, No Cloudiness
	A	Highly Reflective, Slightly Clouded
3. Mg480.C.Al120.C.W40.C.20202.1	B	Diffuse Metallic Gray, Gr Grain Boundaries Evident
	A	No Change
4. Al480.C.Mg90.C.W40.S.20202.1	B	Highly Reflective, No Cloudiness
	A	—
4. Al480.C.Mg90.C.W40.C.20202.1	B	Diffuse Metallic Gray, Gr Grain Boundaries Evident
	A	No Change
5. Mg480.C.Ta40.C.W40.S.20202.1	B	Highly Reflective, Slight Cloudiness, Yellow Hue
	A	Lost Reflectivity, Metallic Appearance, Yellow Hue
5. Mg480.C.Ta40.C.W40.C.20202.1	B	Diffuse Metallic Gray, Gr Grain Boundaries Evident
	A	No Change
6. Mg480.C.Ta40.S.20202.1	B	Highly Reflective, Slight Cloudiness
	A	Gray Metallic Appearance, Cloudy
6. Mg480.C.Ta40.C.20202.1	B	Diffuse Metallic Gray, Gr Grain Boundaries Evident
	A	No Change
7. Mg480.C.Cr10.S.20126.1	B	Highly Reflective, No Cloudiness
	A	Dull Metallic Gray
7. Mg480.C.Cr10.C.20202.1	B	Diffuse Metallic Gray, Gr Grain Boundaries Evident
	A	No Change

*   A denotes after heat treatment.
    B denotes before heat treatment.

4.2.3 X-Ray Diffraction

A summary of the XRD results for the 7 down-selected alloys both on Gr and Si substrates is listed in Table 4-8. Overall, the alloys deposited on Si behaved similar to the previous alloys. Solute constituents were in solid solution, which was maintained after heat treating; however, the Mg alloys had a tendency to
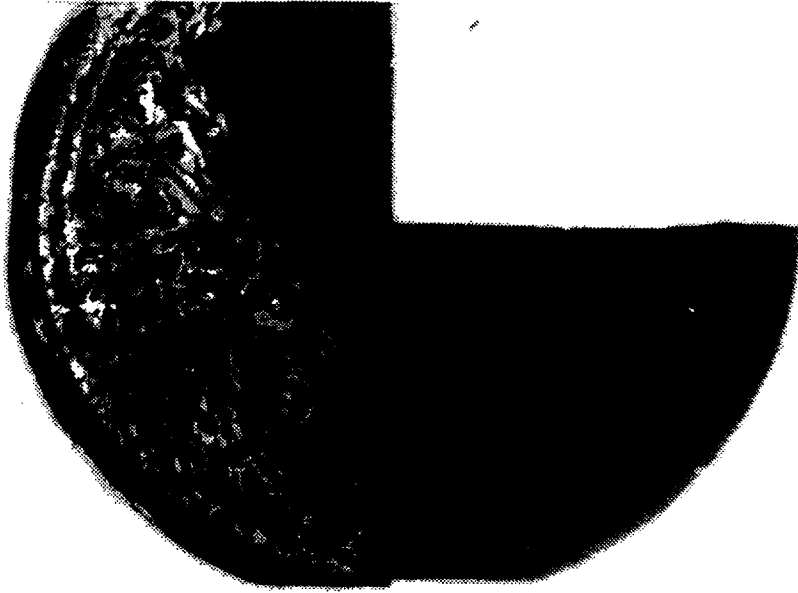
Figure 4-30. Micrograph showing delaminated Mg-Ta-W alloy after heat treatment
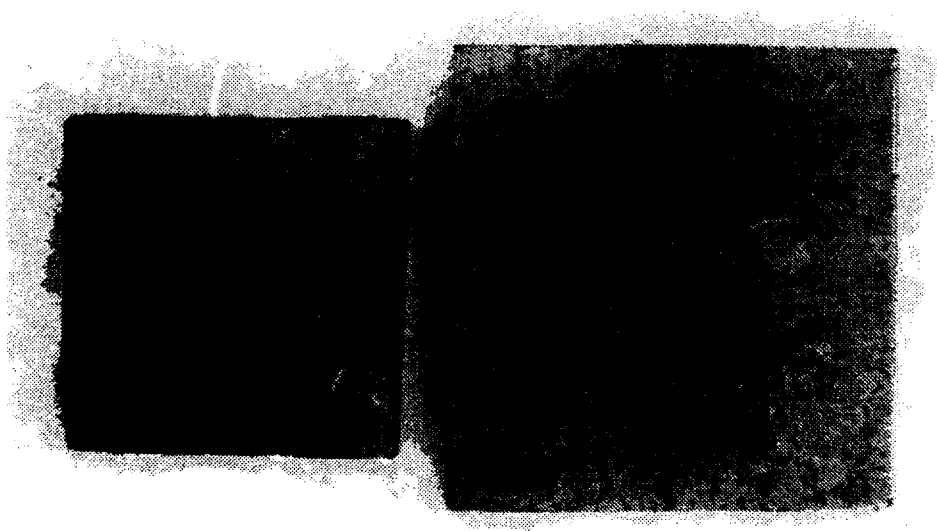
Figure 4-31. Representative appearance of non-equilibrium alloys on Gr before and after heat treating.

Table 4-7. Deposition Conditions and Concentrations of Down-Selected Alloys.

Film Designation	Sputter Time (s)	Film Thickness (nm) Predicted	Film Composition (a/o)	
			EDS	S.Dev.
Silicon Substrate				
1. Al480.C.W40.S.20126.1	120 min.	2480	25.9 at. % W	0.30
2. Al480.C.Mo40.S.20126.1	120 min.	2490	19.1 at. % Mo	0.06
3. Mg480.C.Al120.C.W40.S.20202.1	30 min.	1660	15.13 at. % W	0.84
			17.7 at. % Al	0.058
4. Al480.C.Mg90.C.W40.S.20202.1	30 min.	1460	16.88 at. % W	0.62
			2.2 at. % Mg	0.057
5. Mg480.C.Ta40.C.W40.S.20202.1	30 min.	1700	14.87 at. % Ta	0.18
			11.1 at. % W	0.87
6. Mg480.C.Ta40.S.20202.1	30 min.	1550	14.9 at. % Ta	0.98
7. Mg480.C.Cr10.S.20126.1	60 min.	2980	4.53 at. % Cr	0.21
Graphite Substrate				
1. Al480.C.W40.C.20202.1	120 min.	2480	20.32 at. % W	1.08
2. Al480.C.Mo40.C.20202.1	61 min.	1270	13.3 at. % Mo	0.10
			3.9 at. % Mg	0.47
3. Mg480.C.Al120.C.W40C.20202.1	60 min.	3320	17.6at. % W	0.57
			15.5 at. % Al	0.74
4. Al480.C.Mg90.C.W40.C.20202.1	60 min.	1460	18.1 at. % W	0.53
			3.94 at. % Mg	0.51
5. Mg480.C.Ta40.C.W40.C.20202.1	60 min.	3400	5.86 at. % Ta	0.43
			4.7 at. % W	
6. Mg480.C.Ta40.C.20202.1	30 min.	1580	17.1 at. % Ta	0.46
7. Mg480.C.Cr10.C.20202.1	60 min.	2980	13.3 at. % Cr	0.13

S. Dev = standard deviation

57

Table 4-8. Summary of X-ray Diffraction for Down-Selected Mg-Base and Al-Base Transition Metal Alloys (* SS = solid solution, P = precipitate).

Film Designation	Before Heat Treatment	*	After Heat Treatment	*
1. AI480.C.W40.S.20126.1	Broad Al Peaks, Amorphous ?	SS	No Change	SS
1. AI480.C.W40.C.20202.1	Broad Al Peaks, Amorphous ?	SS	No Change	SS
2. AI480.C.Mo40.S.20126.1	Broad Al Peaks, Amorphous ?	SS	No Change	SS
2. AI480.C.Mo40.C.20202.1	Broad Al Peaks, Amorphous ?	SS	No Change	SS
3. Mg480.C.Al120.C.W40.S.20202.1	Mg and Broad Al Peaks, Amorphous ?	SS	No Change, Mg2Si	SS
3. Mg480.C.Al120.C.W40.C.20202.1	Mg and Broad Al Peaks, Amorphous ?	SS	No Change	SS
4. AI480.C.Mg90.C.W40.S.20202.1	Broad Al Peaks, Amorphous ?	SS	No Change	SS
4. AI480.C.Mg90.C.W40.C.20202.1	Broad Al Peaks, Amorphous ?	SS	No Change	SS
5. Mg480.C.Ta40.C.W40.S.20202.1	Mg and Ta Peaks	P	Ta Peak Intensity Increased	P
5. Mg480.C.Ta40.C.W40.C.20202.1	Mg and Ta Peaks	P	Ta Peak Intensity Increased	P
6. Mg480.C.Ta40.S.20202.1	Mg and Ta Peaks	P	Ta Peak Intensity Increased	P
6. Mg480.C.Ta40.C.20202.1	Mg and Ta Peaks	P	Ta Peak Intensity Increased	P
7. Mg480.C.Cr10.S.20126.1	Mg Peaks	SS	No Change, Mg2Si	SS
7. Mg480.C.Cr10.C.20202.1	Mg Peaks	SS	No Change	SS

react with the Si wafer. Patterns for alloys deposited on Gr were much more difficult to interpret due to the large number of Gr peaks. It appears there was little or no change after heat treating, which indicates no precipitation of the solute or reaction with the Gr substrate. Details of the XRD results for each of the 7 down selected alloys are presented below.

Alloy #1
Al-W (Al-25.9 at.% W)

The XRD patterns for the Al-W on Si and Gr are shown in Figure 4-32 and Figure 4-33, respectively. The pattern for the Al-W on Si looks very similar to what was found in the first phase of this program. Ignoring the Si peaks, the only peaks found were a very broad peak at 21° and a higher intensity broad peak at $2\theta = 40°$. As was discussed earlier, these do not correspond exactly to any Al peak. We suspected this was due to a combination of the

58

Figure 4-32. X-ray Diffraction Patterns for A1480.C.W40.S.20126.1 (Alloy #1, on Silicon) Before and After Heat Treating (HT)

A1480.C.W40.S.20126.1

A1480.C.W40.S.20126.1 HT

6500

0

59
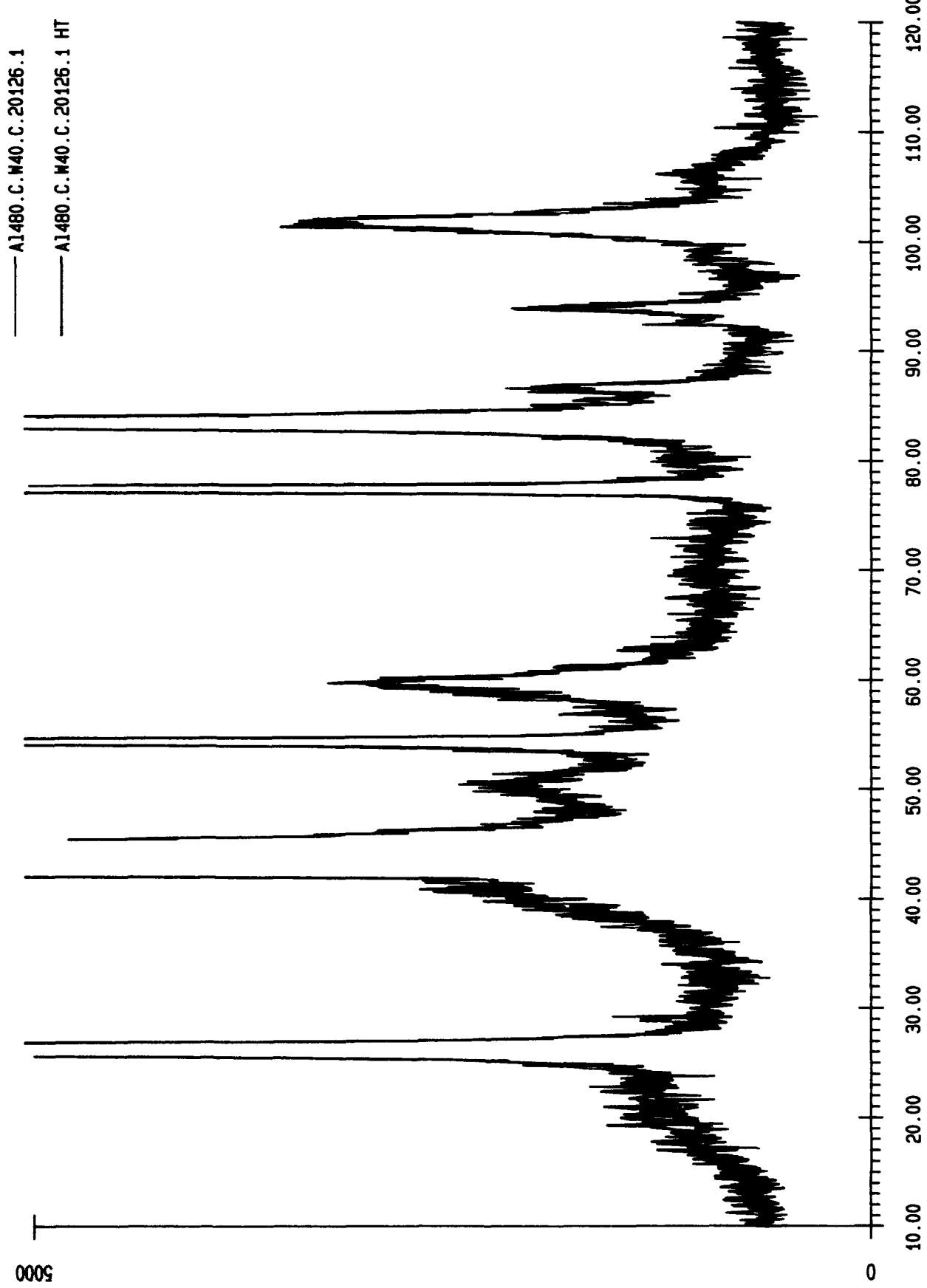
Figure 4-33. X-ray Diffraction Patterns for Al480.C.M40.C.20126.1 (Alloy #4, on Graphite) Before and After Heat Treating (HT)

Legend:
- Al480.C.M40.C.20126.1
- Al480.C.M40.C.20126.1 HT

ultrafine grain size giving the appearance of an amorphous structure combined with the possibility of improper alignment of the highly textured sputtered films. Therefore, it was assumed the broad 41° peak was W solid solution with Al. The diffraction pattern did not change after heat treatment indicating W was retained in solid solution.

The broad peak at 21° was also found for the Al-W films on Gr. Unfortunately, 41°(where the other broad peak was found for Al-W on Si) also corresponds to one of the Gr peaks. Close examination does show a slight hump on the small angle side of the Gr peak that is likely the 41° peak. In addition, Al peaks were found at 2θ of 38.4°, 44.7°, and 65.1° for the (111), (200), and (220) planes, respectively. Although it is difficult to interpret this pattern, no additional peaks were present after heat treating which indicates W was retained in solid solution in Al and the alloy did not react with the Gr coupon.

Alloy #2
Al-Mo (Al-19.1 at.% Mo)

XRD patterns for the Al-Mo alloy were very similar to that shown for the Al-W alloy (alloy #1). Again, the broad peaks were present at 21° and 41°. As with the Al-W alloy, the pattern indicated an ultrafine grain, textured aluminum with Mo in solid solution. No change occurred after heat treatment which indicates that the Mo was retained in solid solution.

The diffraction pattern for Al-Mo on Gr showed two broad peaks at 21° and 41°, as well as, Al peaks at 2θ of 38.4°, 44.7°, and 65.1° for the (111), (200), and (220) planes, respectively. Therefore, Mo was in solid solution for the Al-Mo on Gr. No new peaks were found after heat treatment which indicates Mo was retained in solid solution and the Al did not react with the Gr coupon.

Alloy #3
Mg-Al-W (Mg-17.7 at.%-15.1 at.% W)

XRD patterns for the Mg-Al-W ternary alloy were very unusual because the broad peak found in the Al-W and Al-Mo was apparent, but at a much lower

61

intensity. On top of this broad peak were the normal Mg peaks at 34.1°, 36.1° and 47.9°. In addition, broad peaks were found at 21° and 41°, similar to the Al-W pattern. After heat treating, the typical Mg_2Si peaks appeared, but the Mg peaks disappeared. The peaks at 21° and 41° were unchanged. This result lead us to conclude that the film was deposited as a two phase structure consisting of Mg and an Al-W alloy. The Mg reacted with and was consumed by the Si substrate during heat treatment, while the Al-W phase remained unchanged.

The diffraction data for the Mg-Al-W alloy on Gr also showed broad peaks at ~21° and 41° characteristic of the Al-W and Al-Mo. Close examination also revealed the Mg peaks at 32.1° and 34.8°. We concluded from this pattern that the Mg and Al did not react with the Gr, and that Al and W were retained in solid solution prior to and after heat treating, similar to the film deposited on the Si wafer. In this case, Mg is still present after heat treatment because it could not react with the Gr substrate.

Alloy #4
Al-Mg-W (Al-16.9 at%W-2.2 at.%Mg)

As a result of the problem with film delamination, XRD was not performed for this alloy deposited on the Si wafer. The diffraction pattern for the Al-Mg-W alloy on Gr (Figure 4-34) shows the same broad peaks at ~21° and 41° that were noted for all the Al alloys. Other than the Gr peaks, no additional peaks were found indicating that the Mg and W were in solid solution with the Al prior to and after heat t. eating, and the alloy did not react with the Gr coupon.

Alloy #5
Mg-Ta-W (Mg-14.4 at.%Ta-11.1 at.%W)

The diffraction patterns for the Mg-Ta-W ternary alloy were very difficult to analyze because of the large number of overlapping peaks. The pattern before heat treatment showed a broad hump on the side of the 36.4° Mg peak which appeared to be the Ta 38.4° peak corresponding to the (111) plane.
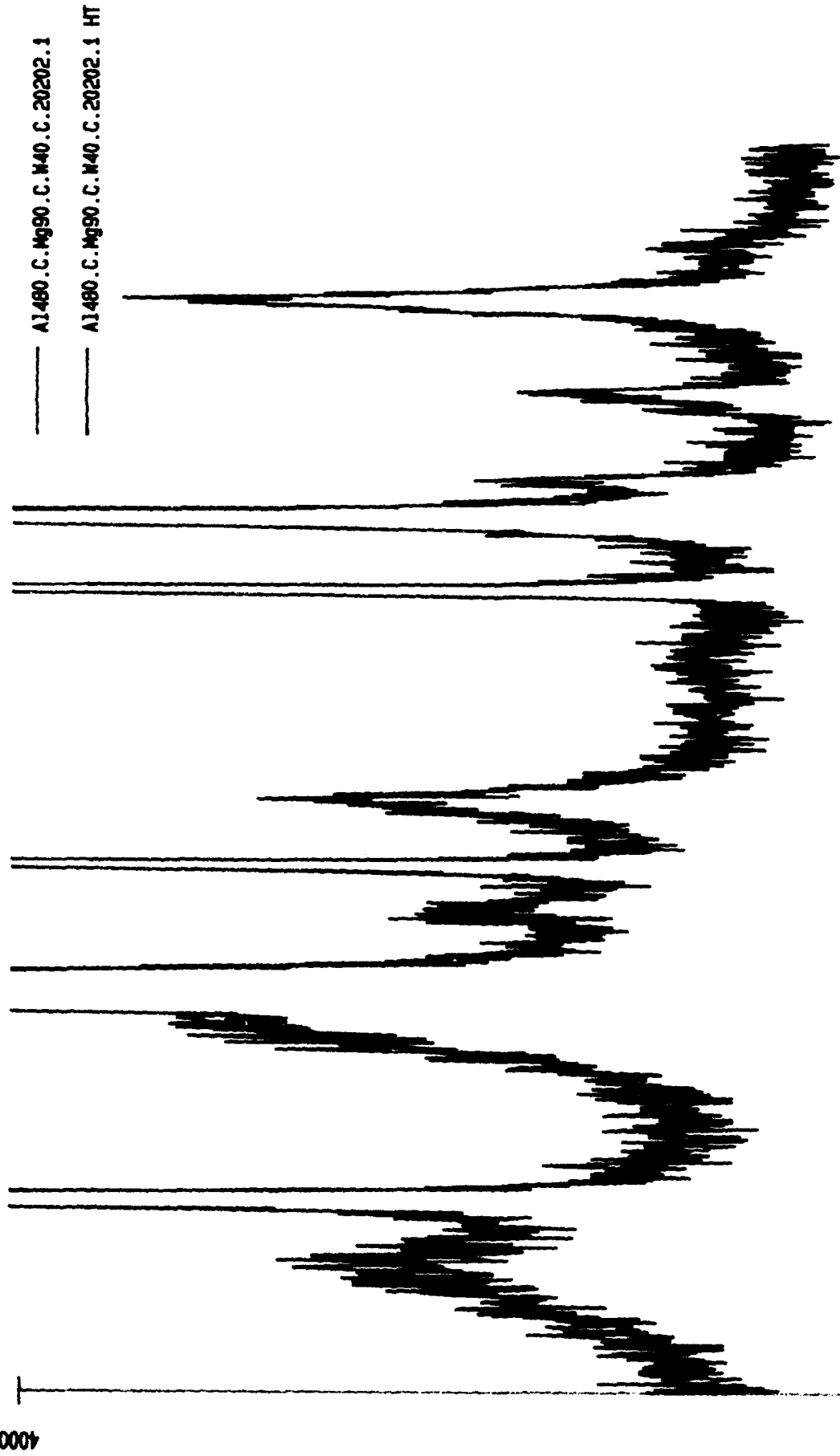
Figure 4-34. X-ray Diffraction Patterns for A1480.C.Mg90.C.M40.C.20202.1 (Alloy A4 on Graphite) Before and After Heat Treating (HT)

Legend:
- A1480.C.Mg90.C.M40.C.20202.1
- A1480.C.Mg90.C.M40.C.20202.1 HT

The source of the Ta may have been unsputtered Ta particles that were typically found on the Ta alloys. (We believe that a defective target was responsible for the unsputtered Ta particles in the deposit.) After heat treatment, the 38.4° peaks became much stronger. On the side of the 38.4° peak was the normal Mg_2Si peak at 40°. Due to the large change in Ta peaks intensity after heat treating, it appears Ta was precipitating.

For the Mg-Ta on Gr, the diffraction pattern was dominated by the Gr peaks, with Mg peaks at 34.8°, 47.9°, and 72.4°. However, the broad peak at 38.4° indicated that free Ta was present, and because the intensity of this peak increased after heat treatment, separation of the Mg and Ta is probably occurring.

Alloy #6
Mg-Ta (Mg-14.9 at.% Ta)

Diffraction patterns for the Mg-Ta alloy on Si and Gr are shown in Figures 4-35 and 4-36, respectively. The pattern on Si showed the very strong Mg peaks at 34.8° and 36.4° and 72.8°. Although a Ta peak was not found, the broad tapering of the 36.4° Mg peak was likely due to free Ta. The source of the free Ta may have been the small Ta particles that were found on the alloys containing Ta. After heat treating, the typical Mg_2Si peaks were present. From these patterns it is difficult to determine whether Ta is present in solid solution and if it remains in solid solution after heat treating. The free Ta particles will likely promote increased corrosion rates as a result of microgalvanic coupling with the Mg.

The XRD pattern for Mg-Ta on Gr showed Mg peaks with a Ta peak at 38.4°. Again, this alloy is not a good candidate for further investigation because of its thermal instability.

Alloy #7
Mg-Cr (Mg-4.53 at.% Cr)

As for the other Mg alloys, the peaks noted before heat treating were for Si and Mg. After heat treating, the Mg_2Si peaks appear indicating a reaction with the substrate.
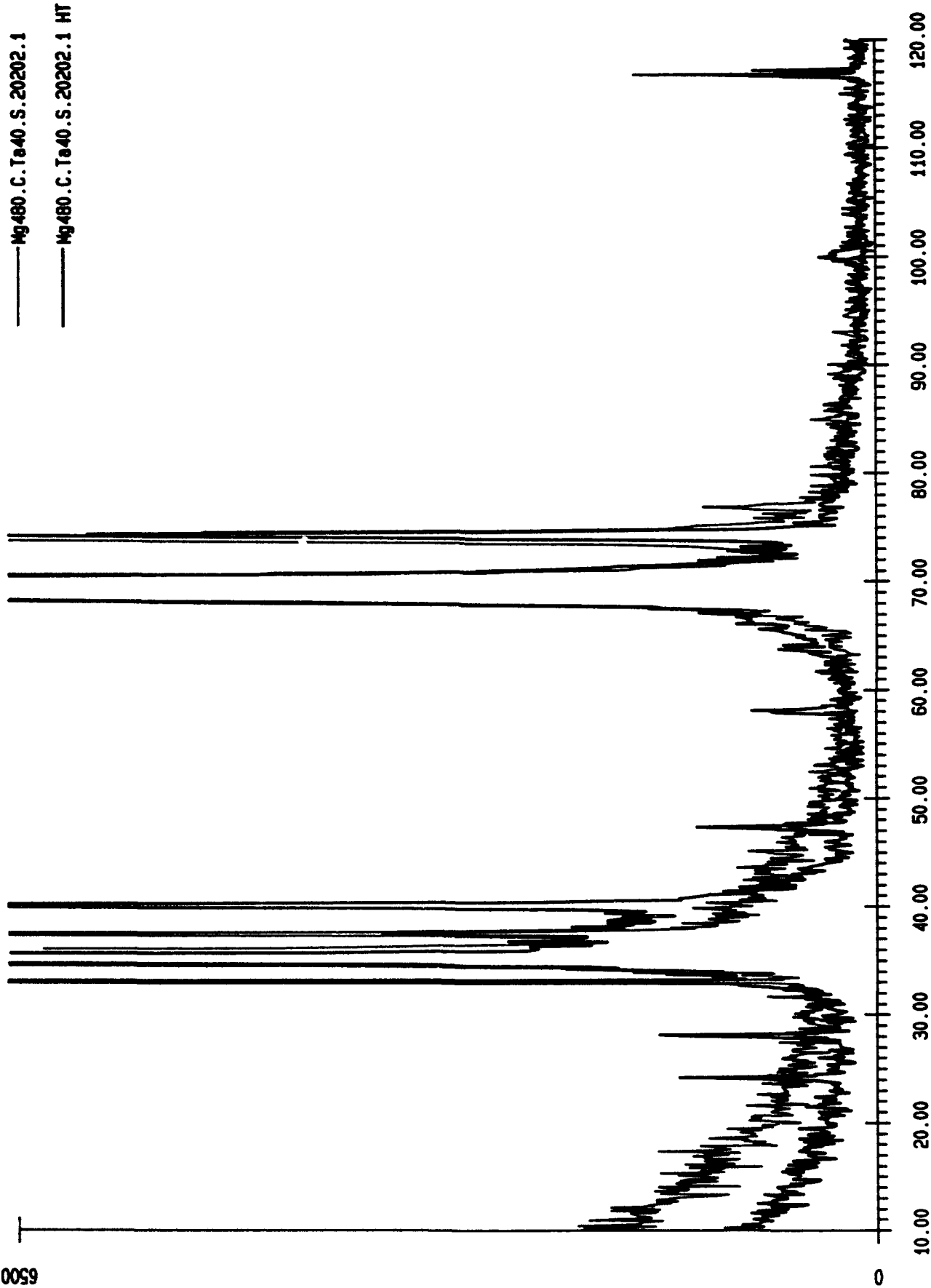
Figure 4-35. X-ray Diffraction Patterns for Mg480.C.Ta40.S.20202.1 (Alloy #6, on Silicon) Before and After Heat Treating (HT)

— Mg480.C.Ta40.S.20202.1
— Mg480.C.Ta40.S.20202.1 HT

6500

0

65

Figure 4-36. X-ray Diffraction Patterns for Mg480.C.Ta40.C.20202.1 (Alloy #6 on Graphite) Before and After Heat Treating (HT)
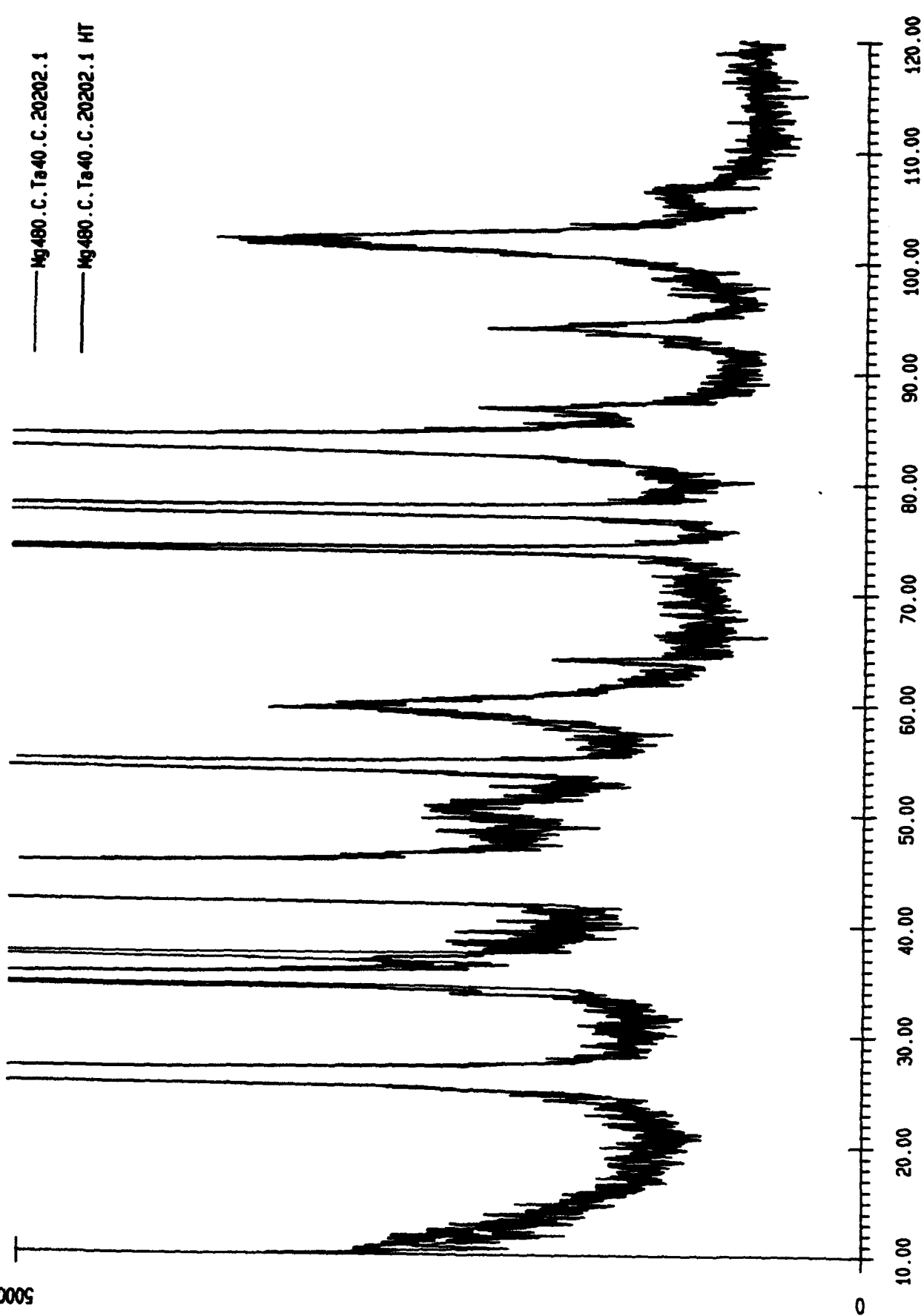
Mg480.C.Ta40.C.20202.1

Mg480.C.Ta40.C.20202.1 HT

66

For Mg-Cr on Gr, no new peaks were evident, indicating Cr was maintained in solid solution. Following the heat treatment, diffraction patterns of Mg-Cr on Gr revealed the typical Gr peaks and Mg peaks at 34.8°, 36.4°, 63.1°. No additional peaks were present indicating Cr was in solid solution and remained in solid solution following heat treatment.

4.2.4   Corrosion Testing

Anodic Polarization Behavior

Alloys 1,2 and 4 (the Al-25.9%W alloy, the Al-19.1%Mo alloy and the Al-2.2Mg-16.9%W alloy) exhibited excellent corrosion performance in the 0.1M NaCl environment with pitting potentials 1200 to 1330 mV higher than that of pure Al. The anodic polarization behavior of these alloys are compared to that of pure sputtered Al in Figure 4-37. Characteristic parameters derived from the polarization curves for these alloys are presented in Table 4-9. Similar passive current densities and pitting potentials were noted for the three alloys. The i_p values for the alloys of approximately 1 µA/cm² are similar to that observed for pure Al prior to pitting--suggesting that the alloy passive films may be closer in composition to the film which forms on pure Al than the films which form on either pure W or pure Mo. Enhanced passivity does not appear to be based solely on solute concentration since equivalent behavior was observed for both the Al-25.9%W and the Al-2.2%Mg-16.9%W alloys. This is important because the addition of Mg and the reduction in W concentration have a significant effect on the final density of the alloy.

The most encouraging attribute of the high solute Al-Mo and Al-W alloys is that they retain their enhanced corrosion resistance after heat treatment for 1 hour at 400 °C. Figures 4-38 and 4-39 show the anodic polarization behavior in 0.1 M NaCl for the Al- 25.9%W and the Al-19.1%Mo alloys, respectively, both before and after heat treatment. No evidence of diminished performance after heat-treatment was observed for either alloy. Again, the curves presented in these figures are representative curves, but as Table 4-9 reveals, only small differences were observed for the replicate specimens. The absence of Al-Mo and Al-W precipitates in the heat-treated alloys and the concomitant undiminished polarization behavior are essential for fabrication since the

67
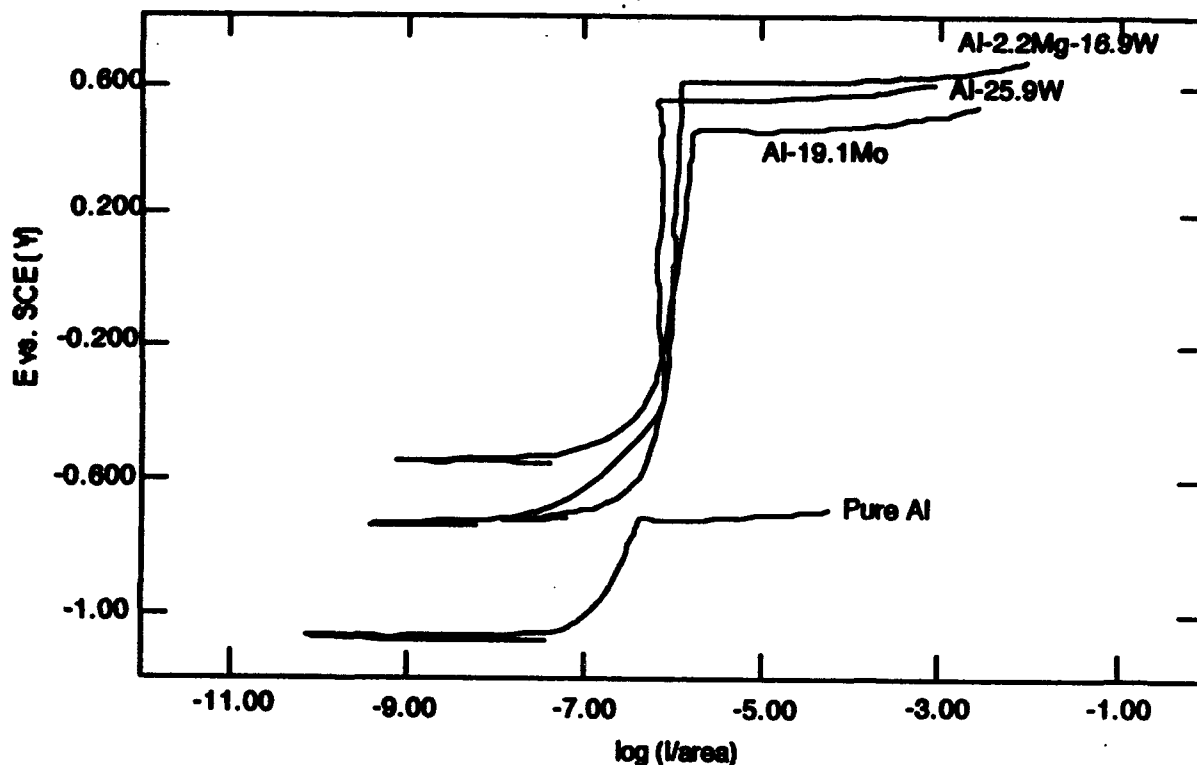
Figure 4-37. Anodic polarization behavior of alloys 1-3 compared to pure aluminum, all deposited on Si.

Table 4-9. Anodic polarization data in .1 M NaCl (pH=8) for the phase 2 Al alloys (HT = heat-treated, ** = average).

| SAMPLE	SCAN (mV/s)	Ecorr (mV-SCE)	Eb (mV-SCE)	Ipass (A/cm)
Al - 19.1 Mo	0.2	-490	320	1.26
Al - 19.1 Mo	0.2	-545	470	1.26
Al - 19.1 Mo (HT)	0.2	-565	400	9.52
Al - 19.1 Mo (HT)	0.2	- - -	410	0.50
Al - 19.1 Mo (HT)	0.2	-595	445	1.00
Al - 19.1 Mo (HT)	0.05	-590	440	1.00
Al - 19.1 Mo (HT)	0.008	-560	400	0.60**
Al - 25.9 W	0.2	-700	500	4.50**
Al - 25.9 W	0.2	-745	550	0.63
Al - 25.9 W	0.2	-740	550	0.63
Al - 25.9 W (HT)	0.2	-775	550	0.63
Al - 25.9 W (HT)	0.2	-775	545	0.63
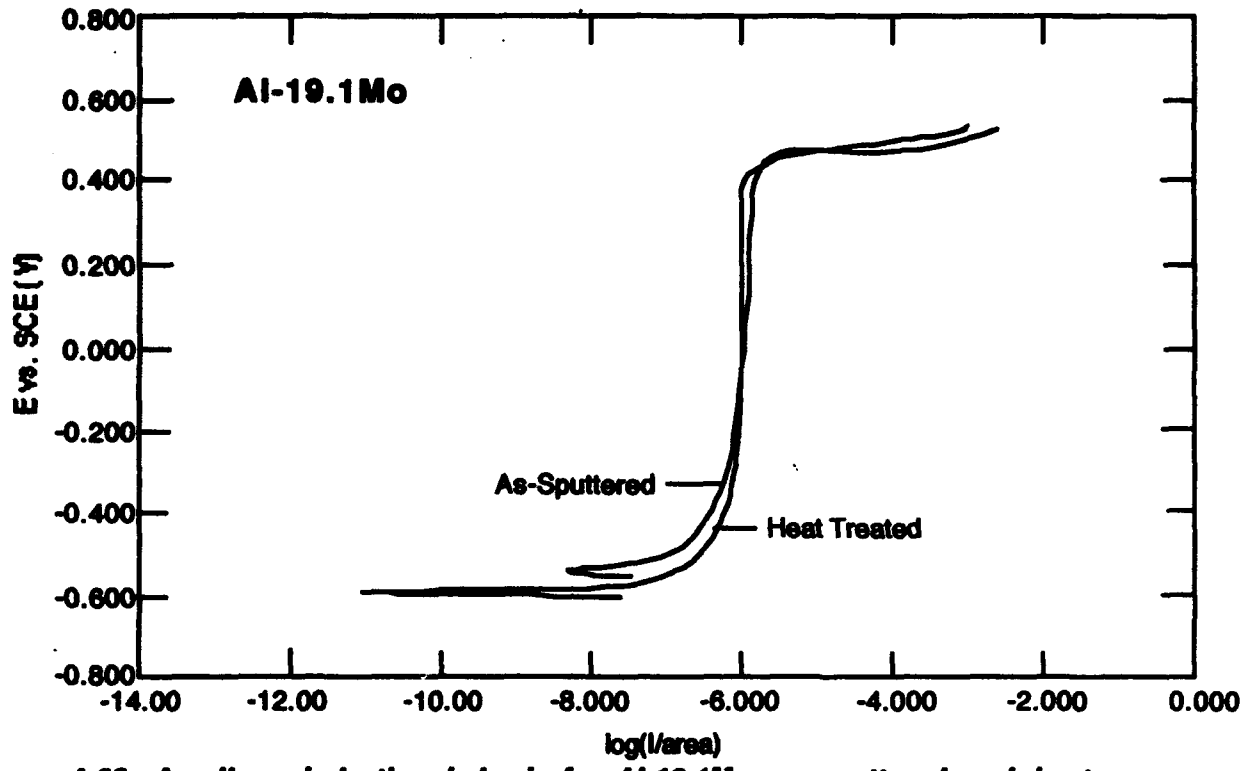
Figure 4-38. Anodic polarization behavior for Al-19.1Mo, as-sputtered and heat-treated.
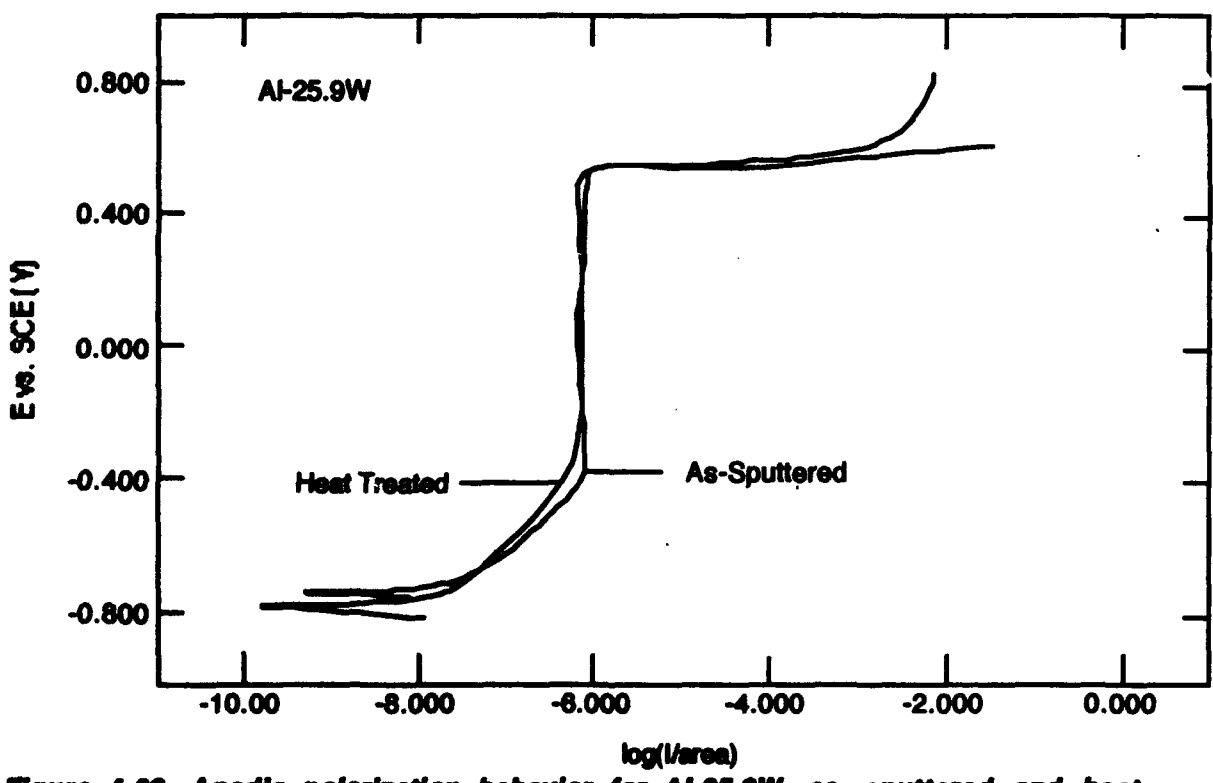

Figure 4-39. Anodic polarization behavior for Al-25.9W, as-sputtered and heat-treated.

alloy coated fibers will need to be HIPed to consolidate the composite. Because of problems with our heat treating apparatus, results are not yet available for heat-treated sample 4.

Sample 3, the Mg-17.7 at.%Al-15.13 at.%W alloy, also exhibited passivity; but, unlike the previous three alloys, this alloy was not self-passiviating and a large active-passive transition was noted between -1100 and -840 mV. Figure 4-40 shows the anodic polarization behavior for this alloy in 0.1M NaCl. This curve reveals a relatively high i_p of approximately 100 μA/cm^2. Potentiostatic polarization at -700 mV for 5 hours, Figure 4-41, showed that with time, i_p dropped to a value of 20μA/cm^2. The large active-passive transition for this alloy could be a problem if this alloy was galvanically coupled to a material such a graphite. Coupling of the MgAlW and graphite polarization curves (considering equal areas) would result in crossover of the two in the active nose of the anodic curve with corrosion of the matrix metal being driven by oxygen reduction on the graphite. Passivity was not observed for alloys 5-7 (Mg-14.87at.%Ta-11.1at.%W, Mg-14.9at.%Ta, or Mg-4.53at.%Cr) and, as was illustrated earlier, their galvanic compatibility with graphite is dependent on the respective E_{corr} values.

The implications of the enhanced passivity of alloys 1 and 2 with regard to their galvanic corrosion performance are presented in the galvanic diagrams shown in Figures 4-42 through 4-44. As these figures reveal, the galvanic performance of the Al-19.1%Mo and the Al-25.9% W alloys are essentially identical to the performance noted earlier for the Al alloys with the high W and Mo concentrations. In all cases, the cathodic oxygen reduction reaction crosses the anodic polarization curve in the passive region and low galvanic corrosion rates for the matrix metal are predicted. Since the polarization behavior of heat-treated alloy 1 and alloy 2 were the same as the nonheat-treated alloys, the galvanic diagrams for these alloys would show identical behavior.

As a result of surface connected cracks in the alloys deposited on graphite, it was not possible to gain the same degree of information from the polarization data on these specimens that was gained from the previous experiments. To date, alloys 1, 2, 4, and the controls have been evaluated. All of the specimens
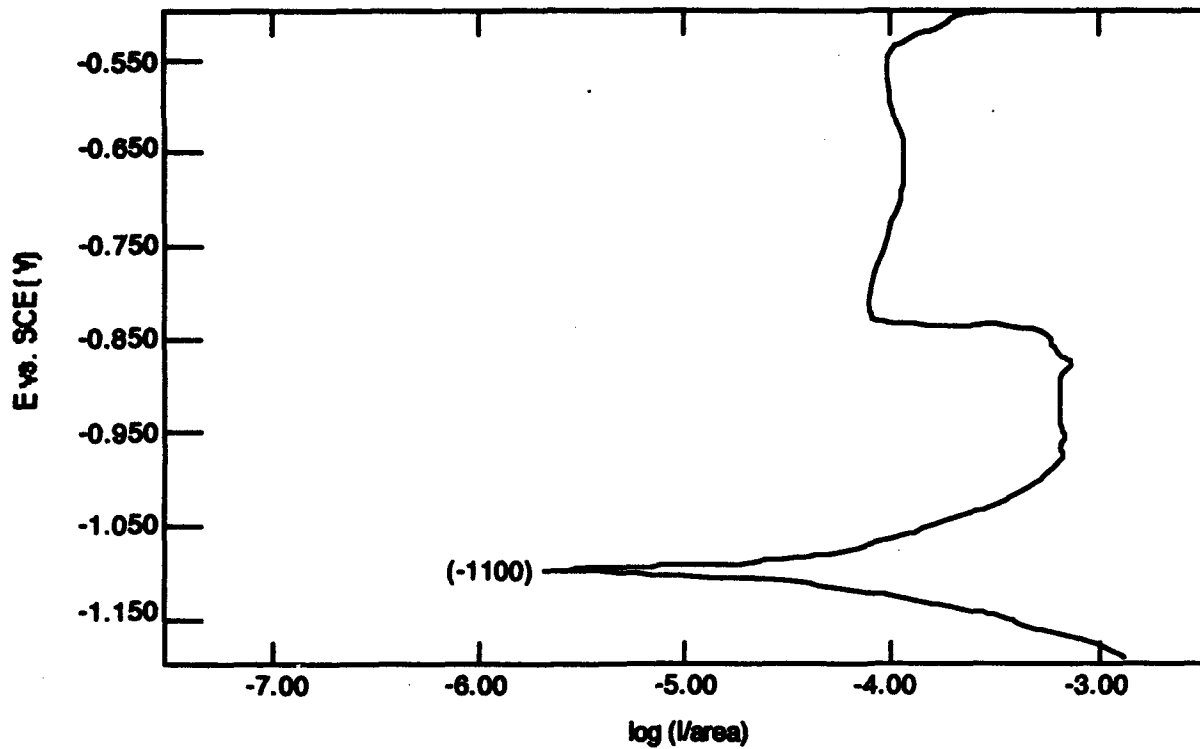
**Figure 4-40. Sample #3, the MgAlW alloy, showing a large active-to-passive transition.**
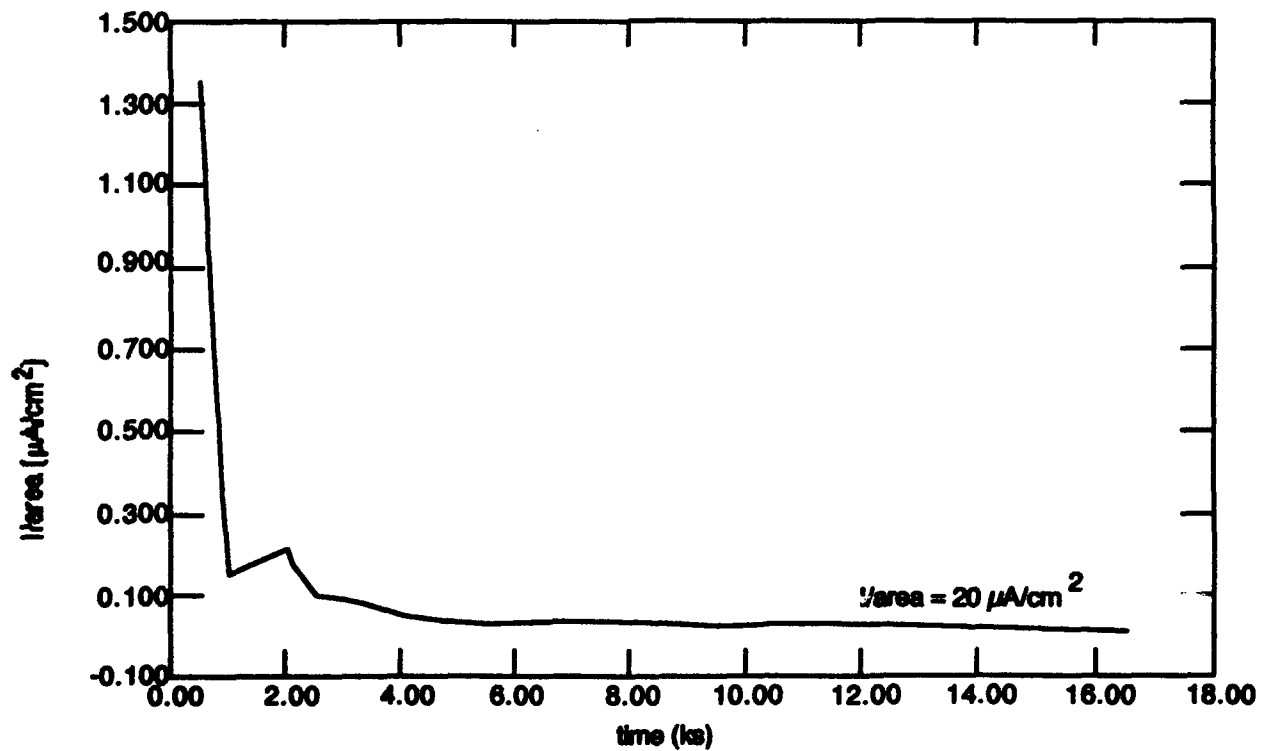
Figure 4-41. Potentiostatic polarization curve for MgAlW (sample #3).

71
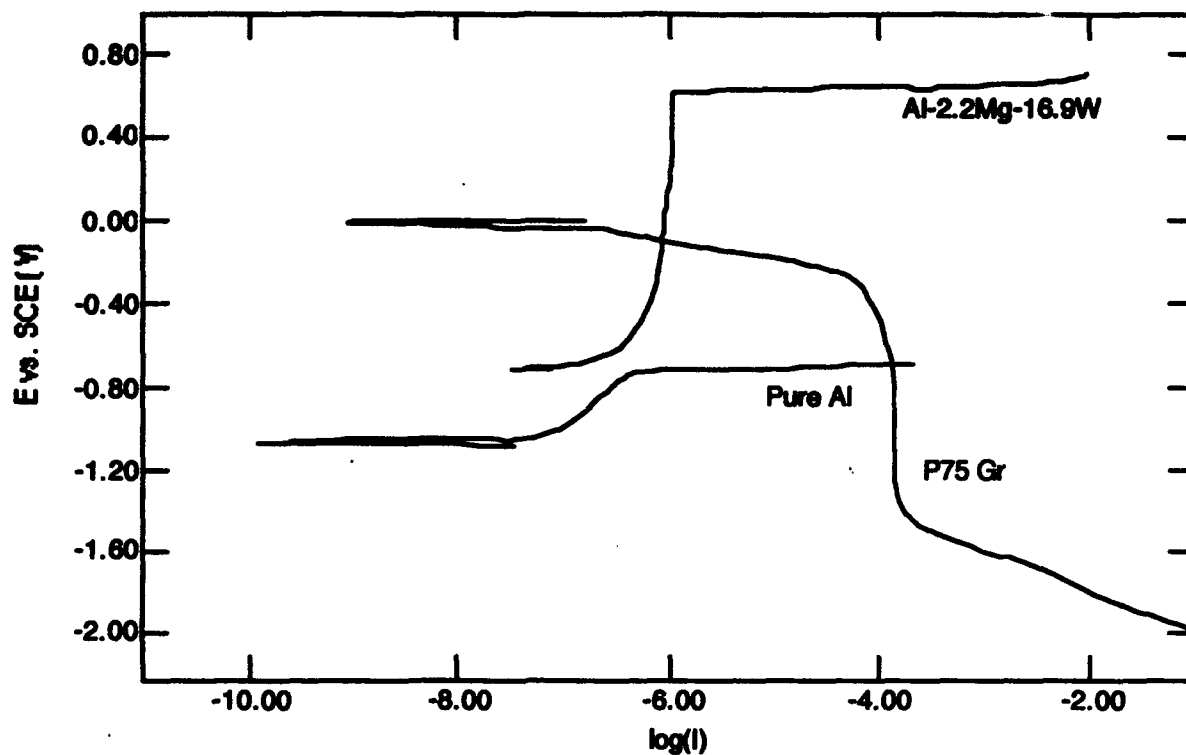
Figure 4-42. Galvanic diagram for pure Al and Al--16.9W-2.2Mg (sample #4) coupled to P75 graphite.
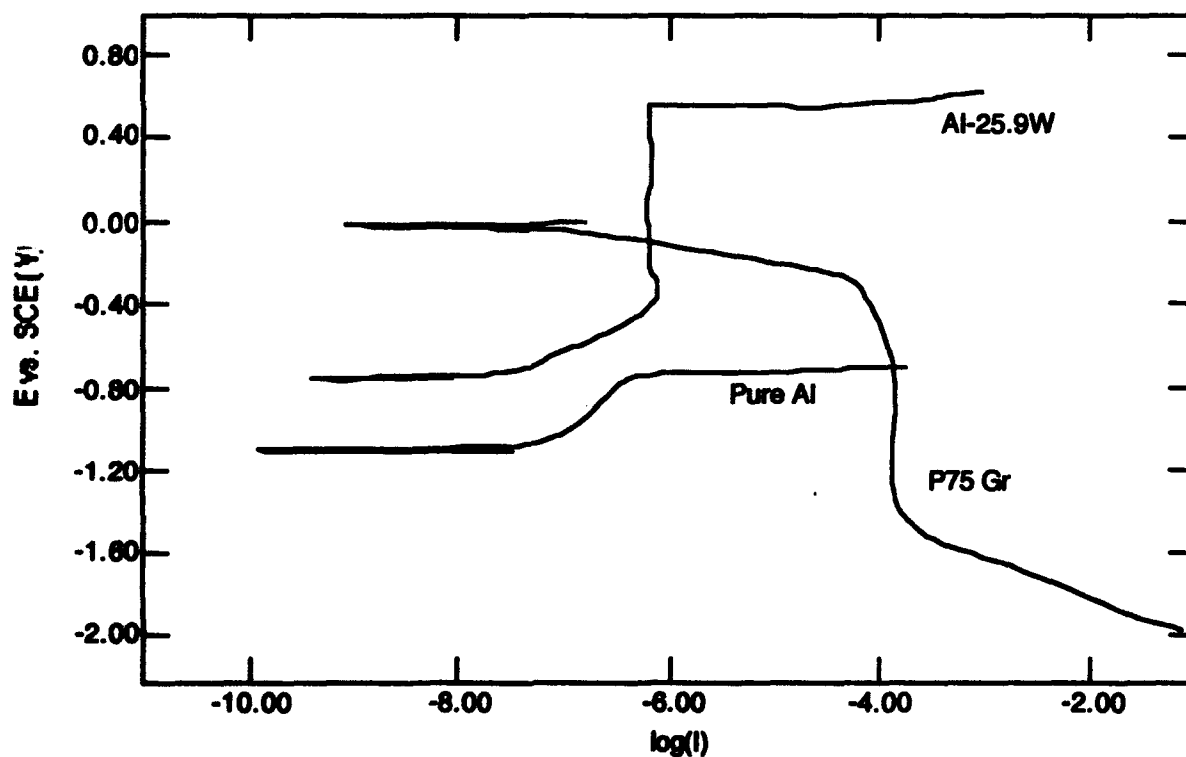

Figure 4-43. Galvanic diagrams for pure Al and Al-25.9W (sample #2) coupled to P75 graphite.

72
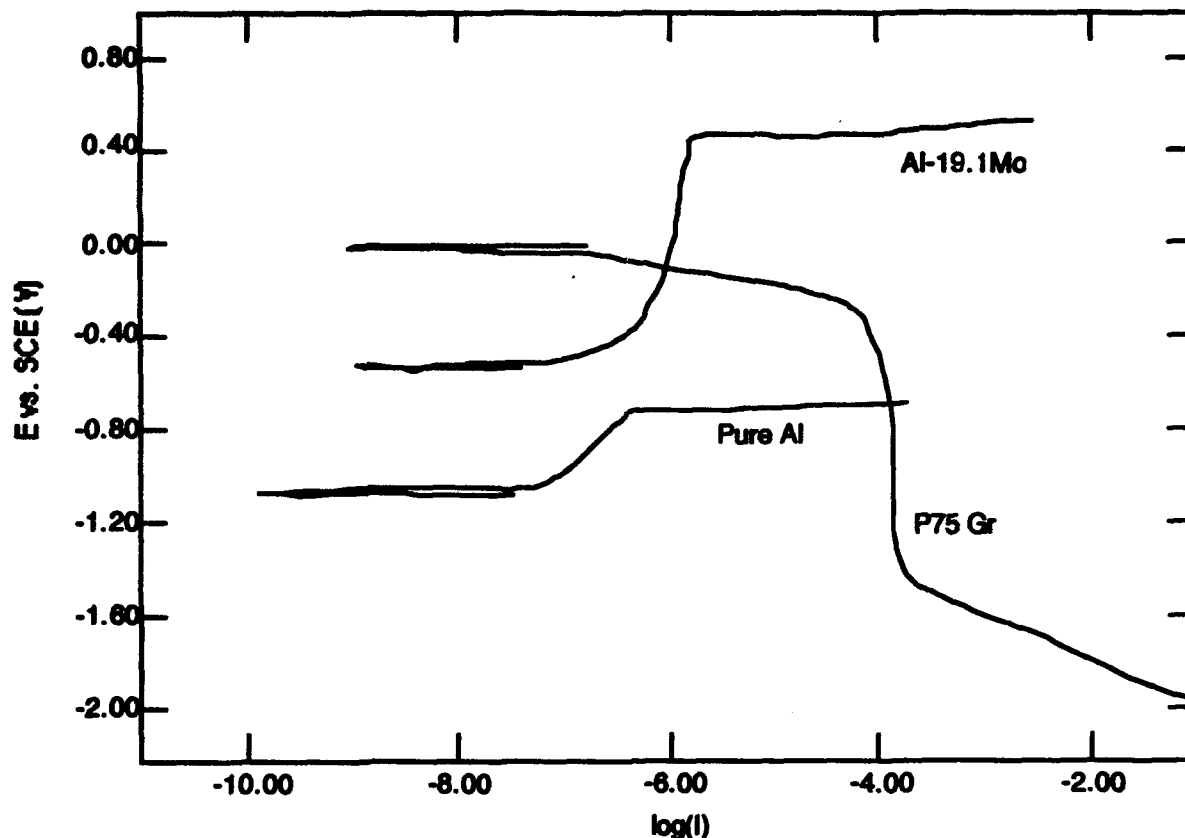
Figure 4-44 Galvanic diagrams for pure Al and Al-19.1Mo (sample #1) coupled to P75 graphite

exhibited E_{corr} values more noble than the values reported for the same alloys on Si substrates. This positive shift in E_{corr} is most likely a function of the exposed graphite substrate. It is not known how much graphite was exposed. From the polarization curves it was evident that at E_{corr}, alloys 1, 2, and 4 were passive and the controls were not . Figure 4-45 shows the initial portion of a polarization curve for the Al-25.9 at. %W alloy (alloy #2) on graphite. Visual analysis of the specimen in the passive region revealed that the surface was virtually unchanged as a result of exposure. Scanning electron microscopy of the passive surface showed no pits and a surface similar in nature to the unexposed material. This passive region was also observed on the heat-treated specimens at E_{corr} and at low overpotentials.

73
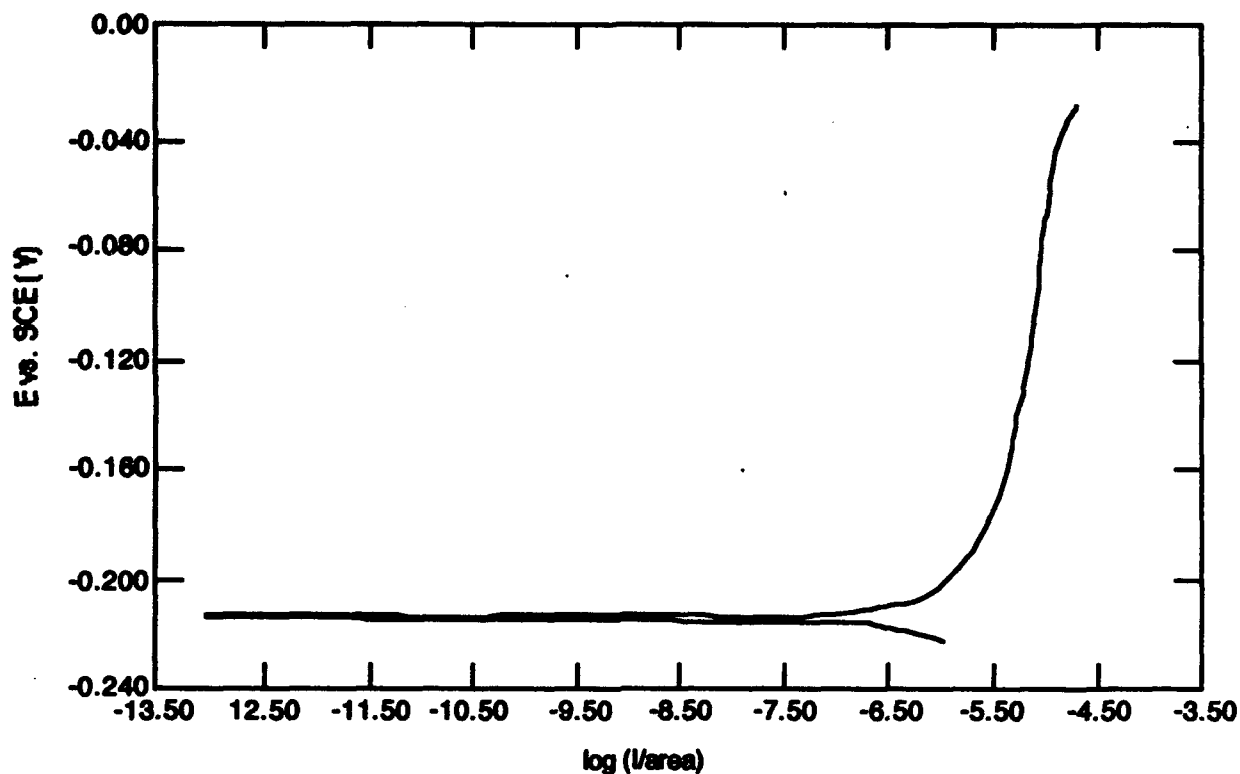
Figure 4-45. Initial portion of polarization curve for Al-25.9 at.% W alloy (alloy #2) deposited on graphite.

Galvanic Current Measurements

To confirm the predictions made using the galvanic diagrams, long-term galvanic current measurements were taken for alloys 1 and 2 coupled to P75 graphite. A similar experiment was also conducted on pure sputtered Al coupled to P75 graphite. Representative results are presented in Figures 4-46 to 4-48. Figure 4-46 shows the galvanic current measured for one of the two Al-19.1%Mo alloy (alloy 1) specimens coupled to P75 graphite. The cathode to anode area ratio for this couple was 0.41. Initially, currents of slightly less than 3 μA were observed which fell off quickly to a value of approximately 0.1 μA after 1 hour. After sixteen hours, the current dropped to a steady state value of 0.05 μA and remained constant for the duration of the experiment. The steady state current of 0.05 μA corresponds to a current density of 0.16 μA/cm^2. The other galvanic couple for this alloy had a cathode to anode area ratio of 0.15 and exhibited an initial current of 4.4 μA which fell off to a value of 0.8 μA after
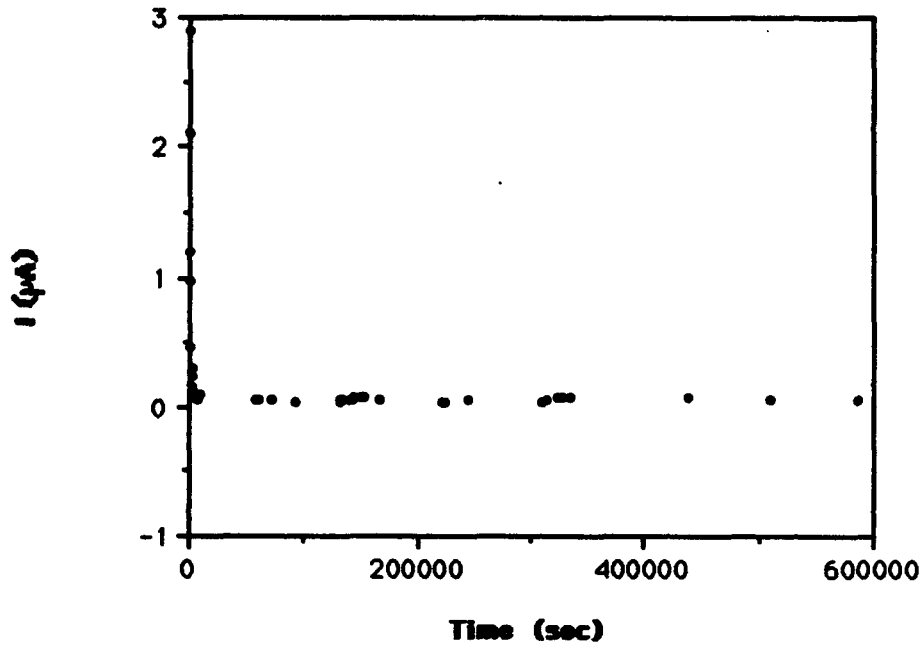
*Figure 4-46. Galvanic current diagram for AlMo/P75 graphite couple.*
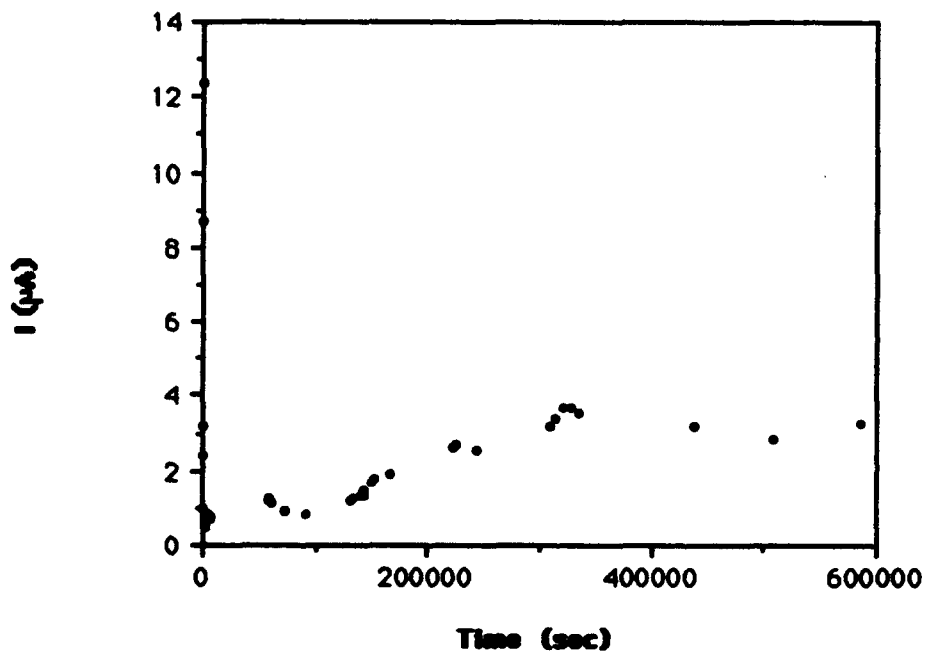
*Figure 4-47. Galvanic current diagram for AlW/P75 graphite couple.*

75
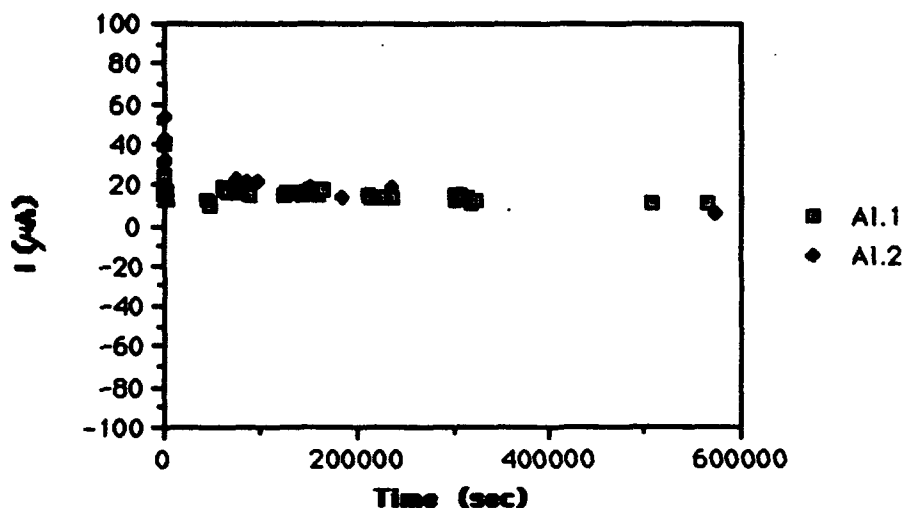
Figure 4-48. Galvanic current diagram for pure Al/P75 graphite couple.

45 minutes. After 9 hours, this current dropped to a value of 0.06 μA and remained constant (at a value of 0.04 to 0.06 μA which corresponds to current densities of 0.06 to 0.09 μA/cm^2, respectively) for the next 3 days before abruptly increasing to 6 to 8 μA for the remainder of the experiment. After completion of the experiments, the surfaces of both specimens were found to be shinny with no evidence of pitting. SEM analysis of the first specimen confirmed that the coating was indeed still present and in good condition after testing. It is believed that a small flaw (possibly produced by sputtering over dust particles on the Si substrate) or scratch, which initially did not extend to the substrate, may have lead to the increase in current on the second specimen after 3 days. Comparison of the current densities measured after after several days of coupling, i.e. 0.16 μA/cm^2, with the value of 0.28 μA/cm^2 derived from the galvanic diagram (for a c:a ratio of 0.41) shows that the diagram provides a reasonably good estimate of the actual galvanic behavior. At a constant current of 0.16 μA/cm^2, a one micron thick film could be expected to last approximately 1 year.

Figure 4-47 shows the galvanic corrosion current vs. time data for one of the two Al- 25.9%W alloy (alloy 2)/P 75 Gr couples. The cathode to anode area ratio for this couple was 0.43. In this case, an initial current of 12.4 μA was

76

noted which dropped to a value of 0.7 μA (corresponding to a current density of 2.1 μA/cm^2) after 1 hour and remained relatively constant (ranging from 0.7 to 1.2 μA) for next 35 hours before gradually increasing to a value of 3.2 μA at the end of the 7 day test. The other galvanic couple for this alloy with a cathode to anode area ratio of 0.16 exhibited an initial current of 13 μA which fell to a value of 0.81 μA (corresponding to a current density 1.0 μA/cm^2) in 48 minutes. The current further decreased to a value of 0.16 μA after 3.5 hours and slowly increased over the next 40 hours to 0.9 μA. At 95 hours, a current of 8.5 μA was observed and remained constant for the duration of the experiment. After testing, the surfaces of both specimens were reflective and no evidence of pitting was observed. Again, it is believed that small flaws or scratches may have lead to the increase in current after a few days of exposure. Comparison of the current densities measured after a few days (1μA/cm^2) with the value obtained from the galvanic diagram (0.23 μA/cm^2 for a c:a ratio of 0.43) shows good agreement with the predicted value being slightly higher than the actual measured value.

Control data for one of the two pure Al/P75 graphite couples with a cathode to anode area ratio of 0.11 are shown in figure 4-48. Initially, a relatively high current of 40 μA was observed which dropped off a value of 20μA (which correlates to a current density of 10μA/cm^2) after 1 minute and continued to slowly decrease for the duration of the experiment. At the end of the experiment, a current density of 5.5 μA/cm^2 was measured and visual observation revealed that very little Al was present on the Si substrate. At a constant current density of 5.5 μA/cm ^{2}, a 1μ thick film would last less than 1 day. The other Al/Gr couple had a cathode to anode area ratio of 0.13 and exhibited similar behavior. Additional tests, where the visual appearance of the specimen is noted with time, will be needed in order to estimate the galvanic corrosion rate of the pure Al/Gr couple. According to the galvanic diagram, the predicted current density of a pure Al/Gr couple (considering a c:a ratio of 0.11) would be 34 μA/cm^2, which provides a conservative estimate when compared to the actual current density of 5.5μA/cm^2.

Low steady state galvanic corrosion currents were also noted for the heat-treated Al alloy/Gr couples as shown in Figures 4-49 and 4-50. An initial current of 6.1μA was noted for one of the two Al-19.1%Mo heat-treated/P75 Gr couples

77

(cathode/anode area ratio of 0.14) which dropped off to a steady state value of 1.5 μA after 5.8 days as shown in Figure 4-49. The second couple (cathode to anode area ratio of 0.18) also showed an initial current of 6.1 μA which fell off to a value of 2.4 mA after 45 minutes and then decreased to 0.16 μA after 50 hours. Following this, the current for second couple increased to 9μA and occasionally oscillated between anodic and cathodic behavior. At the end of the test, it was noted that the second specimen contained a small blistered region near the top of the specimen. The remaining 70 % of this specimen was intact and in good condition with no pits. After testing, the first specimen was found to be fully intact, optically reflective, and free of pits. The data for one of the two heat-treated Al-25.9%W/P75Gr couples (cathode to anode area ratio of 0.434) , Figure 4-50, revealed an initial current of 16 μA which fell to a steady state value of 0.05 μA (corresponding to a current density of 0.1 μA/cm^2) after 19 hours and remained constant at this value for the duration of the test. The second heat-treated Al-25.9%W/P75 Gr couple exhibited an initial potential of 1 μA and a steady state value of 0.3 μA (corresponding to a current density of 0.33 μA/cm^2). After testing, the surfaces of both of the specimens were reflective and no evidence of pitting was observed.

While the nature of the specimens appears to make determination of an exact steady state galvanic current difficult in some cases--the important issue of whether or not performance of a composite could be improved through nonequilibrium alloying is easily answered by the visual appearance of the specimens after testing. Figure 4-51 compares the appearance of the surfaces of pure Al, the Al-19.1%Mo alloy, the Al-25.9%W alloy, and the heat treated Al-25.9%W alloy after galvanic coupling to graphite for 1 week. The alloy surfaces were optically reflective after testing (and appear black in the photograph), while only a small amount of the pure Al film (light areas in the photograph) remained after 7 days.
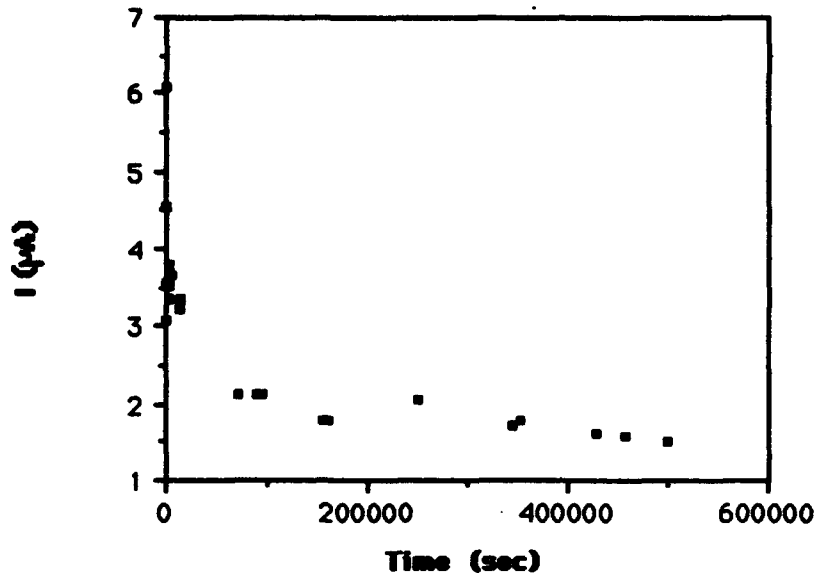
Figure 4-49. *Galvanic current diagram for heat-treated AlMo/P75 graphite couple.*
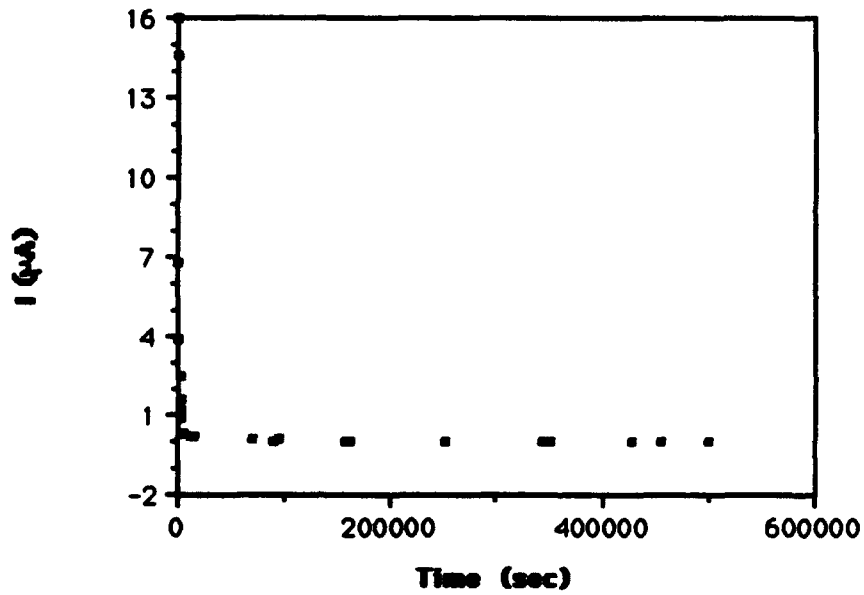

Figure 4-50. *Galvanic current diagram for heat-treated AlW/P75 graphite couple.*
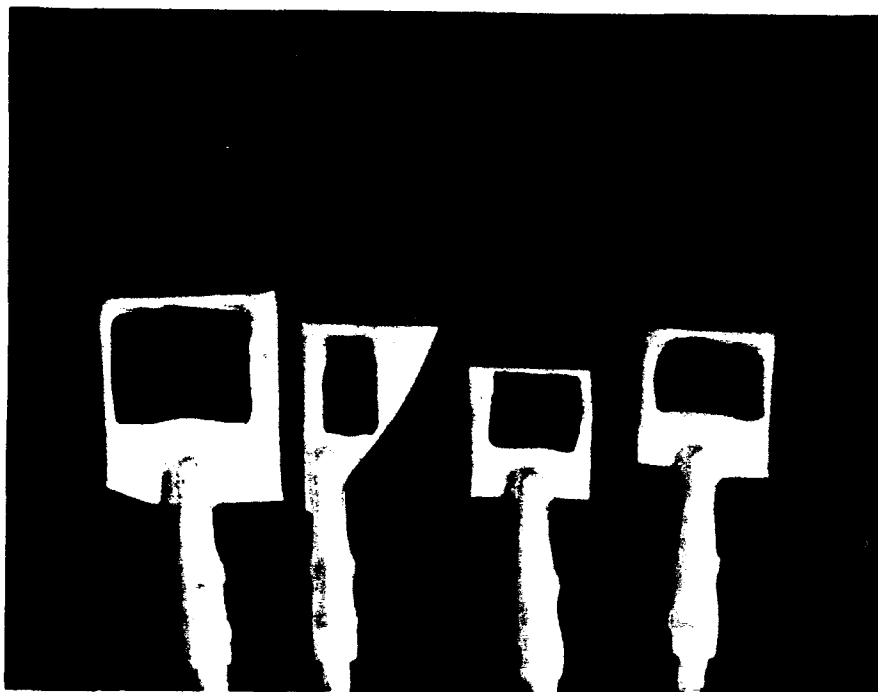
Figure 4-51. Comparison of surface appearance of pure Al, AlMo, AlW, and heat-treated AlW.

Galvanic current measurements were also obtained on pure Mg/P75 Gr and Mg-2.6Cr/P75 Gr couples in artificial seawater. These results are presented in Figures 4-52 and 4-53. Since the Mg and Mg alloys are much more active than the Al alloys, rapid corrosion resulted in exposure of the underlying Si substrate in a matter of hours; therefore, only the galvanic current data for this time period is shown. The rapid corrosion of the Mg and the uncertainty in the exact time to exposure of the underlying Si make interpretation of the Mg galvanic current data difficult. Figure 4-52 shows the galvanic current vs. time data obtained for one of the two pure Mg/P75 Gr couples with a cathode to anode area ratio of 0.16. An initial current of 786 μA was noted which fell to a value of approximately 478 μA after 4 minutes. At 30 minutes, a current of 538 μA was observed which increased to 575 μA (720 μA/cm^2) at 1 hour

and then decreased for the duration of the experiment. No Mg was found on the surface of the Si at the end of the experiment. The second couple (c:a=0.12) exhibited similar behavior and had a final current density of 425 μA/cm^2. It is estimated that the galvanic corrosion current density for the Mg is approximately

570 μA/cm^2. Considering a constant current density of 570 μA/cm^2, the film would be corroding at a rate of 1.5 μm/hr and would be lost within the first few hours of coupling. Figure 4-53 shows the galvanic current vs. time data for one of the two Mg-2.6Cr alloy couples with a cathode to anode area ratio of 0.16. For this couple, initial currents of 35 μA were noted which fell to 17.3 μA after 45 hours and then rapidly decreased. The second couple exhibited an initial current of 1608 μA which rapidly fell to 211 μA after two minutes and finally dropped to a steady state value of approximately 10 μA (6.3 μA/cm^2). Again, no material remained on the surface of the Si at the end of the experiment. An average galvanic corrosion current density of 6 to 17 μA/cm^2 was estimated for this alloy, which is much lower than the current density for the pure Mg (570 μA/cm^2) and is the result of the dramatic shift in E$_{corr}$ for the nonequilibrium alloy. The measured galvanic current density for the Mg alloy (6-17 μA/cm^2) compares favorably with the value estimated using the galvanic diagram (15.2 μA/cm^2).
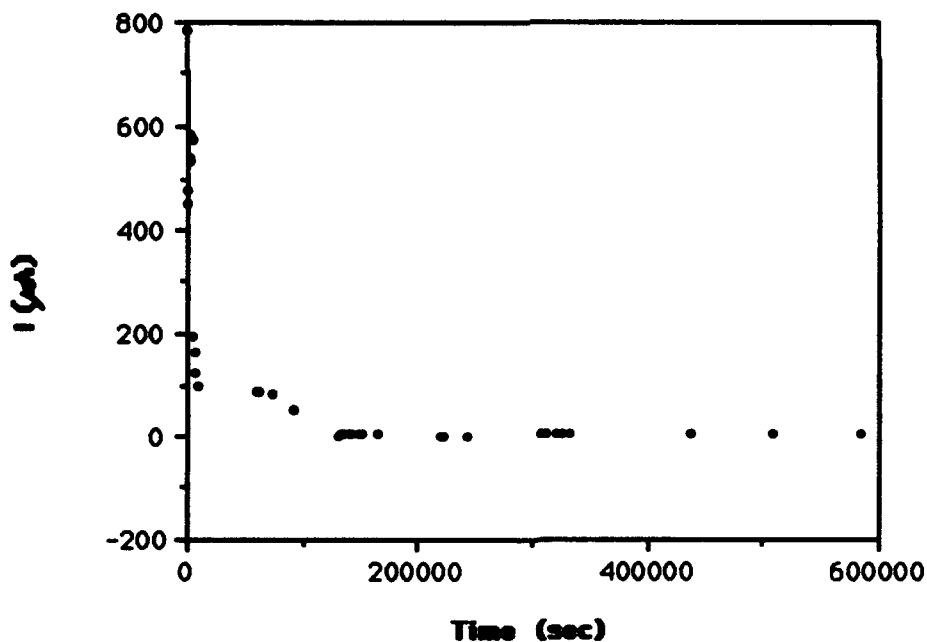
Figure 4-52. Galvanic current diagram for Pure Mg/P75 graphite couple.
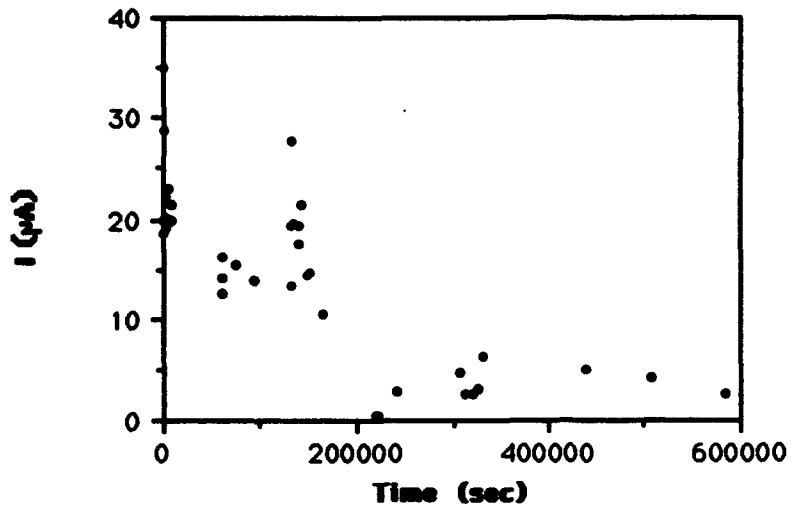
**Figure 4-53. Galvanic current diagram for MgCr (alloy 7)/P75 graphite couple.**

5.0 DISCUSSION

Alloying Mg or Al with Cr, Mo, Ta, or W to form binary alloys had a significant impact on their corrosion behavior. In general, all of the transition metals studied increased the corrosion potential of Mg to more noble potentials. Figure 5-1 shows the dependence of E_{corr} on the amount of each solute in the alloy. For Cr, Mo, and W, E_{corr} increases at approximately the same rate as a function of solute concentration (below 2 at.%). As the solute concentration increases, E_{corr} levels off for the alloy containing Cr, whereas E_{corr} continues to increase for the W-containing alloy. This behavior suggests that these two elements may play different roles in affecting the corrosion behavior the Mg. For example, if E_{corr} is controlled by the effect that the solute has on the hydrogen exchange current density, this result indicates that Cr would be less effective at controlling the hydrogen reaction. This result would be expected, because Mg and Cr have similar hydrogen exchange current densities, whereas the other three elements have exchange current densities almost three orders of magnitude greater than Mg and Cr, and should be more effective at increasing E_{corr} with higher solute concentrations. Additional work will need to be performed to elucidate the mechanism controlling the observed shift in E_{corr}, particularly in light of the rapid dissolution of these alloys and its effect on obtaining steady-state conditions. However, the behavior of Mg may be similar to that observed for the Al alloys, where E_{corr} can be impacted by alloying.

The behavior of E_{corr} in the Mg-Ta system would seem to not support our theory. Tantalum has an exchange current density similar to W, yet E_{corr} initially becomes more active as the Mg is alloyed with Ta. This result is probably related to the large Ta particles that were deposited onto these films during their growth. It is not clear why Ta particles were ejected from the target onto the film during sputtering, but these large particles would surely impact the film's corrosion behavior. Therefore, the Mg-Ta results must be viewed in the light of how these Ta particles could alter the polarization response of the film.

Unfortunately for the Mg system, the change in E_{corr} does not appear to dramatically improve the galvanic compatibility of these alloys with graphite. Exposure of Mg-7.6 at. % Mo and Mg-11.4 at. % W on graphite substrates resulted in their rapid dissolution, indicating that the solutes had not stabilized
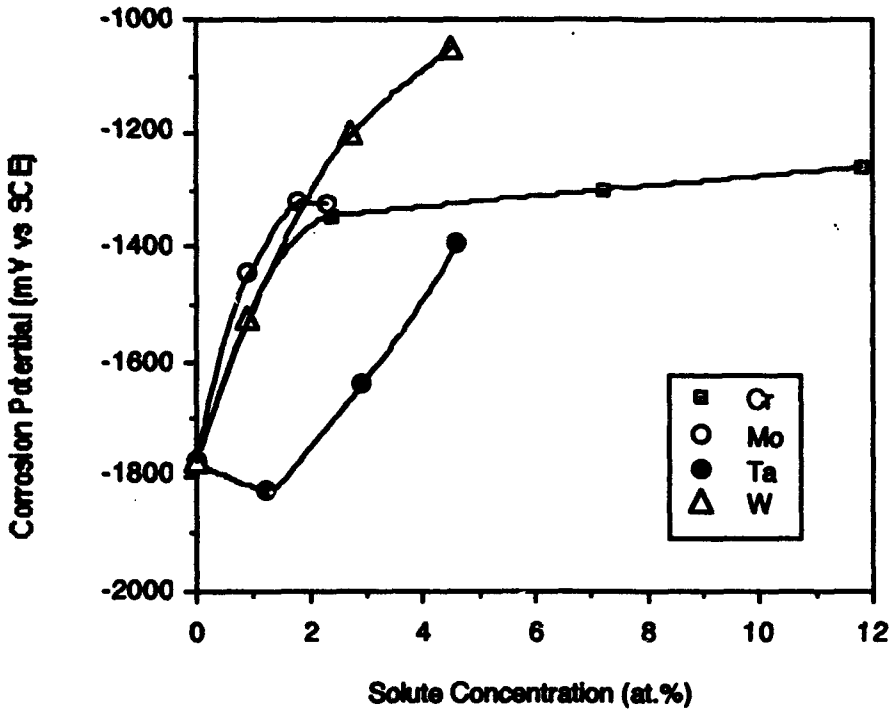
Figure 5-1. *Response of the corrosion potential (E_{corr}) for the Mg alloys containing either Cr, Mo, Ta, or W. E_{corr} for each Mg alloy responses similarly as a function of concentration -- with the exception of Ta -- at low concentrations. Above 2 at. %, E_{corr} for W continues to increase significantly above -1400 mV(SCE).*

the films sufficiently to protect them from attack. Heat treatment results also showed that the Mg-11.4 at. % W alloy formed precipitates during aging. The relatively high galvanic corrosion rates for the Mg alloys coupled with the poor thermal stability of Mg-W precludes further evaluation of these Mg-based alloys as potential composite matrix materials.

Sputtered Al alloys show good potential for use as matrix materials in graphite-reinforced composite systems. The major limitation of these alloys will be the significant increase in density (compared to pure Al) required to protect the alloys against galvanic attack with graphite. The density of these alloys can be determined from equation 2:

$$\rho_T = \frac{w_1 - w_2}{V_T} \qquad (2)$$

Where ρ_T is the alloy density, w_1 and w_2 are the weight of each element in the alloy and V_T is the total volume. This equation can not be solved directly, but assuming that the solute substitutes with Al or Mg atoms in the lattice without introducing a significant volume change, the alloy density can be rewritten as:

$$\rho_T = \rho_1 \chi \left(\frac{n_2}{n_1}\right) \left(\frac{a_1{}^3}{a_2{}^3}\right) + \rho_2 (1-\chi) \qquad (3)$$

where ρ is the density, χ is the at.% of the solute in the alloy, n is the number of atoms in the unit cell for the pure element, a it its lattice constant, and 1 and 2 denote the solute and base metal (Mg or Al), respectively, in the alloy. The assumption for a small volume change should only lead to a small error due to the close relative atomic size of the transition metals with Al. The error will be much more significant for the Mg alloys. Solving for density is now relatively simple. For example, in the case of an alloy containing 20 at.% W, the density of the alloy would be approximately 5.8 g/cm^3. Molybdenum, with a density of only 10.28 g/cm^3, would produce an Al-20 at.% Mo alloy with a density of 4.1 g/cm^3, and at 10 at.% Mo the density would be 3.5 g/cm^3. From a weight standpoint, the Al-Mo alloys would have a significant advantage. However, only the high solute concentration Al-Mo and Al-W alloys maintained a single phase structure following heat treatment for 1 hour at 400 C.

Several alloys are presently under investigation that combine the attractive corrosion properties of Al with the low density of Mg in an attempt to load the alloys with high density transition metals without paying a significant weight penalty. Early results on the Mg-Al-W alloys have not been promising, with the alloy pitting at potentials below -600 mV. This result may be dependent on the odd two-phase structure that developed during deposition in this alloy. However, the Al-Mg-W alloy (alloy #4) exhibits corrosion resistance equivalent

to that of the Al-19.1 at.% Mo and the Al-25.9 at.% W alloys. Further tests are being conducted on the Al-Mg-W alloy and also on Al-Mg-Mo alloys.

XRD results suggest that the films are more stable with higher concentrations of solute in the alloy. This result is surprising and not intuitively obvious, because it would be logical to conclude that the alloys having a higher concentration of solute would increase precipitation, particularly above 0.5 T/T_m, where bulk (volume) diffusion processes begin to become significant. Heat treating at 400°C ($\sim$ 0.7 T/T_m) would be expected to precipitate the supersaturated solute, and this is found to be true below approximately 10 at.% solute. Above this solute concentration, many of the Mg and Al alloys, with the exception of the Al-Cr and the Mg-Ta alloys, remain stable. Additional studies into the mechanism behind this behavior are presently in progress and will be reported in the next annual report.

Eventually, several selected alloys will be deposited onto Gr fibers and consolidated into a composite. Although corrosion performance is the key performance criteria to meet in the selection of an alloy for further study, other factors will be critical in the successful fabrication of the composite. We have already discussed the role of density on composite performance; other variables will be CTE compatibility and mechanical stability. Large differences in CTE between the fiber and the matrix will result in introducing large residual stresses during cooling. Clearly the effect of residual stress is undesirable, both from successfully consolidating the composite as well as long term component performance. Large residual stresses exceeding the fracture strength of the alloy can result in cracking of the composite. High residual stresses can also promote stress corrosion cracking in aggressive environments and reduce the fatigue life of the metal. Fortunately, adding the transition metals reduces the alloys CTE from the high values of Mg or Al, thereby reducing microstrain. The limitation to this approach is that too much transition metal can lead to an alloy with an amorphous structure, which would have a difficult time relieving stresses by yielding. Therefore, final alloy selection must not only be based on the corrosion behavior of the alloy, but also on the processability and fabricability of the alloy. For this reason, we would suggest selecting an Al alloy with the minimum solute concentration (either W or, preferably, Mo) needed to allow high temperature processing and still provide a crystal structure were slip

(yielding) is possible. A better choice, from a weight standpoint, would be an ternary Al alloy containing both Mg and a solute (W or Mo).

6.0   CONCLUSIONS

This year's results have clearly shown that Mg based alloys containing either Mo, Cr, W, or Ta, will not be suitable for use in a graphite-reinforced composite. Although heat treatment conditions have been identified that can be used to consolidate the alloys without degrading the alloy microstructure, the limited improvement in the corrosion performance of the Mg alloys was insufficient to protect them from galvanic attack when coupled to graphite.

Several Al based alloys have been identified that are galvanically compatible with graphite and could be used in a composite. Al-Mo and Al-W alloys containing more than 10 at. % solute have been heat treated at nominal consolidation temperatures and retain their corrosion resistance. XRD results show no evidence of alloy degradation after heat treating and the alloys remain as single phase films. Below 10 at. % solute, the films can not be heat treated without the solute reacting to form Al intermetallic phases, which degrade corrosion performance.

The performance of the AlMgW alloy is also very promising and the next phase of the program will focus on AlMgW and AlMgMo ternaries in addition to Al-Mo and Al-W as potential matrix materials for Gr reinforced composites. Matrix metal corrosion performance will be emphasized in further alloy down selection; however, other key material properties, such as density and strength, will also be taken into consideration.

7.0 REFERENCES

1. W.H. Pfeifer, "Hybrid and Select Metal Matrix Composites: A State of the Art Review,: W.J. Renton, ed., American Institute of Aeronautics and Astronautics, pp. 231-252, (1977).

2. M.G. Vassilaros, D.A. Davis, G.L. Steckel, and J.P. Gudas, "Marine Corrosion and Fatigue of Graphite Aluminum Composites," Proceeding of the 1980 Tri-Service Corrosion Conference, Vol. 2, U.S. Government Publication (1980).

3. M.M. Aylor, and R.M. Kain, "Assessing the Corrosion Resistance of Metal Matrix Composite Materials in Marine Environments," ASTM STP 864 - Recent Advances in Composites in the US and Japan, Vinson and Taya, ed., American Society of Testing and Materials, Philadelphia, (1985).

4. P.P. Trzaskoma, "Corrosion Behavior of Graphite Fiber/Magnesium Metal Matrix Composite in Aqueous Chloride Solution," Corrosion, Vol. 42,. p. 609, (1986).

5. E. Chin and J. Nunes, "Alloying Effects in Graphite/Magnesium Composites," Advances in Magnesium Alloys and Composites, H. Paris and W. Hunt, Ed., The Minerals, Metals, and Materials Society, (1988).

6. D.M. Aylor, R.J. Ferrara, and R.M. Kain, "Marine Corrosion and Protection For Graphite/Aluminum Metal Matrix Composites," Materials Performance, Vol. 23, p. 32, (1984).

7. D.M. Aylor and P.J. Moran, "Effect of Reinforcement on the Pitting Behavior of Aluminum-Base Metal Matrix Composites," J. Electrochem. Soc. Vol. 132, p. 1277, (1985).

8. D.L. Dull, W.C. Harrigan, Jr., and M.F. Amateau, "Final Report - The Effect of Matrix and Fiber Composition on the Mechanical Strength and Corrosion Behavior of Graphite-Aluminum Composites," Aerospace Report ATR-76 (7564)-1, El Segundo, CA, (1977).

9. E.G. Kendall and D.L. Dull, "Salt Water Corrosion Behavior of Aluminum-Graphite Composites," National Technical Information Service, U.S. Department of Commerce, AD-777, p. 160, (1974).

10. L.H. Hihara, "Corrosion of Aluminum-Matrix Composites, "Ph.D. Dissertation, Massachusetts Institute of Technology, (1985).

11. C.R. Crowe, "Localized Corrosion Currents from graphite Aluminum and Welded SiC/Al metal Matrix Composites," NRL Memorandum report 5415, Naval Research Laboratory, February, 1985.

12. W.C. Moshier, G.D. Davis, J.S. Ahearn, and H.F. Hough, "Influence of Molybdenum on the Pitting Corrosion of Aluminum Films," J. Electrochem. Soc., Vol. 133, p. 1063, (1986).

13. W.C. Moshier, G.D. Davis, J.S. Ahearn, and H.F. Hough, "Corrosion Behavior of Aluminum-Molybdenum Alloys in Chloride Solutions," J. Electrochem. Soc., Vol. 134, p. 2677, (1987).

14. W.C. Moshier, G.D. Davis, and G.O. Cote, "Surface Chemistry of Sputter-Deposited Al-Mo and Al-Cr Alloys Polarized in 0.1M KCl," J. Electrochem. Soc., Vol. 136, p. 356, (1989).

15. G.D. Davis, W.C. Moshier, T.L. Fritz, and G.O. Cote, "Evolution of the Chemistry of Passive Films of Sputter-Deposited, Supersaturated Al Alloys," J. Electrochem. Soc., Vol. 137, p. 422, (1990).

16. B.A. Shaw, T.L. Fritz, G.D. Davis, and W.C. Moshier, "Influence of Tungsten on the Pitting of Aluminum Films," J. Electrochem. Soc., Vol. 137, p. 1317, (1990).

17. P.L. Hagans, "Electrochemical Study of the Passivation and Passive Film Breakdown of Mg70-Zn30 Metallic Glass," Materials Research Society Symposium Proceedings, pp. 113-120, (1987).

18. H.H. Uhlig, Corrosion and Corrosion Control, John Wiley and Sons, New York, p. 348, (1971).

19. G.L. Makar and J. Kruger, "Corrosion Studies of Rapidly Solidified Magnesium Alloys, J. Electrochem. Soc., Vol. 137, p. 414, (1990).

20 J.M. West, Electrodepostion and Corrosion Processes, Van Nostrand Reinhold, London, p. 57, (1965).

21. R.G. Wendt, "Advanced Interceptor Pointing Structures," Martin Marietta Report MCR-91-4020, (1991).

22. F. Hehmann, F. Sommer, H. Jones, and R.G.J. Eduvean, "Corrosion inhibition in magnesium-aluminum-based alloys induced by rapid solidification processing," J. Mater. Sci., Vol. 24 (1989) 2369-2379.

23. D.A. Jones, Principles and Prevention of Corrosion, Macmillan Publishing Co., New York, (1992).